In-fiber Semiconductor Filament Arrays

by

Daosheng Deng

Submitted to the Department of Materials Science and Engineering
in partial fulfillment of the requirements for the degree of

Doctor of Philosophy in Materials Science and Engineering

at the

MASSACHUSETTS INSTITUTE OF TECHNOLOGY

February 2010

Author .....
Department of Materials Science and Engineering
January 15, 2010

Certified by.....
Yoel Fink
Associate Professor of Materials Science
Thesis Supervisor

Accepted by .....
Christine Ortiz
Chair, Departmental Committee on Graduate Students.

In-fiber Semiconductor Filament Arrays

by

Daosheng Deng

Submitted to the Department of Materials Science and Engineering
on January 15, 2010, in partial fulfillment of the
requirements for the degree of
Doctor of Philosophy in Materials Science and Engineering

Abstract

One-dimensional nanostructures with high aspect-ratios and nanometer cross-sectional dimensions have been the focus of recent studies in the persistent drive to miniaturize devices. Conventional bottom-up methods such as vapor-liquid-solid growth have been widely applied for the fabrication of uniform and high quality nanowires. Two challenges toward nanoelectronics and other applications remain: on the single-nanowire level, precisely manipulating an individual nanowire for the sophisticated functionalities, and on the multiple-nanowire level, integrating nanowires into designed architecture at large scale. Thus, an alternative approach with the capacity to achieve ordered and extended nanowires is highly desirable.

In this thesis, we observe an intriguing phenomenon that a cylindrical shell upon reaching a characteristic thickness breaks up into filament arrays during optical-fiber thermal drawing. This structural evolution occurs exclusively in the cross-sectional plane, while the uniformity along the axial direction remains intact. We demonstrate crystalline semiconductor nanowires by post-drawing annealing procedure and characterize their electrical and optoelectric properties for the devices such as optical switch. This top-down thermal drawing approach provides new opportunities for nanostructure fabrication with high throughput and at low cost, and offers promising applications in renewable energy and data storage.

In order to understand the stability (or instability) of thin shells and filaments, we explore a physical mechanism during the complicated thermal drawing. A perspective of capillary instability from fluid mechanics is focused. Axial stability of continuous filaments is consistent with capillary instability. Axial stability of a thicker cylindrical shell arises from large radius and high viscosity. These results provide theoretical guidance in the understanding of attainable feature sizes and in materials selection to expand the potential functionalities of devices in microstructured fibers.

Thesis Supervisor: Yoel Fink
Title: Associate Professor of Materials Science

Acknowledgments

I would like to take this specifical opportunity of thesis writing to express my sincere gratitude to many people who helped me and supported me academically and personally during my PhD study at MIT.

I would like to thank my academic mentors during PhD study. First, I am grateful for my thesis advisor, Prof. Yoel Fink, who is an exceptional scientist with deep conviction and great vision. His charisma, integrity and perseverance enormously influence my intellectual growth during the past years. His patience and support, which allows me to explore scientific adventure in broad areas, is indispensable to all results in this thesis. More importantly, his persistent encouragement helps me to grow and mature scientifically. Secondly, I would also like to thank my thesis committee members, Prof. Steven Johnson and Prof. Francesco Stellacci, for their constant support and guidance during my research. I am indebted to Prof. Howard Stone, who has recently moved from Harvard University to Princeton University. His genuine interest and scientific support of my thesis project greatly inspired me to move forward.

I would like to thank the experimental and theoretical team members during my past research. I would like to thank experimental team members including Dr. A. Abouraddy for guiding me through the project with many constructive feedbacks and Dr. N. Orf for teaching and helping me to draw fibers. I would like to thank theoretical team members including Dr. J. C. Nave for contributing numerical simulations and Prof. Steven Johnson for investing his time and effort to train me how to do research. In addition, I am thankful for Dr. S. Danto to teach me crystallization.

I would like to thank all the other members in Prof. Fink's group who provide friendly environments: Dr. Wang Z, Dr. Sorin F, Dr. S. Ofer, Dr. S. Egusa, S. Stolyarov, D. Shemuly, N Chocat, Z. Ruff. I would like to extend my thanks outside the group. Dr. S. Kooi helped me with SEM micrographs, P. Boisvert and Dr. Y.

Zhang helped me with TEM micrographs.

I would also like to acknowledge the support of Gilbert Y Chin Fellowship when arriving to MIT, and other funding agencies for the projects including DARPA, ARO, the ONR and the AFOSR, as well as the NSF/MRSEC program through the CMSE shared facilities.

I would like to express my gratitude to family members. While I was away from homeland China, my parents and old brother, support greatly me behind, although they wished I could have stayed in China. I am particualr grateful to many friends in Boston, who help, support and encourage me greatly during my PhD study.

He hath made every thing beautiful in his time. (Ecclesiastes 3:11)

Contents

List of Figures

Chapter 1

Introduction

Interests in efficient processing of semiconductor nanowires (nanofilaments) are motivated by their unique physical properties and the potential for wide applications in electric devices, life science, and renewable energy. Silicon-wafer-platform based approaches, such as vapor-liquid-solid growth and lithography, have successfully fabricated high-quality nanostructures. Nevertheless, filaments produced by these conventional techniques are inherently limited to micrometer-length scales, are fraught with mechanical fragility, and lack global orientation. Consequently the manipulation, integration, and macroscopic assembly of filaments have proven heretofore to be extremely challenging. It is intriguing to link the nanostructures with the traditional approach to optical-fiber fabrication, which is a well-developed technique for producing kilometer-long uniform optical fibers with high throughput and at low cost.

This work may be considered a marriage of two different research fields: optical fibers and nanostructures. Although optical fibers share the cylindrical form factor with filaments, they are produced at much larger dimensions and, furthermore, are usually fabricated out of insulating glasses, not semiconductors. It is therefore intriguing to investigate whether some variant of fiber thermal drawing can be developed to produce semiconductor filaments with much longer lengths than previously thought possible.

The focus of this thesis, which provides a top-down thermal- drawing platform to produce in-fiber filament arrays, is motivated by the ultimate feasibility of feature size

of cylindrical shells on our multimaterial fibers. We find a novel physical phenomenon in which a cylindrical shell evolves into an ordered array of filaments during the thermal drawing. This "preform-fiber-filament" methodology offers a unique approach to produce high-aspect-ratio nanofilaments in a high-throughput and low-cost fashion. Extended nanowire bundles may be potentially useful in large-area nanowire-based applications including renewable energy (photovoltaics, thermoelectrics), nonlinear optics (exploring nonlinear optical dynamics in two-dimensional wire arrays), or bioengineering (scaffolding for organ growth).

In Chapter 2, we will further describe the general motivation for ultimate feature size in the nanoscale, and discuss recent progresses in one-dimensional nanostructures. In Chapter 3, we introduce a new family of multimaterials fibers, and the attainable uniform cylindrical shells on the micrometers scale. In Chapter 4, we study the experimental observation that a cylindrical shell undergoing a scaling process evolves into an ordered array of filaments upon reaching a limited thickness. The breakup occurs exclusively in the fiber cross- section, while uniformity is maintained in the axial direction. The tendency of breakup is related to materials viscosity. In Chapter 5, we attain the crystalline semiconductor nanofilaments with a post-drawing annealing procedure, and demonstrate the simplicity of electric connection by contacting to external circuitry through the fiber end facets. These results hold promise for the large-area electronics. In Chapter 6, we proceed to explore the mechanism of thin-film filamentation. The classic capillary instability is focused. The continuity of filaments is explained since capillary instability has insufficient time to develop due to the fast drawing time. In Chapter 7, to further extend the capillary instability in the geometry of cylindrical shells, direct numerical simulation is performed via a finite element method for the Navier-Stokes equations. A radial stability map is established to survey the feasible feature size, providing guidance to identify the suitable viscous materials selections. Last Chapter 8 briefly addresses the future ongoing work.

Chapter 2

Background of nanostructures

2.1 Introduction

The idea of nanoscience and nanotechnology was originally conceived in December, 1959, when physicist Richard Feynman presented his lecture, *There's Plenty of Room at the Bottom*, at an American Physical Society meeting at Caltech [1]. Feynman articulated his vision as follows: "The principles of physics, as far as I can see, do not speak against the possibility of maneuvering things atom by atom. It is not an attempt to violate any laws; it is something, in principle, that can be done; but in practice, it has not been done because we are too big."

Recently, nanotechnology has provided many opportunities in diverse areas [2]-[9]. First, in fundamental research, new interesting phenomena arise from nanoscale confinement such as size-dependent optical excitation, quantized electrical conductance. Second, in microelectronics, the reduced feature size of each single component in the integrated circuits enables greater performance, faster operation, and less power consumption. Third, in information storage, an individual magnetic and optical component at nanometer scale is essential for high-density information storage. Fourth, in biotechnology and life science, the miniaturized devices can be powerful for real-time and cost-effective diagnostics and medicines.

Specifically, we focus on one-dimensional nanowires, which typically have transversal dimension between 1 to 100 nm. Many techniques have been developed in the

synthesis and formation of nanowires. These strategies can be classified into two categories. One is bottom-up approaches, including spontaneous growth (such as vapor-liquid-solid growth)and template-based synthesis. Spontaneous growth produces single crystal nanowires along a preferential crystal growth direction depending on the crystal structures and surface properties. Template-based synthesis mostly generates polycrystalline or even amorphous products. The other is top-down techniques, including electrospinning and lithography. Electrospinning fabricates extended polymer nanowires by applying electric force to eject an electrically charged jet. Lithography, such as electron beam lithography, defines the nanoscale patterns which are transferred to form nanowires. Nanowires fabricated by vapor-liquid-solid method are discussed with more extensive details in this chapter.

2.2 Approach of vapor-liquid-solid growth

Vapor-liquid-solid (VLS) approach to grow nanowires (NWs),was first found by Wagner and Ellis in 1960s [10]. One key feature of this synthesis is anisotropic growth along a specific direction, as shown in figure 2-1. Typically, metal nanoparticles (Au) are used as catalyst to guide the axial growth. Generally, a growth species is evaporated and dissolves into a liquid droplet (figure 2-1a) . A favorable site for deposition is at the surface of liquid droplets due to its larger accommodation coefficient. Subsequently, the saturated growth species in the liquid droplet diffuse to and precipitate at the interface between substrate and liquid (figure 2-1b). The precipitation results in nucleation and crystal growth. In this fashion, the continued precipitation will separate substrate and liquid droplets, and thus nanowire is formed (figure 2-1c).

The basic process of VLS method is sketched in figure 2-2. First, a thin film of metal catalyst (such as gold, Au) are thermally evaporated on a substrate (such as Si). Second, the film is heated at elevated temperature, and melted into many droplets which act as catalyst to guide the anisotropic growth. Third, incoming gases are introduced to cause the saturation of the molten metal droplet, which subsequently leading to continuous precipitation of single-crystal nanowires.

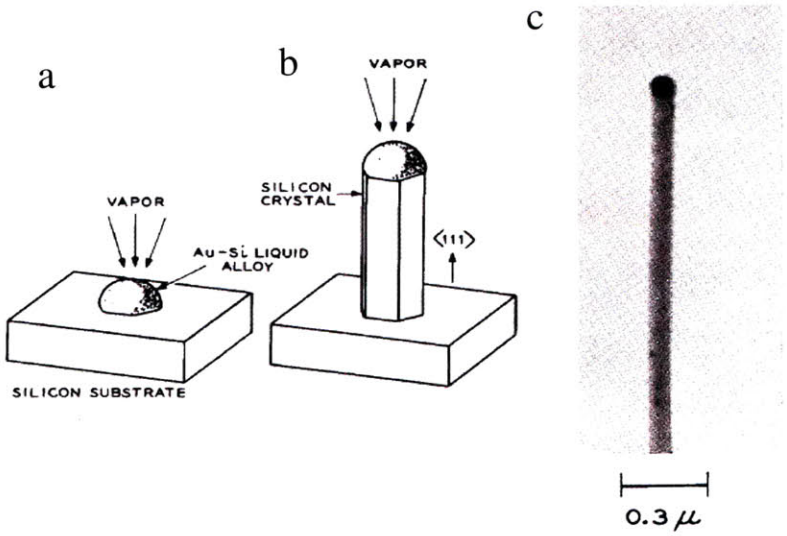

Figure 2-1: Schematic illustration and micrograph of VLS growth. **a,** initial condition with liquid droplet on substrate; **b,** growing crystal with liquid droplet at the tip; **c,** Transmission electron micrograph showing solidified gold-silicon alloy at tip. Adapted from [10].

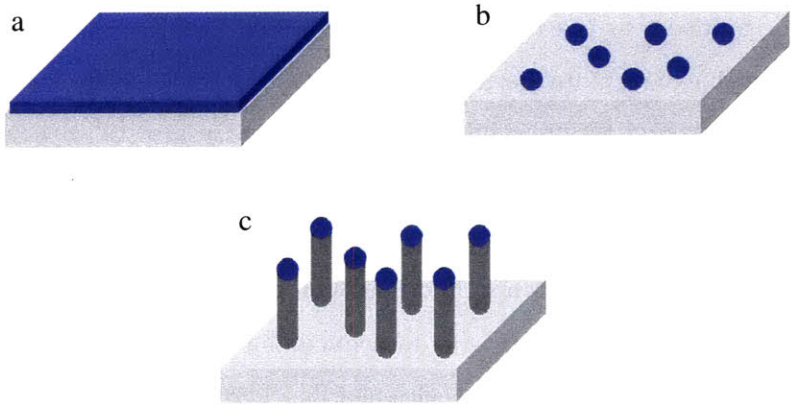

Figure 2-2: Schematic of nanowire fabrication by vapor-liquid-solid process. **a,** Thin metal film evaporated on the substrate; **b,** Metallic droplet catalyst formed by heating at elevated temperature; and **c,** Anisotropic growth of nanowires.

This method has been successfully developed to fabricate high-quality and single-crystal nanowires [11]. SEM image figure 2-3a, shows the vertical-epitaxial-growth of ZnO nnaowires; high-resolution TEM image of figure 2-3b, reveals single-crystalline attribution. These well-orientated nanowires with two naturally faceted end faces may be viewed as a resonance cavity. Under optical excitation, surface-emitting lasing action, at UV regime corresponding to a wide bandgap of ZnO, was observed.

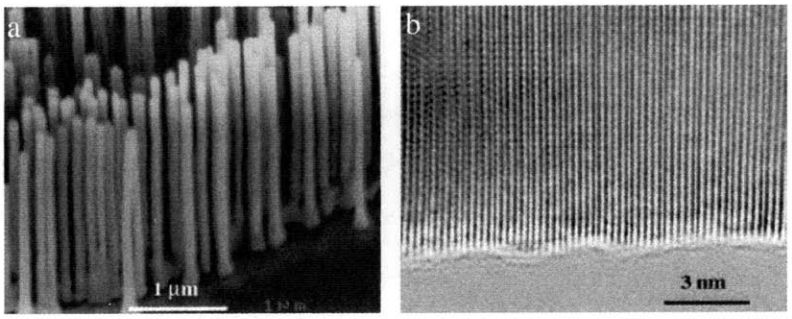

Figure 2-3: Nanowire configuration. **a,** SEM images of ZnO nanowire arrays. **b,** high-resolution TEM image of an individual ZnO nanowire. Adapted from [11].

Cross-sectional feature size of of nanowires is determined by liquid catalyst droplets associated with thickness of thin film of catalyst (such as Au). For example, 10 nm Au film under heating spontaneously breaks into droplets with feature size around 150 nm, resulting in the nanowires with cross-sectional dimension around 150 nm. If Au film thickness is further reduced such as 5 nm, the corresponding droplets has featuer size around 80 nm, which leads to nanowire growth with cross-section size further down to 80 nm. But further reduction of film thickness can not produce smaller droplets. Instead of heating a thin film, catalyst colloids are directly dispersed on the substrate surface, and nanowire with 10 nm feature size was fabricated by this method [12]. Further, to grow semiconductor nanowires at defined locations, the seeds have to be selectively positioned [5]. The most common process to pattern the seeds or droplets is electron-beam lithography, which involves resist exposure and development, evaporation of Au layer, and lift-off.

The axial length of nanowires is in the range of nanometers to micrometers, which can be controlled by synthesis condition such as growth rate and growth time. The

growth rate of nanowire by VLS method is very slow, typically at the order of $1 \sim 2\,\mu$m/min, resulting in a great challenge to fabricate extreme long nanowires. Millimeter length of NWs have been produced by high-temperature evaporation of silicon powder [13] or by accelerating the rate-limiting step in the process [14]. For example, the gas-phase reactant silane SiH_4 is replaced with disilane Si_2H_6 which has a lower activation energy of $Si - Si$ and higher catalytic decomposition. The resulting millimeter-long high-quality silicon nanowires provides the possibility to link the integrated nanometer structure through entire length for the multiple cooperated functionalities and performances.

2.3 Observation of VLS growth

Real-time observation of VLS growth is demonstrated by transmission electron microscope (TEM) [15]. VLS growth consists of alloying process, nucleation, and axial growth, as shown in figure 2-4a. Binary phase diagram of $Au - Ge$ is presented in figure 2-4b to show the phase evolution in the growth of NWs.

Three main steps are involved during the growth: formation of alloy, nucleation of alloy, and the axial growth. The first step is the alloy formation as observed in figure 2-5(a-c). Ge and Au gradually form an alloy of liquid droplets, as the amount of Ge vapor condensation and dissolution increases. This alloying process (solid Au and Au/Ge in a single-liquid phase) is depicted by an isothermal line at 800 °Cin the $Au - Ge$ phase diagram of figure 2-4b. The second step is the nucleation of alloy, as seen in figure 2-5 (d,e). Once the composition of the alloy crosses the boundary of the liquid alloy region and the alloy/Ge solid coexistence region, nanowire nucleation starts in a supersaturated alloy liquid. Occasionally, two liquid/solid interfaces are also observed, when two Ge nanocrystals precipitate from a single alloy droplet [figure 2-5(h,i)]. The last step is the axial growth [figure 2-5(d-f)]. Once Ge nanocrystal nucleates at the liquid/solid interface, further condensation/ dissolution of Ge vapor into the system will increase the available amount of Ge crystal that precipitates from the alloy. The incoming Ge species solidify at the solid/liquid interface, pushing the

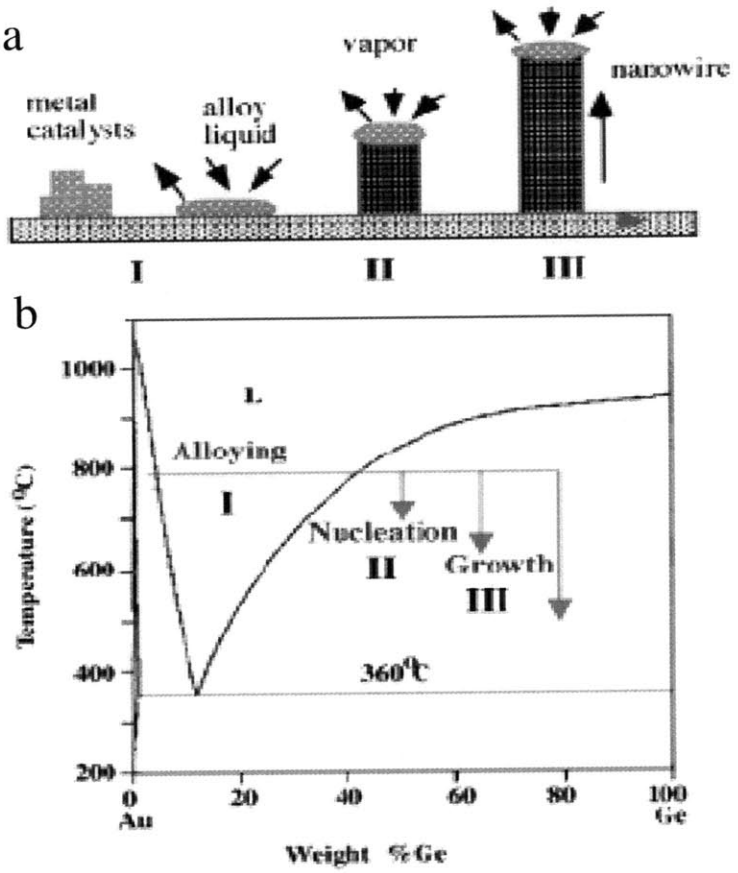

Figure 2-4: **a,** Schematic illustration of vapor-liquid-solid nanowire growth mechanism including three stages (i) alloying, (ii) nucleation, and (iii) axial growth. **b,** Au – Ge binary phase diagram to show the phase evolution dependent on composition during the nanowire growth process. Adapted from [15].

interface forward to form a nanowire (figure 2-5f). After the growth is complete, the alloy droplets solidify on nanowire tips upon cooling.

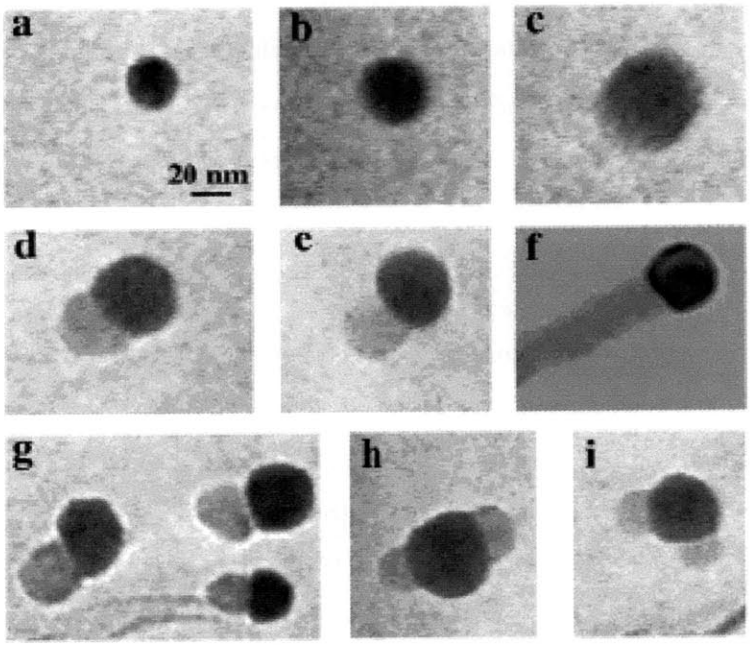

Figure 2-5: *In-situ* TEM observation of Ge nanowire growth. **a,** Au nanoclusters in solid state at 500 °C; **b,** alloying initiates at 800 °C. At this stage Au exists in mostly solid state; **c,** liquid Au/Ge alloy; **d,** the nucleation of Ge nanocrystal on the alloy surface; **e,** Ge nanocrystal elongates with further Ge condensation and eventually a wire forms; **f, g,** Two other examples of Ge nanowire nucleation; **h,i,** TEM images show two nucleation events on a single alloy droplet. Adapted from [15].

2.4 Mechanism of anisotropic growth

Generally speaking, anisotropic growth is responsible for the formation of 1D structure. To minimize Gibbs free energy, growth takes place along a preferable direction in the super-saturation state. The preferable direction is determined by direction-dependent growth rate (*e.g.* growth rate in (110) direction is faster than that of (111) direction in silicon) and imperfections in the specific crystal direction (such as screw dislocations, and impurities on facets).

In the case of VLS approach, favorable adsorption of growth species is at the

droplet surface. A rough surface of liquid alloy is composed of ledge, kink, and ledge-kink sites. Consequently, the impinging growth species can be efficiently trapped. Almost all the impinging growth species are accommodated on the growing surface. Thus growth proceeds at the liquid-solid interface.

More quantitatively, the equilibrium vapor pressure (P) of a curved surface is dependent on the surface energy and curvature,

$$In(\frac{P}{P_0}) = \frac{2\gamma\Omega}{kTr}, \tag{2.1}$$

where P is the vapor pressure of a curved surface, P_0 is the vapor pressure of a flat surface, γ is the surface energy, Ω is the atomic volume, r is the surface radius, T is the temperature, and k is the Boltzmann constant. For a cylinder-shaped nanowire, convex-side-surface with a small radius ($r < 100\,nm$) has a significantly higher vapor pressure (P) than flat-surface ($P > P_0$). If the supersaturated pressure (P_s) of growth species is below the pressure of curved surface while above the pressure of flat surface (i.e., $P_0 < P_s < P$), growth at side surface is suppressed and only axial growth is developed. By this means, the anisotropic growth is expected to form.

2.5 Nanowire manipulation, assembly, and contact

Despite the successful fabrication of nanowires, how to controllably manipulate a single nanowire and effectively assemble nanowires into a designed architecture remain the great challenges for functional devices. For example, light emitting diode need to be created by a $p-n$ junction at the overlapping point, which requires the precise crossing of p-type and n -type nanowires so that electrons and holes are injected into the junction to generate light at the confined sub-wavelength scale. Nanowire made by VLS growth, however, are generally random oriented in the substrate.

To manipulate and position the nanowires [5], several means have been applied. One method is inducing the electric polarization by applying electric field [16]. Elongated nanowires are attracted to a high electric field and line up. When a voltage is

applied between two electrodes, nanowires suspended in a solution are positioned in a parallel fashion (figure 2-6a). Additionally, alignment in a crossed way is done by applying additional electric field to form a $p-n$ junction (figure2-6b). Other methods for alignments of nanowires include fluid flow, transfer printing, and optoelectronic tweezers [17].

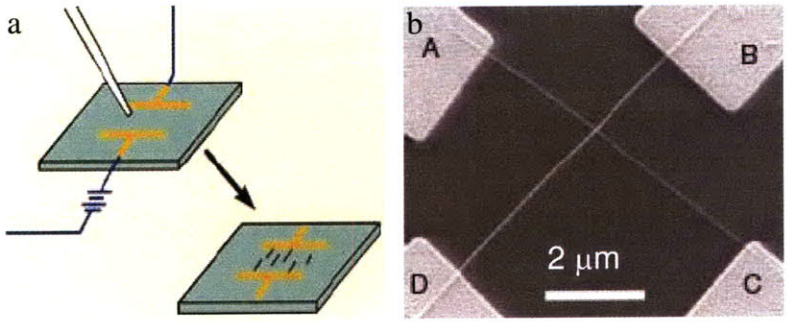

Figure 2-6: Single-nanowire manipulation. **a,** schematic view of alignment by electric field. The electrodes (orange) are biased by the applied voltage after a drop of nanowire solution is deposited on the substrate (blue). **b,** SEM image of crossed nanowires to form a $p-n$ junction. Adapted from [16].

Furthermore, large-scale hierarchical assembly and organization to scale up nanowires are indispensable for real applications such as the realization and commercialization of integrated electronic and photonic nanotechnologies. Two approaches are investigated. One is blow-film extrusion, a process for the manufacture of plastic films in large quantities by extruding a molten polymer and inflating it to obtain balloon and continuous flat film [18]. As shown in figure 2-7, the basic steps consist of (a) preparation of NW polymer suspension, (b) expansion of polymer suspension to form bubbles by nitrogen gas at a certain pressure (P), and (c) transfer of films to the substrates such as crystalline wafers, plastics, curved surfaces and open frames. This simple extrusion provides a large-scale, controlled-density nanowire films with a flexible substrate. The other is Langmuir-Blodgett technique, relying on the uniaxial compression of a NW-surfactant monolayer on an aqueous phase to produce the aligned ordered NWs [19], [20], [21]. By repeating these sequent steps, cross and more complex NW structure can be built with the controlled orientation for more integrated devices.

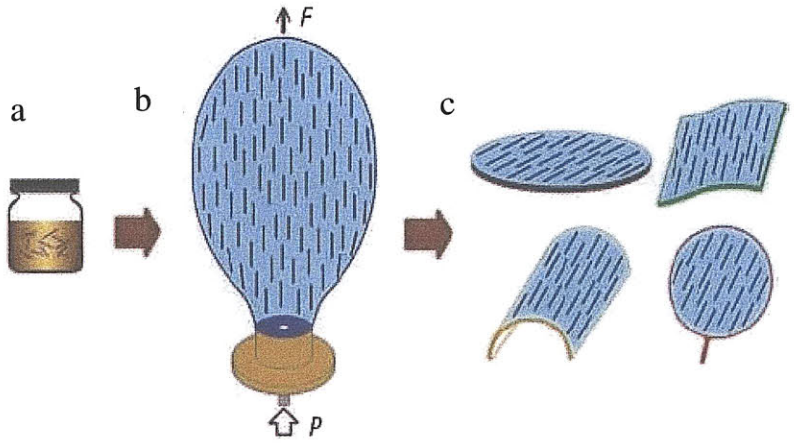

Figure 2-7: Large-area assembly of nanowires by blown bubble film process. Adapted from [18].

Moreover, to precisely contacting nanowires with the external electrical circuitry are complicated. Multiple steps are still required. (i) Grow nanowires by VLS. (ii) Remove nanowires from growth substrate by sonicating the substrate in a liquid solution, usually ethanol. (iii) Deposit nanowires onto an Si substrate by depositing a small droplet of the nanowire solution and letting it dry. (iv) Find the nanowires on the Si substrate by SEM (usually the substrate already has a grid on it for locating specific nanowires). (v) Spin Poly(methyl methacrylate) (PMMA) on the substrate and write lines from a contact pad on the grid to the nanowire. (vi) Evaporate metal and then lift-off the PMMA, so that one now can have metal contacts running from contacting pads to the nanowire and just across the nanowire.

2.6 Nanowire devices in renewable energy

Nanowire-based devices has been demonstrated for the broad applications in field effect transistors [22], light emitting diodes [16], biosensors [23], solar cells [24], and battery [25]. Particularly, nanowire provides new opportunity for solar energy, which is perhaps one of the major natural resources for clean and renewable energy. A solar cell is the associated device for solar-to-electric energy conversion by the photovoltaic effects. Two types of solar cells exist. One is the conventional silicon p-n junction

diodes. The other is excitonic solar cell, such as organic, hybrid organic-inorganic, and dye-sensitized solar cells (DSCs).

DSCs, which is based on photoexcitation of dye molecules absorbed on the surface of sintered nanoparticles, was invented by Regan and Gräzel in 1991 [26]. Light absorption and charge-carrier transport are separated in dye and semiconductor region. As shown in figure 2-8, current is generated when a photon absorbed by a dye molecule emits electrons into the conductor band of semiconductor (n-type TiO_2).

High efficiency of the DSCs is attributed two improvements. One is the high surface area of a semiconductor nanoparticle film. A cubic close packing of 15 nm sized spheres to a 10 μm thick layer is expected to increase 2,000-fold of surface area. The other is the spectral absorption range of dye, trimeric ruthenium (Ru) complex. Combination of this dye and TiO_2 covers UV and visible range.

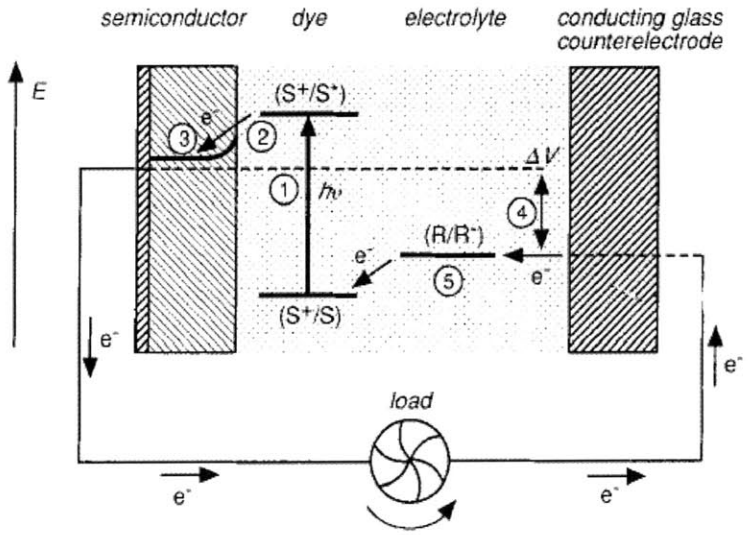

Figure 2-8: Schematic representation of the principle of DSCs to indicate the electron energy level in the different phases. The cell voltage observed under illumination corresponds to the difference, ΔV, between the quasi-Fermi level of TiO_2 under illumination and the electrochemical potential of the electrolyte. Adapted from [26]

Motivated by the fact that nanowire morphology provides direct conduction path for the electrons, a thick nanoparticle film, central to DSCs, is replaced by a dense array of oriented, crystalline nanowires (ZnO) to investigate the performance, as

shown in figure 2-9 [27], [28]. Electrons transport in oxide nanoparticle film, which is fairly well understood, proceeds by a trap-diffusion mechanism with a random walk through the film. Electron diffusion length is about $10\,\mu$m. In contrast, electron diffusion length increases in the single-crystalline nanowires. Electron transport in crystalline wires is much faster than percolation through a random polycrystalline network.

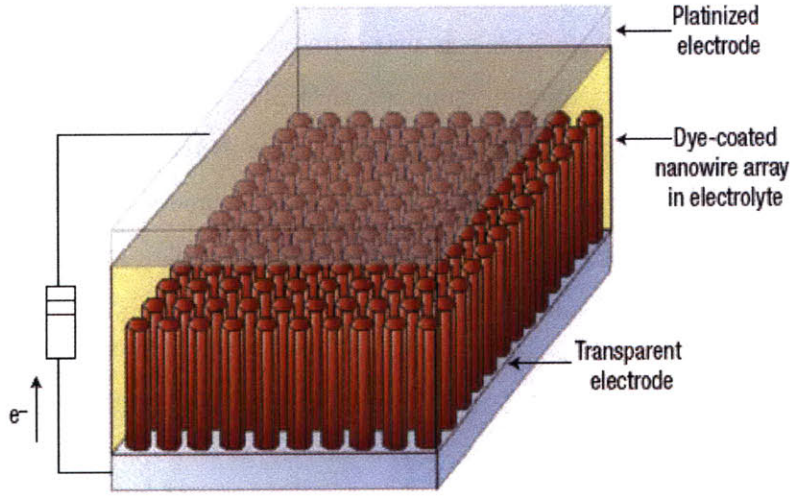

Figure 2-9: Schematic of nanowire-based solar cell. Light is incident through the bottom electrode.Adapted from [28].

The relative efficient of nanoparticle- and nanowire- based solar cells, in terms of short-circuit current (J_{sc}) and roughness factor, is presented in figure 2-10. Roughness factor is defined as the total film area per unit substrate area. TiO_2 film has a high maximum current than ZnO particles at the same roughness factor, arising from better transport through TiO_2 network. J_{sc} of ZnO nanowire almost reaches J_{sc} of efficient TiO_2 films; nanowire cells generate higher current than that of ZnO particles. Better electron transport within nanowire photoanode is expected from its higher crystallinity and the internal electric field to assist electron drift towards collecting electrode. Thus the direct electrical pathways provided by the nanowires enable the rapid collection of carriers.

More examples include solar energy generation from a new structure of the coax-

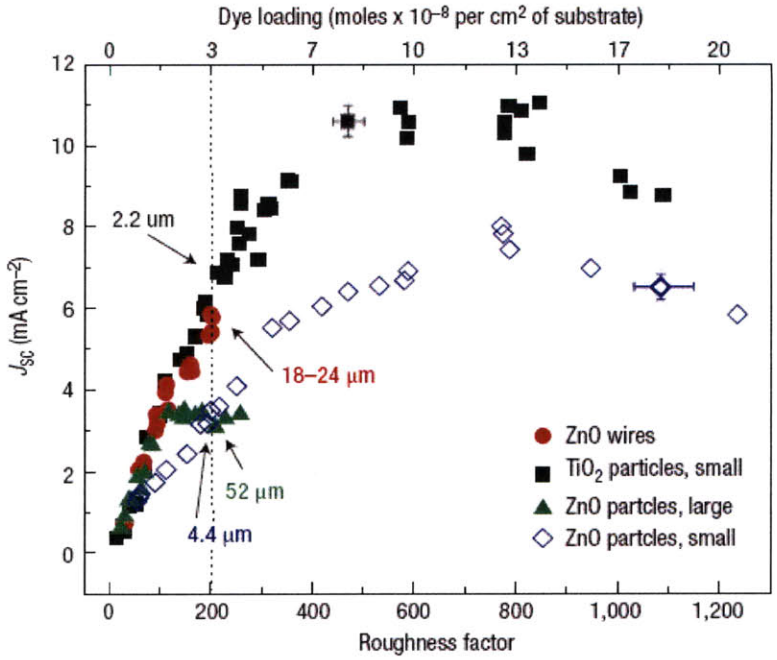

Figure 2-10: Comparative performance of nanowires and nanoparticle cells. Adapted from [28].

ial nanowires [24] and lithium battery with silicon nanowire anode [25]. Structure of coaxial silicon nanowires are characterized with a p-type silicon core capped with intrinsic and n-type silicon shells. Electrons and holes are swept into the n-shell and p-core under the built-in electric field, respectively. Thus, photogenerated carrier, separated in the radial direction, can reach the $p - i - n$ junction with much higher efficiency by reducing the substantial bulk recombination. Because silicon's volume changes by four folds upon insertion and extraction of lithium, which causes pulverization and loss of electrical contact in bulk films or micrometer-sized particles, silicon have limited applications as anodes in lithium batteries. The newly silicon-nanowire battery electrodes accommodate larger volume change without damages. Facial strain relaxation in the nanowires allows them to increase in diameter and length without breaking. Efficient electron transport is allowed along the length of individual NW which is connected to the current collector.

2.7 Summary

We have presented relevant background information of one-dimensional nanostructures, including fabrication techniques, growth mechanism and potential applications. However, nanowires produced by the conventional silicon-wafer-based approach with inherent limits in micrometer-length-scale, mechanical fragility, and a lack of global orientation, make their manipulation, integration, and macroscopic assembly extremely difficult. Thus an alternative fabrication method with capacity to produce extended and ordered nanowires is highly desired for large-area nanowire-based devices. We will move the discussion from traditional VLS growth method to a top-down approach of optical-fiber thermal drawing, in which thin-film filamentation occurs upon reaching a characteristic thickness down to nanometer scale in a new class of multimaterials fiber as discussed in the following chapters.

Chapter 3

Multilayer multimaterial fiber

3.1 Introduction

The previous chapter 2 described motivation, fabrication, growth, and applications of 1D-nanostructures. Conventional silicon-wafer-based approach such as vapor-liquid-solid growth is inherent with low throughput and limited length of nanowires, representing a technical difficulty for their large-area cost-effective applications. It is interesting to explore an alternative cost-effective method. In this Chapter, we will introduce a new platform of multimaterial fibers fabricated by a top-down approach of thermal drawing. In the following chapters, we will present that an instability of a thin cylindrical shell results nanofilaments arrays during thermal drawing.

Optical-fiber thermal drawing, a well-established top-down method, has been employed for producing kilometer-long silica fibers with uniform dimensions in the telecommunication industry. The first step of thermal drawing is the fabrication of a cylindrical object called a preform, which is identical in its geometry and composition to the final designed fiber, but is much larger in its cross-sectional dimensions and shorter in length. The second step is heating this preform into viscous state and stretching the preform into extended fibers under the applied axial stress.

The most widely used conventional optical fibers transmit light through a solid core of doped silica (SiO_2) glass using the mechanism of index confinement, or total internal reflection (figure 3-1a) [29], [30], [31]. In the last decade, microstructured

fibers incorporating air enclaves have been created with these methods, resulting in photonic band gap fibers (figure 3-1b). All these fibers, however, consist of a single material with the possible addition of air cavities. The fact that these fibers consist of a single dielectric material limits their applications in optical transmissions.

A new class of fibers incorporating multiple materials (e.g., semiconductor, insulators, and metals) has been developed [32]. These fibers allow one, in principle, to incorporate the functionality of a semiconductor device into a fiber. Furthermore, these fibers contain periodically alternative layers of an insulating polymer and a semiconducting glass of prescribed thickness, thus forming a cylindrical omnidirectional mirror or Bragg mirror (figure 3-1c). This multilayer structure is designed to efficiently reflect light at low loss and wide angular range.

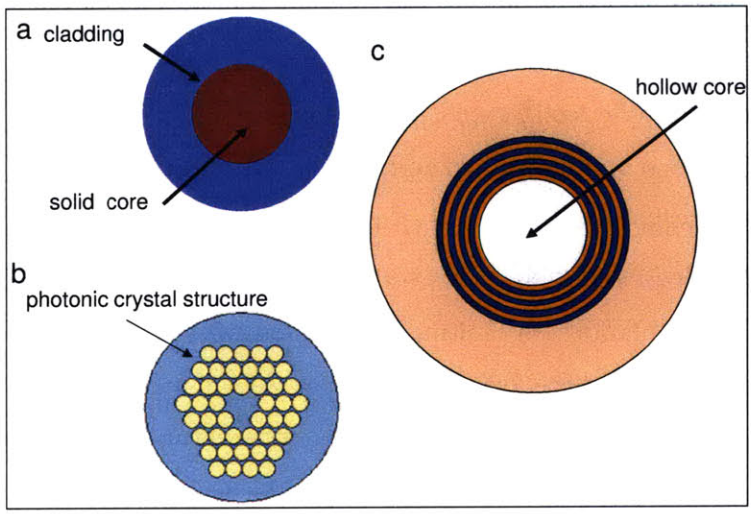

Figure 3-1: A comparison of representative cross-section view of different type fibers. **a,** conventional fiber, **b,** 2D microstructured fibers, and **c,** 1D multimaterial multilayer fibers.

3.2 Cylindrical omnidirectional mirror

Exploration of Bragg reflection from periodic concentric cylindrical layers, as a mechanism for light guidance in a hollow core, was proposed in 1970*s* [33]. The further

quantitative analysis and experimental realization were reported in references [34], [35], [36]. In order to achieve low-loss omnidirectional reflectivity in the 1D finite periodic structure shown in figure 3-2a, necessary conditions must be met on large contrast of refractive index n_H/n_L and on the ratio of the lower index to the ambient n_L/n_A. A photnic band gap diagram for both TM and TE is shown in figure 3-2b. Externally incident light in the range of frequencies in the grey can not couple to any propagating states within structure and will be reflected.

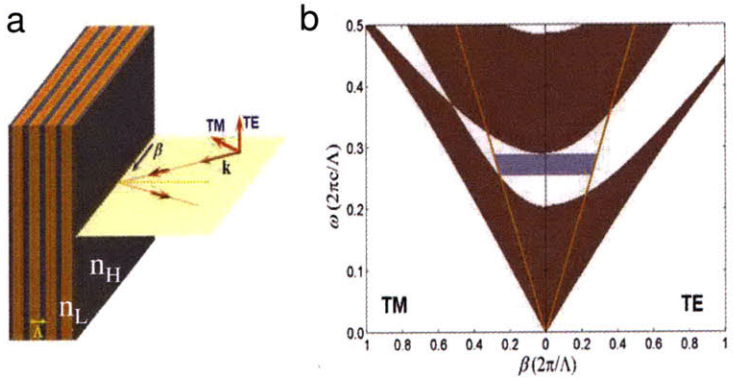

Figure 3-2: **a,** A 1D planar dielectric multilayer structure composed of alternating layers of indices n_L and n_H of period Λ; **b,** TE and TM band diagram of the structure. Propagating states in brown whereas forbidden states in white. Adapted from [32].

3.3 Materials selection

Realization of this structure by traditional thermal drawing has two primary difficulties of sub-wavelength periodicity of multilayer and high-index contrast with similar thermo-mechanical properties. Previously it has been considered unusual to achieve this by a recent statement that "[optical] fibers are limited by the small refractive index contrasts attainable between the core and cladding materials (which need to be thermally compatible)" [37].

The identified materials can be co-drawn together with the capability of maintaining the geometry from preform to fiber during thermal drawing. The main requirements in the materials used in the thermal drawing are as follows:

- At least one of fiber materials can support the draw stress and yet continuously deform; thus at least one material is amorphous resisting divitrification, so that fiber is drawn at a reasonable speed with self-maintaining structural regularity in a furnace-tower process.
- The respective softening point is below the drawing temperature, so all the materials can flow in a viscous state during drawing.
- Materials should exhibit good adhension/wetting in the viscous and solid states without cracking even when subjected to rapid thermal cooling and quenching.
- Additional optical restrictions: high index-contrast satisfies the criteria for the omnidirectional reflection, and low optical absorption over a common wavelength band allows the penetration depth smaller than the absorption length.

Chalcogenide semiconductor glass and thermoplastic polymers are identified as suitable materials pair to meet all the above requirements. Chalcogenides are high-index inorganic glasses that contain one or more of the chalcogen elements including sulfur (S), selenium (Se), and tellurium (Te) and generally contain no oxygen. They have glass-temperatures in a range between $100 \sim 400\,^{o}$C, refractive index between $2.2 \sim 3.5$, and are transparent in the infrared region. Thermoplastic polymers match the thermal properties of chalcogenide glass in a thermal co-deformation process. They have lower softening temperature and turn to a liquid when heated and freezes to a very glassy state when cooled sufficiently. Examples of polymer used in fiber include polyethersulfone (PES), polyetherimide (PEI), and polysulfone (PSU). The wide variety of polymers available, the feasibility of processing them in film form, and their excellent mechanical toughness make these materials principal candidates for combination with chalcogenide glass in our composite PBG fibers.

3.4 Fabrication process

After identifying the compatible materials, we will move to the fabrication process of cylindrical fibers with alternative layers of glass and polymer. The fabrication

process has four main steps (See figure 3-3a). (i) An amorphous semiconductor film of desired thickness is thermally evaporated onto an amorphous polymer substrate. (ii) The semiconductor/polymer bilayer film is tightly wrapped around a polymer tube. (iii) Additional layers of protective polymer cladding are then rolled around the structure. In this way, a multimaterial preform is formed in which the semiconductor film is completely enclosed between polymer layers. (iv) The preform is fused into a single solid structure by heating the structure under vacuum. The solid preform is heated into the viscous state and controllably stretched into an extended fiber by the application of axial tension.

Fibers with layer structures have been successfully achieved from optical-fiber thermal drawing. Tens-of-meters long fibers with a uniform diameter have been produced, as seen from the inset of figure 3-3a (iv). The cross-section and semiconductor layer of fiber (see figure 3-3c) do not change during drawing; they are simply a scaled-down version of preform structure (figure 3-3b). The semiconductor film geometry is important in structures such as cylindrical multilayer photonic bandgap fibers and sensitive optical and thermal fiber detectors.

3.5 Multifunctional fibers

These building blocks of diverse materials (insulator, metal and semiconductor) make the multi-functionalities in a single fiber possible, which have not been thought of before [38]. A variety of composite multimaterial fibers have been developed and are summarized in figure 3-4. In (a) and (b), alternating layers of high and low refractive index form a Bragg mirror with a photonic band gap that efficiently reflects light of a broad range of wavelength from the mid-IR to the UV regime by simply changing the layer thicknesses [39]. This photonic band gap lines a hollow core to guide and transmit light through the fiber (a) or is wrapped around the outside of the fiber to reflect externally incident light as a bar code (b). (f) and (g) demonstrate the ability to guide or reflect light of different wavelengths. The multilayer Bragg mirror may also be combined with a gain medium as in part (c) to create a fiber laser, in which

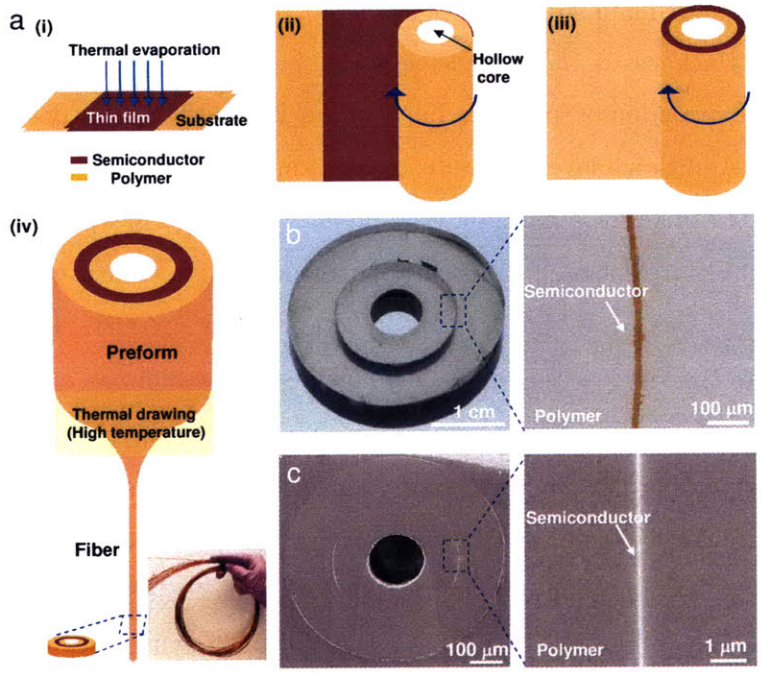

Figure 3-3: fabrication process of fiber. **a,** (i) Thermal evaporation of a glass film on a polymer substrate; (ii) wrapping film around polymer rod with a hollow core; (iii) cladding the film with polymer matrix; (iv) thermal drawing from preform to fiber with the layer structure retained. Inset is photograph of tens-of-meters long fiber. **b,** An optical microscope image of the layer structure in the preform is shown on the left, and a magnified section of the thin film on the right. **c,** SEM micrograph of the fiber cross-section is shown on the left, and a magnified section of the intact semiconductor thin film, right, confirms that the layered structure is preserved.

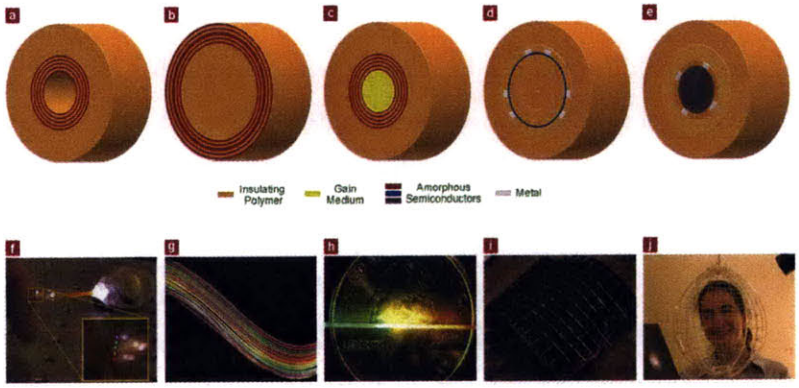

Figure 3-4: (top row) schematic diagrams of **(a)** optical transmission fibers, **(b)** optical reflection fibers, **(c)** surface emitting fiber laser, **(d)** thin-film photodetecting fiber, **(e)** solid core photodetecting fiber. (bottom row) Experimental demonstrations of the above devices.

the Bragg mirror not only guides the pump light along the axial direction but also functions as a resonator cavity in the radial direction. The resulting laser emission comes from the surface of the fiber in the direction perpendicular to the pump light, as shown in (h) [40]. Parts (d) and (e) represent the incorporation of metals into the fibers and their connection to the chalcogenide semiconductor to form photo- or thermal- detecting devices. The semiconductors may be in the form of either a thin film (d) or a bulk rod (e) [41]. In either case, the devices can function as individual extended detectors and be assembled into fabrics and arrays of fibers for large area signal detection.

3.6 Transmission hollow-core fiber

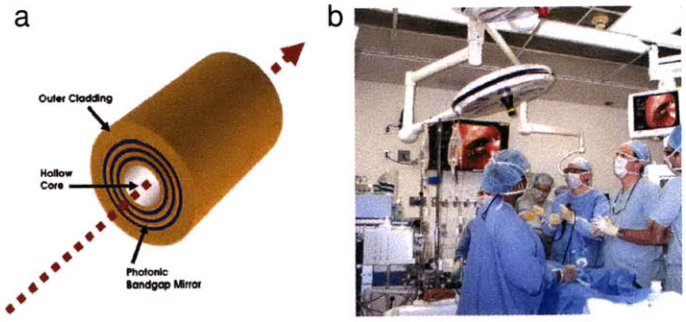

Figure 3-5: **a,** Low-loss waveguide of light along hollow core; **b,** fiber application in the non-invasive medical surgery.

In order to demonstrate the new opportunities of these multifunctional fibers, hollow-core PBG transmission fiber will be taken as an example [36]. Most widely used conventional silica fibers transmit light through a solid core of doped silica (SiO_2) glass using the mechanism of index confinement, or total internal reflection. Index-guided systems have certain fundamental limitations associated with the propagation of light through a solid material, stemming from the fundamental optical properties of the transmitting medium such as non-linear effects (associated change in the refractive index of the material with varying light intensity), light absorption by electrons or phonons, light scattering caused by microscopic density fluctuations (Rayleigh scat-

tering), material dispersion (wavelength-dependent variations in refractive index).

This transmission fiber, as seen in figure3-5a, consists of a hollow air core surrounded by multiple alternating submicron-thick layers of a high-refractive-index glass and a low-index polymer, resulting in large infrared photonic bandgaps. Tens of meters of hollow photonic band gap fibres for transmission of carbon dioxide (CO_2) laser light at 10.6 μm wavelength were drawn. The transmission losses were found to be less than 1.0 dBm^{-1}, demonstrating that the waveguide losses are orders of magnitude lower than the intrinsic fiber material losses. Furthermore, high-power CO_2 laser light was delivered with densities exceeding 1.3 $kWcm^{-2}$. CO_2 lasers have been used for non-invasive upper airway surgery due to excellent laser-tissue interactions. These flexible fibers allow surgeons to gain access to otherwise inaccessible areas by line-of-sight techniques such as trachea, nasal canals, ears, and even neuro surgery, as seen in photograph of figure 3-5b.

3.7 Ultimate feature size of layer thickness

One intriguing property of the aforementioned transmission fibers is the scalability of wavelength by changing layer feature size. The mechanical flexibility and cross-section view of hollow-core fiber is shown in figure 3-6a, and b, respectively. The fundamental photonic band gap of these hollow-core fibers ranges from UV, visible, NIR and the MIR regions by identifying the transmission peak. Scanning electron microscope (SEM) imaging of the layers (figure 3-6c,d) reveals that the final layer thicknesses correctly correlate to the measured transmission peaks (figure 3-6e). Hollow-core cylindrical PBG fibers have been produced with fundamental band gap at 350nm (UV), at 750 nm (NIR) for biomedical applications, at 1.5 μm (NIR) for use in telecommunications applications, at 2.94 μm (MIR) for the transmission of high-energy Er:YAG laser radiation, and at 10.6 μm (MIR) for laser surgery and materials processing.

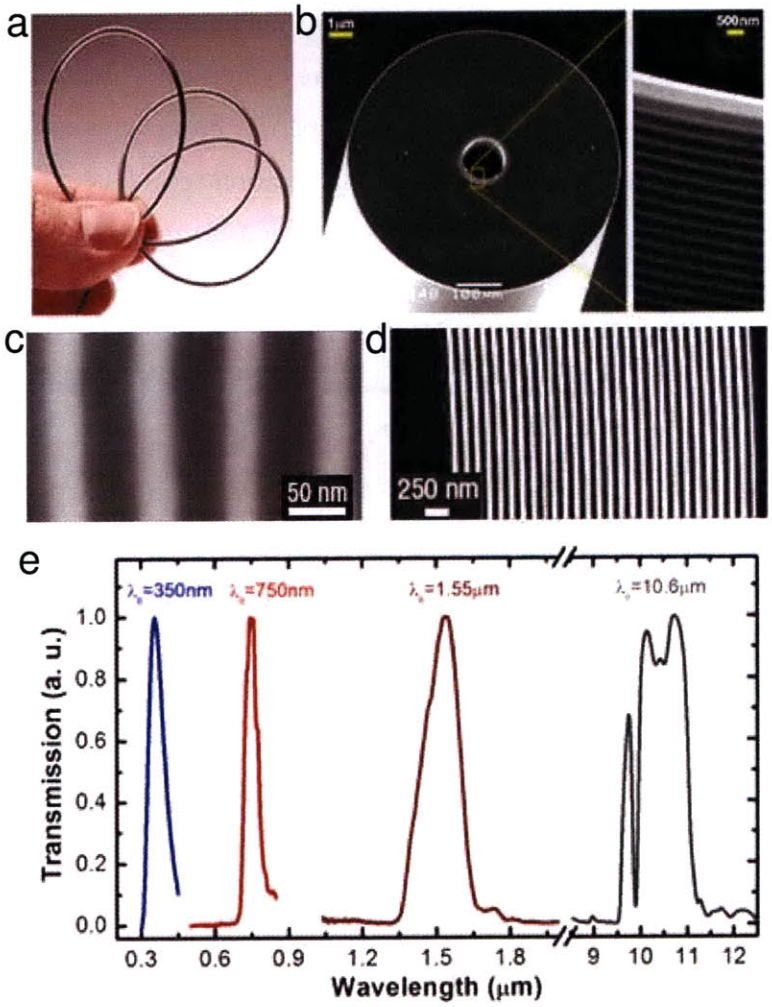

Figure 3-6: Wavelength-scalable hollow-core fiber. **a,** A flexible, hollow-core, PBG fiber; **b,** An SEM micrograph of a hollow-core PBG fiber cross-section; **c, d,** SEM micrographs of the omnidirectional reflecting multilayer structures lining the hollow fiber core for UV (**c**) and NIR (**d**) transmission peaks; **e,** Wavelength scalability of hollow-core PBG fibers. Transmission spectra of four fibers, differing only in the period of the multilayer structure, with peak wavelengths λ_0 at $10.6\,\mu$m, $1.55\,\mu$m (corresponding to the structure in d), 750 nm, and 350 nm (corresponding to the structure in **c**).

3.8 Summary

In this Chapter, we have focused on a new class of microstructured fiber, multilayer multimaterial fiber. The mechanism of light guidance is photonic band gap which is formed by high-index-contrast of alternative cylindrical layers. Material system need be compatible with thermomechanical properties at a common temperature window to ensure the co-drawing process. The fabrication technique relies on the top-down method of thermal drawing. The unprecedent feature size from micrometers down to submicrometers has been maintained, allowing a broad range wavelength scaling from IR to UV in the fiber.

Chapter 4

Thin-film-breakup into filament arrays

4.1 Introduction

We have discussed in Chapter 2 nanostructures that are typically synthesized by bottom-up methods with small-volume yields. In Chapter 3, we have presented multilayer multimaterial fibers that are fabricated by a top-down approach of thermal drawing. In particular, the unique geometry of cylindrical shells with thickness down to submicrometers have been demonstrated in these multilayer fibers. We pose a question that whether it would be possible to use our thermal drawing technique to incorporate nanostructures into the platform of microstructured fibers.

This objective naturally entails a decrease in feature dimensions. However, what happens to extremely thin films during the top-down thermal drawing process has not been explored. One may reasonably expect that surface-energy-driven instabilities while the preform is in the viscous fluid state will impact the resulting geometry. In fact, this approach may be viewed as a test bed for studying such instabilities with several distinct and unique advantages. The effect of shrinking the liquid film (or other structures of interest) may be studied over a very wide range of parameters and can be finely controlled during the fiber-drawing process. The produced structures are 'frozen' into the fiber so that they may be directly observed by both cross-sectional

and axial inspection, and quantitative conclusions concerning stability limits of the feature size can be made.

4.2 Azimuthal instability of layer

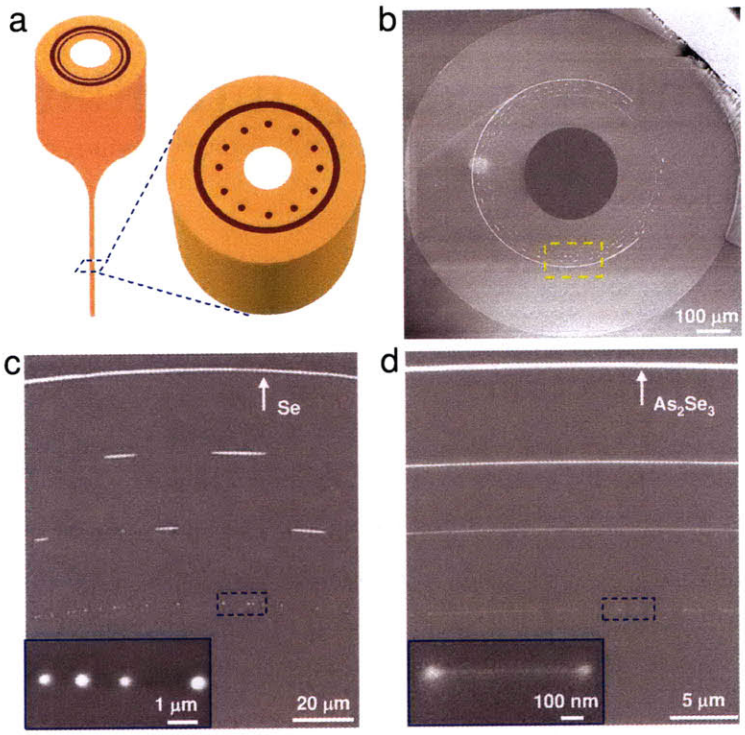

Figure 4-1: Breakup of layers at the nanometre scale. **a,** Sketch of the preform with multiple films of decreasing thickness and fiber cross-section indicating breakup of thinner layers. **b,** An SEM micrograph of whole cross-sectional view of fiber; inset showing that average spacing of break-up segments varies linearly with the final layer thickness. **c,** Magnification Se/PSU fiber cross-section (the final layer thicknesses in fiber are $700, 96, 65$ and $17\,\text{nm}$, respectively) showing that the layers are broken when pulled to below $100\,\text{nm}$ thickness; inset for a further magnified section of the $17\,\text{nm}$ layer. **d,** Magnification As_2Se_3/PES fiber cross-section (the final layer thicknesses in fiber are $270, 70, 14$ and $3\,\text{nm}$, respectively) showing that the layers are maintained to sub $-$ $15\,\text{nm}$ thickness; inset for a further magnified section of the $3\,\text{nm}$ layer.

In order to investigate the smallest achievable thickness of the thin glassy film, we

have studied multiple material combinations. Two amorphous semiconductors (Se and As_2Se_3) and two polymers (polysulphone, PSU, and polyethersulphone, PES) were used in two combinations (Se with PSU and As_2Se_3 with PES). The materials in the pairings have similar thermo-mechanical properties in an overlapping temperature range as well as good adhesion through repeated thermal cycling, both properties being crucial to facilitate co-drawing of the two different materials.

To isolate the effect of film thickness, a fiber preform consisting of several concentric amorphous semiconductor films having decreasing thicknesses was prepared for each material combination (as depicted schematically in figure 4-1 a) [42]. The preform was consolidated under vacuum for approximately one hour at $\sim 260\,^{\circ}C$ or $220\,^{\circ}C$ for As_2Se_3/PES and Se/PSU combination, respectively. To draw tens of meters of fiber from cylindrical preforms measuring 160 mm in length and 20 mm in diameter, a conventional optical fiber draw tower consisting of a three-zone furnace to heat the preform to its processing temperature (mid-zone set to $\sim 300\,^{\circ}$C for As_2Se_3/PES and $\sim 260\,^{\circ}$C for Se/PSU fibers), a feeding process to controllably introduce the preform into the furnace (downfeed speed of $0.003\,\mathrm{mm}\cdot\mathrm{s}^{-1}$), and a capstan to pull the resulting fiber from the preform (set at was $\sim 0.1\,\mathrm{m}\cdot\mathrm{min}^{-1}$) were used. The drawing parameters were fixed to keep a constant draw-down ratio of about 20 between the diameter features sizes of the initial preform and final fiber.

SEM micrographs of fiber cross-section (figure 4-1 b) show that the thicker semiconductor layers remain intact after drawing, but thinner layers break up. A striking difference in film stability is highlighted in a magnification of fiber cross-sections for Se/PSU (figure 4-1 c) and As_2Se_3/PES (figure 4-1 d). Only the thickest Se layer remains intact after drawing, with the three thinner layers experiencing circumferential breakup (figure 4-1 c). The thinnest Se layer completely breaks up into circular cross-sectional features. In contrast, all the As_2Se_3 layers remain intact above 10 nm, with layer breakup occurring only in the thinnest $3-$ nm layer (figure 4-1 d).

4.3 Continuous filaments

Given these observations of circumferential layer breakup in the fiber, the question of axial stability naturally arises. To facilitate the observation of the axial behavior, we prepared new preforms with single thin Se films designed such that the layer would be 100 nm (figure 4-2 b,c) and 800 nm (figure 4-2 d,e) after drawing (figure 4-2 a). The 100 nm layer was expected to break up while the 800 nm layer should remain intact (figure 4-1 c). Photographs in figure 4-2 b,d demonstrate the color and mechanical flexibility of the fibers. Axial inspection of the fibers reveals axially continuous Se filaments form in the 100 nm-layer fiber (figure 4-2 c) while solid brick-red color characteristic of a-Se spans the length of the 800 nm-layer fiber. Combining the cross-sectional (figure 4-1 c) and axial (figure 4-2 c) information of the filament, we conclude that the a-Se and As_2Se_3 filaments have a ribbon-like three dimensional structures (approximately 100 nm x 10 nm x length and 10 nm x 100 nm x length of fiber, respectively).

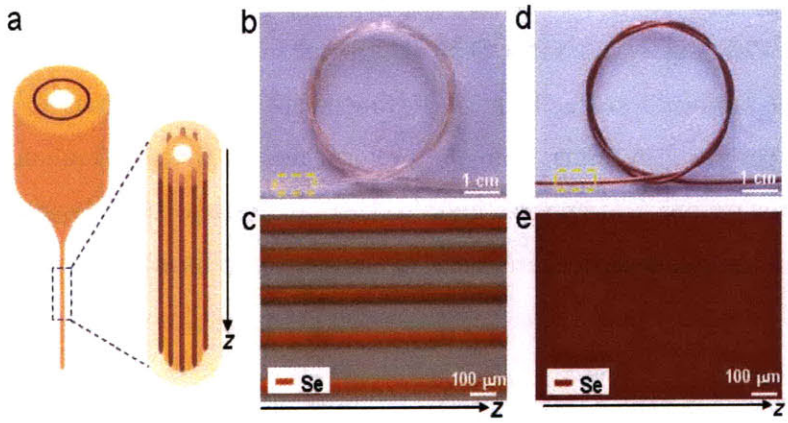

Figure 4-2: Extended and ordered filament arrays embedded in the fiber. **a,** Sketch of the preform with a thin film and fiber with the extended filaments after layer breakup. **b,** Photograph of a Se/PSU fiber exhibiting cross-sectional break-up of the layer the $sub-100-nm$ layer. **c,** Optical microscope image taken along the length of the showing extended amorphous Se filaments embedded in this fiber. **d, e,** Photograph and optical microscope image of a Se/PSU fiber with a thick Se film that does not breakup.

The reproducibility of the extended filament has been confirmed by several inde-

pendent fiber drawings in both Se/PSU and As_2Se_3/PES system with different film thickness. Se/PSU fibers were drawn from preforms with the initial Se film thickness 6 μm, 1 μm, and 200 nm. As aforementioned, the thickest Se film remains stable as seen from the optical microscopic image of figure 4-3a. Figure 4-3b and c show the continuous filaments without breakup for the hypothetical layer thickness down to 50 nm and 10 nm, respectively. For the other As_2Se_3/PES fiber, the filaments remain parallel with the hypothetical layer thickness down to 10 nm in figure 4-3 d. We have not found any axial breakup of filaments, though the branching and recombination of the filaments appear rarely, thought to be due to defects. Thus, the well-ordered parallel filament arrays span the entire fiber length.

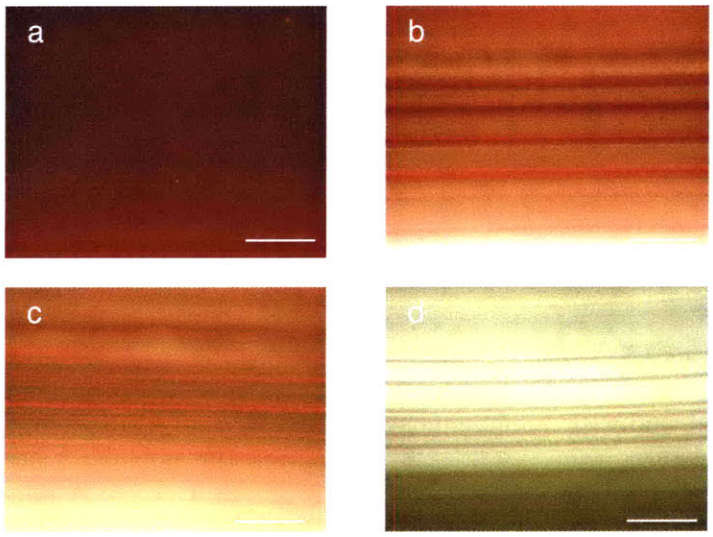

Figure 4-3: Reproducibility of in-fiber filaments. **a,** Stable film, **b,c,** Se filaments from hypothetical layer thickness 50 nm and 10 nm , respectively. **d** As_2Se_3 filaments from hypothetical layer thickness 10 nm. Scale bar is 100 μm

An intriguing feature of this phenomenon is the potential use of these semiconductor filaments after extraction from the polymer matrix (figure 4-4 a). Indeed, the polymer matrix is easily dissolved away by a solvent (dimethylacetamide), leaving filament arrays for possible further processing. Examples of the extracted filaments are given in figure 4-4 b-c. Figure 4-4 b shows a 1 mm long Se filament extracted from a fiber composed of 100 nm thick Se layer that has broken up (the same fiber

as figure 4-2 c). A bundle of As_2Se_3 filaments extracted from an As_2Se_3/PES fiber (from a As_2Se_3-thin-film preform) is shown in figure 4-4 c. Individual filaments have $sub-100-$ nm width and $10-$ nm thickness.

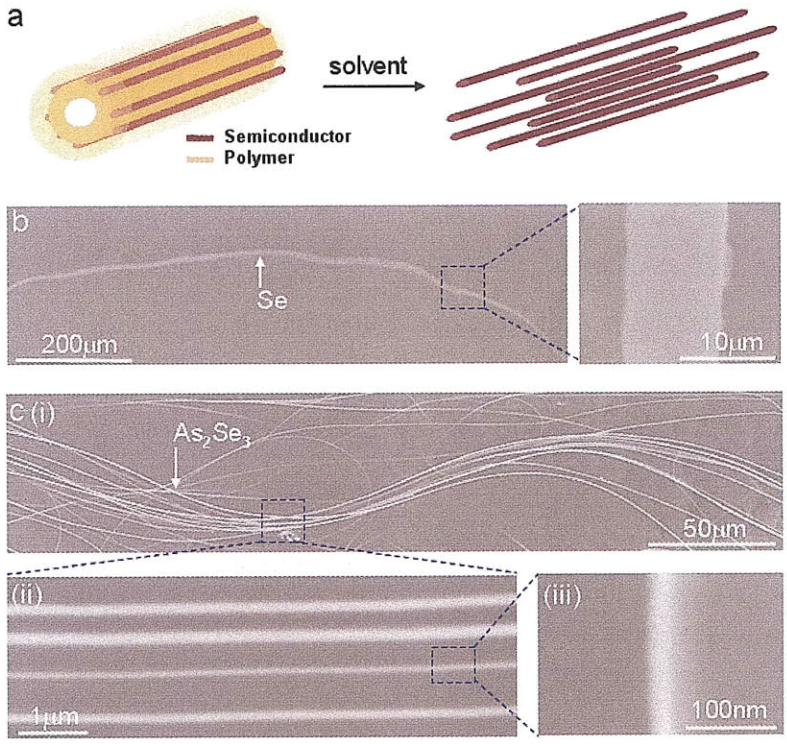

Figure 4-4: Semiconductor nanofilaments extracted from a fibre. **a,** The filament bundles are extracted from the fiber by dissolving the polymer matrix. **b,** SEM micrograph of a Se filament and a magnified section of it. **c,** (i) A bundle of As_2Se_3 filaments. (ii) Magnified section showing parallel filaments. (iii) A section of a single filament.

The total length of nanofilaments produced with this method is especially captivating. For example, the semiconductor film in a typical fiber-preform is 10 cmlong, 3 cmwide (the preform circumference) and hundreds of nanometers in thickness (these dimensions are by no means limits, but are simply experimentally convenient). From this preform, forty meters of fiber may be produced if it is drawn down by a scaling factor of 20. The number of filaments in the fiber is around 10^2 (diameter of fiber is 1 mm and spacing between filaments is around 10 μm). Thus a total filament length on the order of four kilometers can be produced from a single semiconductor sheet clad in

a polymer preform. This unique feature is due to the transition in dimensionality from a 2D sheet into 1D filament arrays. Because the fiber dimensions may be easily changed and the fiber drawing process may have draw down ratios much greater than 20, kilometer-long nanofilaments are readily obtainable, many orders of magnitude longer than other approaches to nanowire production. Note that this is achieved in the form of hundreds of nanofilaments all possessing global orientation in fiber form.

4.4 Instability evolution and wavelength

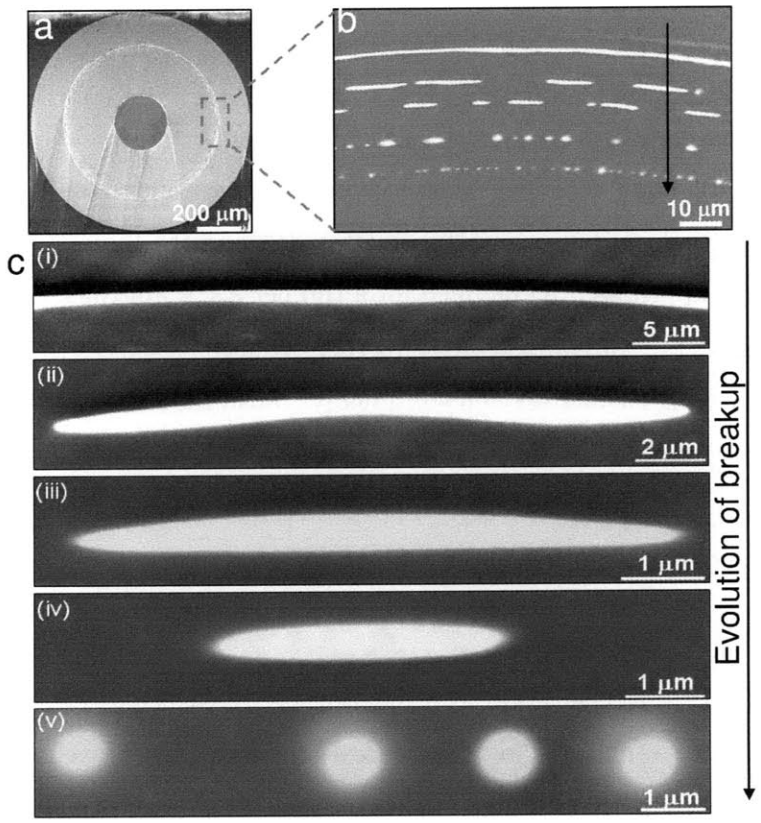

Figure 4-5: Evolution of instability in the structure of graded-thickness layers. **a** and **b** for an SEM micrograph of cross-section and multilayer structure; **c,** A close-up SEM for the evolution of instability for initial film thicknesses of $6, 3.4, 1.8, 0.8$ and $0.2\,\mu$m, respectively. Bright and dark color for glass Se and polymer PSU, respectively.

To reveal the evolution of entire breakup process, we design a graded-thickness

multi-layer structure in a single preform to draw fiber. Advantage of this structure design is the elimination of many uncontrollable factors that might affect film breakup such as thermal cycling of consolidation and thermal drawing of fabrication. The tendency of breakup is readily accessible by a cross-section view, as the produced structures are frozen in fiber. Cylindrical preform was made of five concentric selenium (Se) films with the graded thicknesses ($6, 3.4, 1.8, 0.8$ and $0.2\,\mu$m, respectively), which are embedded in polysulfone (PSU) polymer matrix. Fiber was drawn with a scaling factor of 20 at temperature about $260\,^{\circ}$C. A scanning electron microscope (SEM) micrograph of a fiber cross-section is shown in figure 4-5 a. figure 4-5b is the magnified view of five Se layers (bright color) with initial film thicknesses of $6, 3.4, 1.8, 0.8$ and $0.2\,\mu$m, respectively.

Figure 4-5 c(i)-(v) displays a close-up view of each individual layer in the order of thickness. (i) Perturbations or fluctuations occur in the thickest $6-\mu$m-thick layer. (ii) Small amplitudes are amplified for a thinner $3.4-\mu$m-thick layer, rupturing into many segments. (iii) and (iv) At further reduced thickness of 1.8 and $0.8-\mu$m-thick layer, long-slender segments gradually transform into short segments by surface tension. (v) Eventually, circular shapes arise for the thinnest $0.2-\mu$m-thick layer. Evolution of entire process of instability and break-up at different stages indicates that surface tension is associated with breakup.

Instability wavelength (λ) as a function of layer thickness (e) with a square-root relationship ($\lambda \sim e^{1/2}$) is shown in figure 4-6 (red circles). Wavelength is measured by averaging spacing between break-up segments in figure 4-5c (for stable layer of figure4-5c (i), wavelength is the distance between maximum width). Error bar of wavelength and thickness is due to statistic error and variation of fiber diameter. In addition, data of instability wavelength dependent on thickness from previous experiments is plotted in figure 4-6 (gray squares). All these data are fitted well by square-root curve $\lambda \approx ce^{1/2}$ with coefficient $c \approx 14$ (blue-solid line).

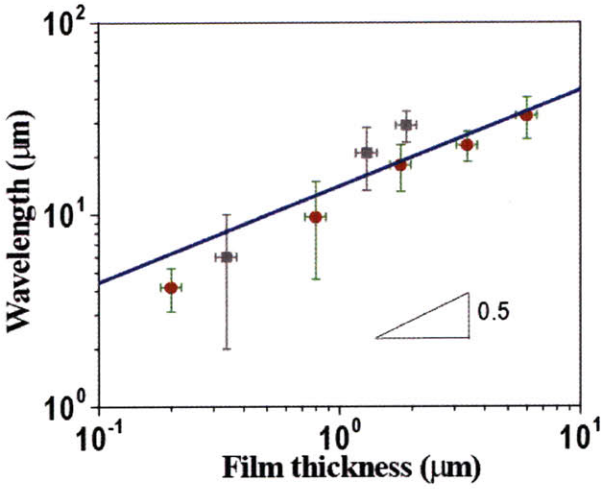

Figure 4-6: Instability wavelength has a square-root relationship with thickness ($\lambda \sim e^{1/2}$). Red circles for current experiment, and gray squares for previous experiment. These data can be fitted well by power-law curve with a slope 0.5, as seen from blue line and gray line.

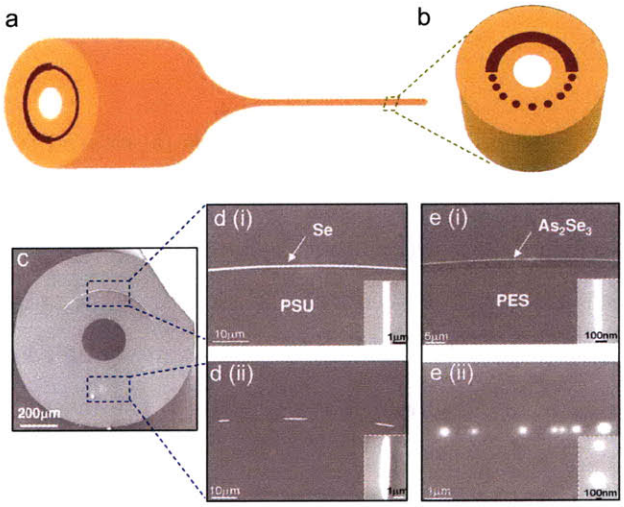

Figure 4-7: Fiber of dual-thickness layer. **a,** Sketch of fiber drawing with the dual-thickness layer structure; **b,** Sketch of fiber cross-section with the fidelity of thicker layer and breakup of thinner layer; **c,** The whole cross-section view of final fiber; **d,** For low-viscosity material set Se/PSU, no breakup of $400-$ nm layer and breakup of $100-$ nm layer; **e,** For high-viscosity material set As_2Se_3/PES, no breakup of $50-$ nm layer and breakup of $4-$ nm layer.

4.5 Instability observations in dual-thickness ring

To check whether physical parameter variables along radial direction is relevant with the azimuth instability breakup, a ring structure with dual thickness is designed in the preform to draw the fibers, as sketch in figure 4-7 **a**, **b**. Because of the cylindrical symmetry during fiber drawing, this structure allows us to study thermal gradient effect.

Two fibers were drew in the Se/PSU and As_2Se_3/PES system. A thin glass film (Se or As_2Se_3) is thermally evaporated on the polymer substrate (PSU or PES, correspondingly). Next, half of glass film is shielded while the other half continues growing. Then this dual-thickness film is rolled directly around a polymer cylinder to obtain the preform, which is placed into furnace, heated into viscous state at high-temperature zone. The fiber is stretched down from preform by the pulling tension with a scaling factor about 20.

For Se/PSU material combination, a fiber is fabricated to have dual-thickness Se ring-layer structure (400, 150 nm for thick and thin part, respectively). SEM image of a whole cross-section view of this fiber is shown in figure 4-7 **c**. Thick layer of 400 nm thickness layer is clearly presented by SEM close-up view in figure 4-7 **d** (i), and inset reveals layer thickness. The breakup of $100-$ nm thinner layer is demonstrated by figure 4-7**d** (ii), and one segment is revealed from the inset.

For the other As_2Se_3/PES system, a fiber is fabricated to have dual-thickness As_2Se_3 ring structure as well (50, 4nm for thick and thin part, respectively). The $50-$ nm thick layer remains intact and $4-$ nm layer has broken into circle shape. Over $20-\mu$m long As_2Se_3 layer is shown in figure4-7 **e**(i) with $50-$ nm thickness from the inset SEM. figure4-7 **e** (ii) presents the targeted As_2Se_3 layer of 4 nm is broken into many droplets, which are conformed by inset of high-resolution SEM.

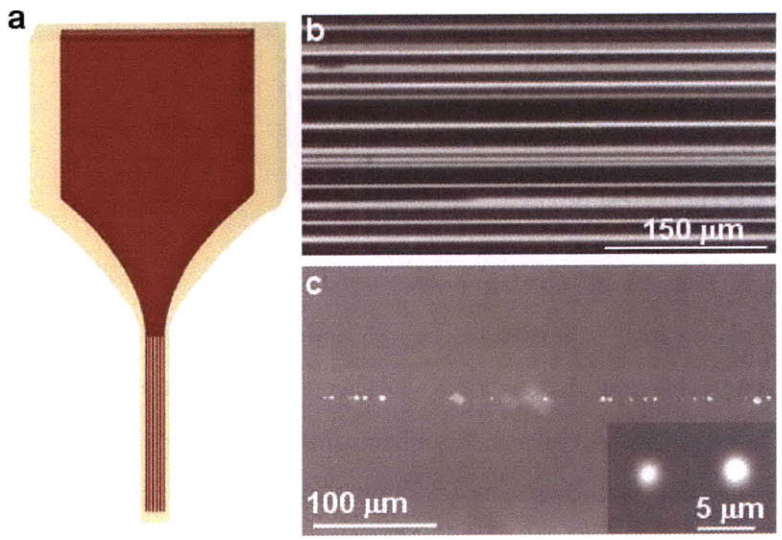

Figure 4-8: Filamentation of thin film in the ribbon fiber. **a,** Sketch of ribbon fiber drawn from a flat preform; **b,** Optical microscope of filaments embedded in the ribbon fiber; **c,** SEM of cross-section of ribbon fiber, indicating breakup of layer into circular shapes. Inset with higher magnification for cross-section. Bright and dark color for glass Se and polymer PSU, respectively.

4.6 Filamentation in ribbon fiber

To check whether circumferential curvature is responsible for the filamentation, another different geometry of flat ribbon fiber is prepared, as illustrated in figure 4-8a. The fabrication procedures are similar to those of cylinder preform. A thermally evaporated $200-\text{nm}-\text{thick}$Se film on a $25-\mu\text{m}-\text{thick}$PSU polymer substrate was clad between thicker PSU plates to form flat preform. After consolidation, plat preform was placed in the furnace and heated above melting temperature into viscous fluid. Ribbon fiber was drawn with a scaling down factor around 20, the same factor as that of cylindrical fiber, to target a hypothetical layer thickness of 10 nm. figure 4-8b shows an optical microscope image of a bundle of filaments embedded in ribbon fiber. figure 4-8c presents the SEM micrograph of cross-section view and indicates the breakup of layer into circular shape. Thin film remains undergoing filamentation in the flat preform during thermal drawing. As expected, the circumferential bending curvature of thin cylindrical shell on the order of 10^{-4} (the ratio between micrometer-thickness

and centimeter-diameter) is negligible, and the circumferential curvature is not likely relevant to the filamentation.

4.7 Summary

We observe a novel physical phenomenon in which a cylindrical thin sheet spontaneously evolves into a periodic array of filaments when the sheet thickness reaches a critical length scale. In contrast to other related phenomena, the axial dimension remains continuous. A controlled and reproducible approach of thermal drawing processing is developed allowing us to follow the fleeting evolution of fluid breakup in a frozen solid state, resulting in unprecedented kilometer-long semiconductor nanofilaments. Hundreds of nanofilament arrays are precisely oriented within a polymer fiber. Moreover, these nanofilaments are hermetically encapsulated in a tough polymer fiber matrix making them environmentally stable. This powerful method offers exciting opportunities for fabrication of nanodevices with virtually unlimited length while maintaining structural integrity in the fiber platform.

Chapter 5

In-fiber crystalline nanowires

5.1 Introduction

Interest in efficient processing of crystalline semiconductor filaments of submicron dimensions is motivated by their unique physical properties and potential for a wide range of applications, as discussed in Chapter 2. Vapor-liquid-solid (VLS) growth has emerged as an important method for the fabrication of high-quality filaments [10]. Nevertheless, filaments produced by the conventional VLS approach are inherently limited to micrometer-length scales, are fraught with mechanical fragility, and lack global orientation. Consequently the manipulation, integration, and macroscopic assembly of filaments have proven heretofore to be extremely challenging. It is instructive to compare this new technology with the traditional approach to optical-fiber fabrication, which is a time-tested technique for producing kilometer-long uniform optical fibers with high throughput and at low cost, as discussed in Chapter 3. Although optical fibers share the cylindrical form factor with filaments, they are produced at much larger dimensions and, furthermore, are usually fabricated out of insulating glasses, not semiconductors. It is therefore intriguing to investigate whether some variant of fiber thermal drawing can be developed to produce semiconductor filaments with much longer lengths than previously thought possible.

Several attempts have been made to fabricate submicrometer-diameter wires directly by the thermal drawing or incorporate micro- and nanowires into optical fibers.

Examples include: two-step drawing of submicrometer-diameter silica wires [43], holey fibers as template [44], [45], and post-processing by filling the holes of air-silica microstructured optical fiber [46]. A two-step drawing process was introduced to further reducing the diameter of silica wire from micrometers down to tens of nanometers [43]. A micrometer diameter silica wire was drawn from a silica fiber by a flame. As seen in figure 5-1a, one end of a micrometer-scale silica wire was then placed horizontally on the sapphire tip, heated to high temperature (about 2,000 K), and winded the wire around the tip by rotating the sapphire tip, resulting in the submicrometer or nanometer-diameter silica wires. A tapered sapphire fiber (figure 5-1b) was used to absorb the thermal energy from the flame to obtain a steady temperature distribution in the drawing region for the production of uniform diameter down to nanometers. The mechanical flexibility of silica wires were demonstrated by a knot in the SEM image of figure 5-1c. These silica wires represent miniaturization of subwavelength-diameter optical waveguide as building blocks for microphotonics devices and for high-bandwidth optical communication system.

Another method is using hollow core of fiber as a template to growth nanowires [44], [45], as seen in figure 5-1d. Generally, deposition within micro to nanoscale diameter chamber is difficult due to the larger aspect ratio, and high pressure is necessary to overcome the mass-transport constraints inside the micron sized holes. High-pressure of silane/helium precursor up to 30 MPa enters a pore from the left side, and single crystal silicon is deposited behind a gold catalyst particle moving towards the left side. figure 5-1e presents an SEM image of wires with a smooth surface, which are etched out of the silica matrix. Furthermore, post-drawing processing, to insert semiconductors and metals into the holes of air-silica microstructured optical fiber, is complicated by a pumping-and-filling technique [46]. After drawing the microstructured fibers made of silica and air, the holes except the selected ones on the fiber end-face are closed. Molten materials (gold, silver, or germanium) were pumped into the remaining open holes. A single wire made of germanium with diameter around 2 μm was shown in SEM image of figure 5-1f. In addition, another method is the multiple step draw-cut-stack technique in which a powder or rod of material is inserted

into a glass tube, drawn down into a fiber, and the resulting fiber sections are stacked together to form a new preform that is drawn down again [47]. Silicon-core optical fibers have been fabricated with this method, but further efforts are needed to reduce the semiconductor dimensions, currently at hundreds of micrometers in diameter [48].

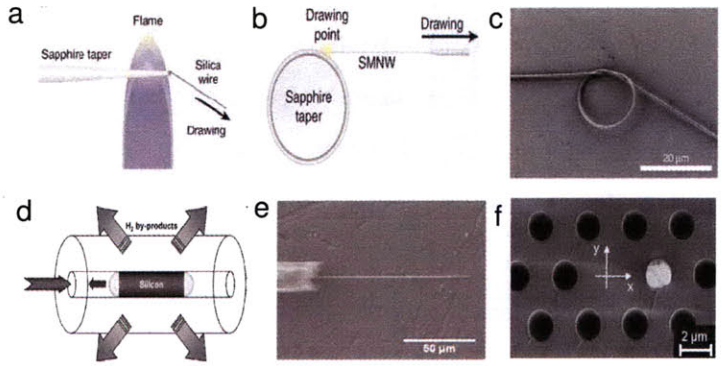

Figure 5-1: Overview of nanowires fabricated by thermal drawing. **a,** Schematic diagram of drawing submicrometer wire from a coil of micrometer-diameter silica, **b,**Magnified view of the drawing process, the sapphire taper for the steady temperature distribution in the drawing region, **c,** A microscopic ring with diameter around 15 μm showing the flexibility of silica wires. Adapted from [43]. **d,**Schematic of deposition growth process inside a fiber template, **e,** SEM micrograph of wire etched from fibers. Adapted from [45]. **f,** SEM of a fiber cross-section microstructure with a single germanium (Ge) wire of diameter around 2 μm (white color). Adapted from [46].

While combining crystalline filaments with optical fibers has generated a lot of interest, several challenges to producing nanowires using thermal drawing remain which are a consequence of the orders-of-magnitude disparity between typical fiber and filament dimensions. Moreover, the above described approaches do not take full advantage of the fundamental simplicity of the traditional fiber thermal-drawing process which is, nevertheless, at odds with the desire to produce crystalline structures.

5.2 Thin-film filamentation by thermal drawing

To fabricate extended crystalline semiconductor nanowires, we implement a one-step optical-fiber co-drawing process, which is based on an intriguing phenomenon where

a viscous semiconductor film spontaneously evolves into a periodic array of nanowires [49], as illustrated in figure 5-2a. First, a macroscopic preform is constructed by wrapping layers of polymer film and an amorphous semiconductor around a mandrel and fusing the layers into a single solid structure (figure 5-2b). After removing the mandrel, the completed preform is heated until it becomes viscous and is controllably stretched by the application of axial tension into an extended fiber (figure 5-2c). When the thickness of the semiconductor layer drops below a characteristic length scale during fiber drawing, it spontaneously breaks up into an ordered array of nanowires. This length scale is determined by the viscosity of the two materials and their surface energy.

This novel process has several unique advantages. First, nanowires have unprecedented lengths, in principle, extending along the entire tens-of-meters-long fiber. Secondly, the process aligns all nanowires in the same global orientation. Thirdly, the mechanically tough polymer matrix hermetically seals the nanowires into a structure that may be macroscopically manipulated, bypassing problems associated with the mechanical fragility of nanostructures. Additionally, the approach is compatible with a variety of materials including metals and semiconductors. In this paper, we focus on the semiconductor selenium (Se), which exhibits many interesting properties such as excellent photoconductivity, large piezoelectric and thermoelectric coefficients [50], [51], and high mercury affinity for potential use in mercury remediation applications [52].

5.3 Thermal crystallization

Fiber was prepared by drawing a preform. A thin film of Se (modified with 2 atomic percentage sulfur to depress the alloy melting temperature) was thermally evaporated onto a polysulfone (PSU) polymer film. Macroscopic preforms having $2 - cm$ outer diameters were fabricated by rolling the chalcogenide films and polymer cladding layers onto a PTFE mandrel and consolidating the structure under vacuum at $\sim 220\,^{\circ}\mathrm{C}$ for approximately one hour, after which the mandrel was removed. A conventional

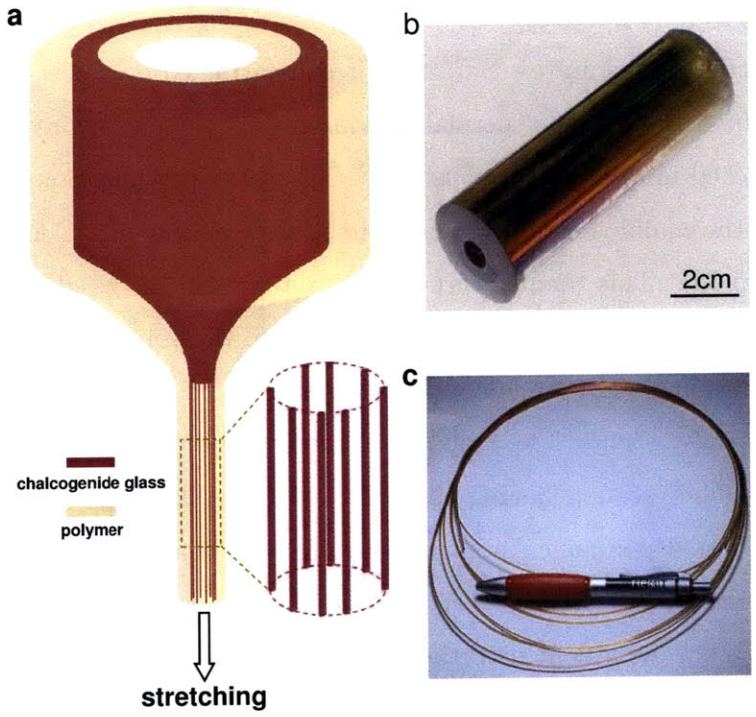

Figure 5-2: Fabrication of nanowire arrays using the optical-fiber thermal drawing technique. **a,** Schematic diagram of break-up of a thin cylindrical shell into a periodic array of nanowires. During thermal drawing, a macroscopic preform is heated into the viscous state and controllably stretched into an extended fiber. **b, c,** photographs of a $8-\text{cm}-$ long preform and of several meters of fiber, respectively.

optical fiber draw tower consisting of a three-zone furnace was used. The preform was heated to its processing temperature (mid-zone set to $\sim 260\,^{\circ}\mathrm{C}$) as it was controllably inserted into the furnace. A motorized capstan pulled the resulting fiber from the viscous preform. A typical preform was 160 mm in length and 20 mm in diameter and was drawn into twenty meters of fiber. The drawing parameters were fixed to keep a constant draw-down ratio of about 20 between the features sizes of the initial preform and final fiber.

Crystalline selenium ($c - Se$) nanowires are attained by a post-drawing annealing process. Immediately after thermal drawing the selenium nanowires are rapidly cooled and quenched into the amorphous state. The nanowires may however be easily converted to the equilibrium crystalline state by annealing at $150\,^{\circ}\mathrm{C}$ for one hour (sketch in figure 5-3a). This temperature is substantially below the glass transition of the polymer cladding (polysulfone, $T_g \sim 190\,^{\circ}\mathrm{C}$), and the polymer is therefore unaffected by the annealing. The transition from amorphous to crystalline can be readily discerned visually. Figure 5-3 b (top panel) presents optical micrographs of a nanowire-embedded fiber section having the brick-red color characteristic of an amorphous selenium film. Upon annealing, the nanowire color changes into a dull gray (bottom panel of figure 5-3). Nanowires crystallization may also be induced optically (sketch in figure 5-3c). As a demonstration, sections of the same fiber were illuminated for two hours with an above-bandgap $532 - \mathrm{nm}$ laser (selenium bandgap $\sim 1.6\,\mathrm{eV}$)[51]. The laser power density was kept below $10\,\mathrm{mW/cm^2}$ in order to minimize heating effects [53]. An optical micrograph of a four-period structure of alternating amorphous (brick-red color) and crystalline (gray color) domains fabricated in this way is shown in figure 5-3d. The ability to change the beam size and location suggests that laser-induced crystallization could offer several advantages over thermally activated devitrification and should enable the fabrication of novel amorphous and crystalline heterostructures.

The atomic rearrangements, from amorphous to crystalline state, result in the change of electric energy band structure. The reflection spectra was performed for the in-fiber Se nanofilament arrays in an amorphous state before annealing and crystalline

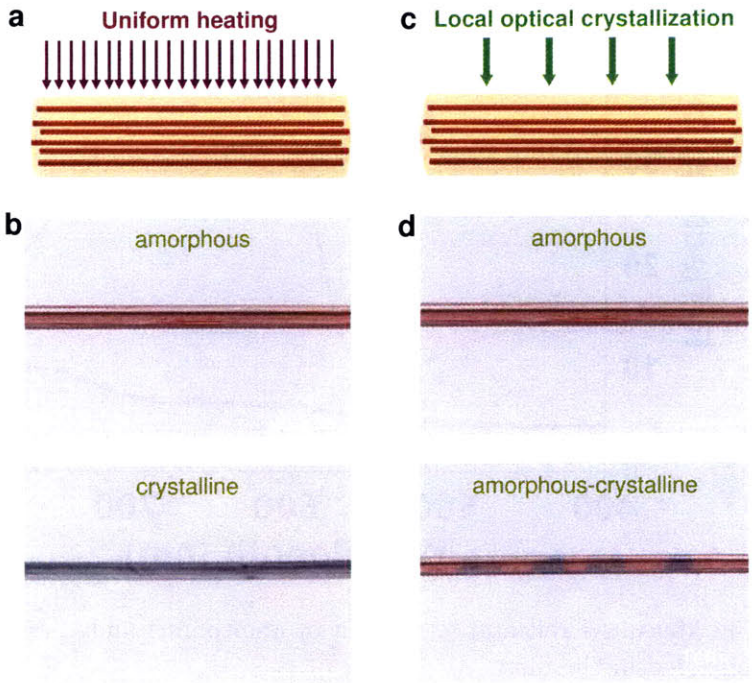

Figure 5-3: Thermal and optical crystallization of fiber-embedded selenium filaments. **a,** Schematic diagram of thermal annealing, and **b,** photographs highlighting the visible change from brick red (amorphous filaments, upper photograph) to grey(crystalline filaments, lower photograph) corresponding to the amorphous/crystalline transition brought about by annealing. **c,** Schematic diagram of laser-induced local crystallization and **d,** photographs of a fiber with alternating amorphous (brick-red) and crystalline (gray) regions along the fiber axis. Scale bar in all of the photographs is 1 cm.

state after annealing. figure 5-4 shows the measured reflectivity spectra in the visible range. The reflection peak at wavelength around 650 nm of amorphous filaments corresponds to its brick-red color; for the crystalline filaments, the light is absorbed with little reflection, resulting in gray color.

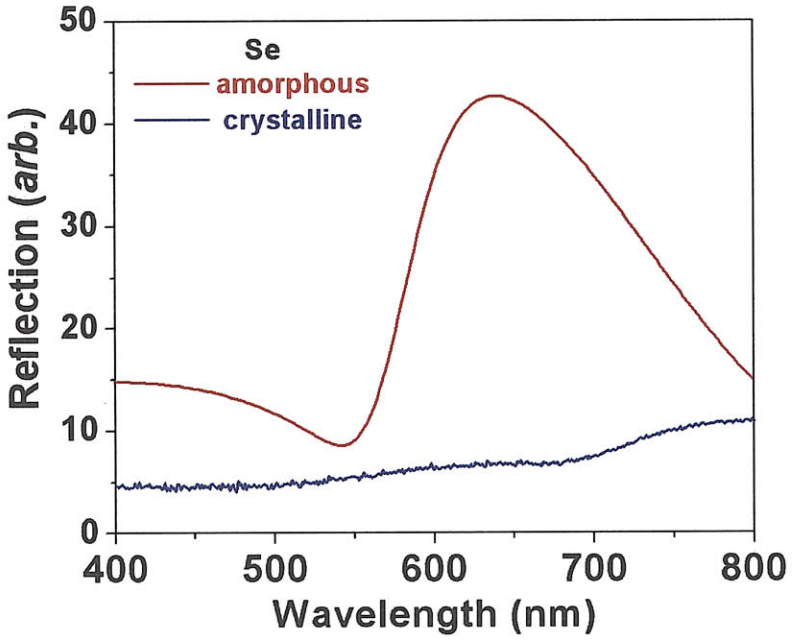

Figure 5-4: Measured reflectance spectra of amorphous and crystalline Se filament arrays embedded in the fiber.

5.4 Structure characterization

After presenting macroscopic-scale evidence for amorphous/crystalline phase transitions in the ensemble of fiber-encased filaments both thermally and optically, we proceed to demonstrate this phase transition at the single-filament level. This allows us, in particular, to quantitatively determine the extent of crystallization that the filaments undergo. The transition between the amorphous and crystalline phase was confirmed by transmission electron microscopy (TEM). A SEM micrograph (figure 5-6a left) shows a fiber cross-section with an array of nanowires arising from the breakup of $2-\mu\text{m}-$ thick film after its thickness was reduced to 100 nm through

drawing. Figure 5-6b (left) shows a magnification of individual nanowires in figure 5-6a (left).TEM samples of fiber cross-sections were prepared with a MT-X ultramicrotome equipped with a diamond knife. TEM measurements were performed on a JEOL-200CX TEM operated at 200KV. A TEM cross-section of an individual Se segment prior to annealing is shown in figure 5-6a (middle). Due to volume conservation, the maximum thickness of ellipsoidal cross-section is about 200 nm, instead of the expected 100 nm for a continuous film. A TEM diffraction pattern shows only diffuse halos indicative of an amorphous material (figure 5-6a right). After annealing, multiple grain boundaries are seen in the TEM image (figure 5-6b middle), and the electron diffraction pattern shows satellite spots in concentric rings (figure 5-6b right) indicating poly-crystallinity.

The composition of nanofilaments is further analyzed by energy dispersive X-ray spectra, as shown in figure 5-5. The measurement was performed at a selected area around of fiber cross section, where filament is located. The peak intensity confirms the Se component. Other composition signal of oxygen, carbon and sulfur may come from the cladding polymer PSU.

In light of the typical grain sizes observed in the annealed filaments, it is expected that nearly single crystal nanowires are expected when the nanowire size decreases below the average selenium grain size. To verify this, a preform containing a $200-\text{nm}-$ thick selenium film was drawn into fiber with the intention of reducing the film thickness to 10 nm. The SEM and TEM micrographs in figure 5-6c (left) and (middle), respectively, show the film has completely broken up into nanowires having circular cross-sections and an average spacing between filaments (i.e., the instability wavelength, λ) of approximately $3\,\mu$m. A diffraction pattern taken from one of these nanowires (figure 5-6c right) demonstrates the single-crystalline nature of the nanowire sample. This provides direct evidence that single-crystalline semiconductor structures with feature sizes of 100 nm or less can be fabricated by optical-fiber thermal drawing. The longitudinal spatial extent of the single-crystalline domains is currently under investigation.

We now proceed to provide an order-of-magnitude estimate of the obtained fila-

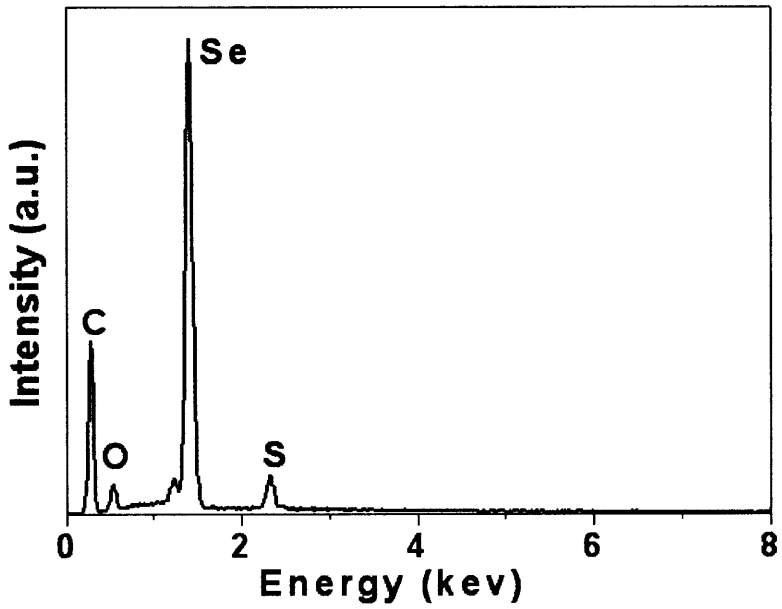

Figure 5-5: Energy dispersive X-ray spectra of nanowire cross-section at a selected region.

ment diameters. The initial film thickness in the preform was 200 nm, after drawing down and breakup initiation the resulting filament diameter in the fiber is determined by conservation of volume. The area of the actual filament cross section can be equated to the initial thickness of the film divided by the draw-down ratio (which in the absence of break-up would be the film thickness in the fiber) times the distance between filaments λ,

$$\pi D^2 \sim \lambda(h/z), \tag{5.1}$$

where D is the filament diameter, h is the initial semiconductor layer thickness, z is the preform-to-fiber draw-down ratio, and is the instability wavelength. As h/z $\sim$ 200/20 nm and $\lambda \sim 3\,\mu$m, the filament diameter is approximately 200 nm, close to the actual filament size (figure 5-6c middle). The ultimate filament diameter is determined by initial film thickness, the film viscosity, surface tension and draw-down ratio. These parameters were studied in the previous Chapter 4, and amorphous As_2Se_3 filaments were drawn to thicknesses down to 20 nanometers.

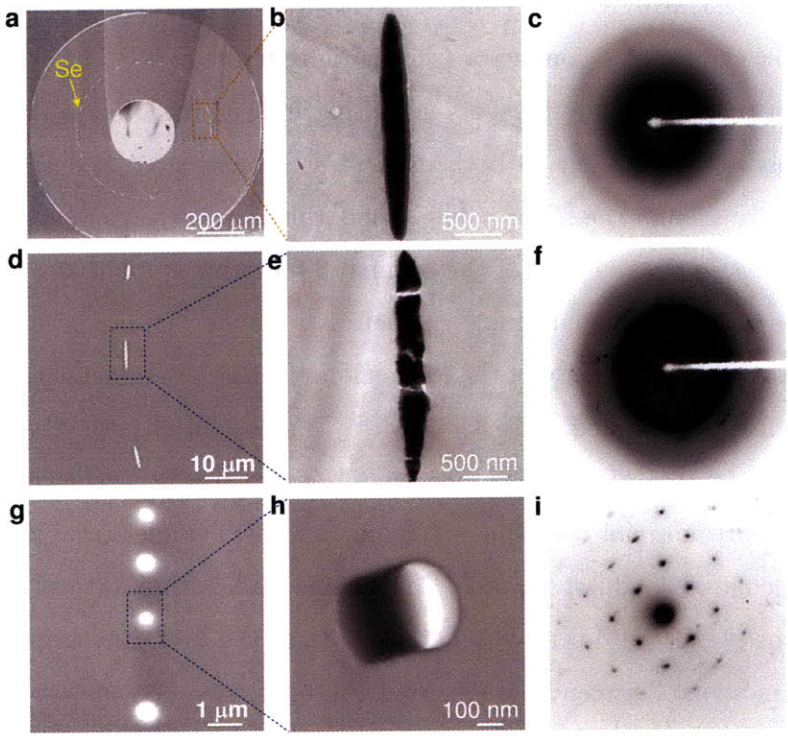

Figure 5-6: Filament characterization. **a,** Amorphous filament arrays. Left, an SEM micrograph of a fiber cross-section containing a filament array; middle, TEM micrographs and, right, corresponding electron diffraction patterns of $a-Se$ filaments resulting from an initial $2-\mu m-$ thick continuous amorphous film. **b,** Polycrystalline filament arrays. Left, a magnified SEM micrograph of ellipsoidal filaments; middle, TEM micrograph and, right, electron diffraction pattern demonstrating polycrystallinity. **c,** Crystalline filament array. Left, a magnified SEM micrograph of a filament array resulting from the complete break up of a continuous amorphous film having an initial $200-nm$ thickness; middle, TEM micrograph and, right, single crystal electron diffraction pattern.

5.5 Electrical and optoelectric property

Lastly, we demonstrate an in-fiber, crystalline-filament device in the form of a photodetector or optical switch. In contrast to many other nanowire arrays, the entire fiber filament array can be easily connected to external circuitry by contacting the two fiber ends with a conductor (schematic in figure 5-7a). For example, an in-fiber array of polycrystalline filaments (resulting from thermal annealing) was contacted by applying silver paint to both ends of a fiber segment and then wrapping thin metal wire around the silver-painted ends (figure 5-7b). A number of 2-cm-long filament arrays were cut out of the original 20-meter-long fiber and measured. These sections displayed similar ohmic characteristics under applied bias (figure 5-7c), and the electrical conductivity of the filaments in the dark can be estimated from the applied voltage, measured current, and array dimensions (length of wires $\sim 2\,\mathrm{cm}$; total cross-section area of wire is approximately equal to the product of the layer thickness had breakup not occurred $\sim 100\,\mathrm{nm}$, and its circumferential length $\sim 1000\,\mu\mathrm{m}$). The calculated conductivity of $10^{-8}\,\Omega^{-1}\cdot\mathrm{cm}^{-1}$ is less than that of bulk single crystal selenium ($\sim 10^{-6}\,\Omega^{-1}\cdot\mathrm{cm}^{-1}$)[54]. As noted in the literature, significant disparities in conductivity between filaments and the bulk have been observed previously and have been attributed to enhanced inelastic scattering of carriers at surfaces due to increased surface-to-volume ratios, reflection of electrons at grain boundaries, and defects or impurities along the high aspect ratio wires [55]. An array of amorphous filaments was contacted and measured in the same way (gray line in figure 5-7c) but no current was recorded owing to its extremely low conductivity ($< 10^{-16}\Omega^{-1}\mathrm{cm}^{-1}$) [56], [57]. The measurable current of the $c-Se$ filament arrays confirms that there is a continuous path between fiber ends and that the selenium filaments are at least 2 cm in length.

The filament arrays exhibit enhanced photoconductivity under illumination from a $500\,\mathrm{mW/cm}^2$ broadband white-light source (red line in figure 5-7c). A repeatable two-orders-of-magnitude change in current is demonstrated by turning the illumination on and off under fixed applied bias (figure 5-7d). The observed fluctuation of dark

current may be due to thermal and generation-recombination noise [41]. The large difference in light and dark conductivity suggests possible use as an optical switch [58]. Unlike other nanowire devices [59], the photoconductivity of the filament arrays is unaffected by changes in the local environment due to contamination or humidity, as they are clad in the protective polymer matrix.

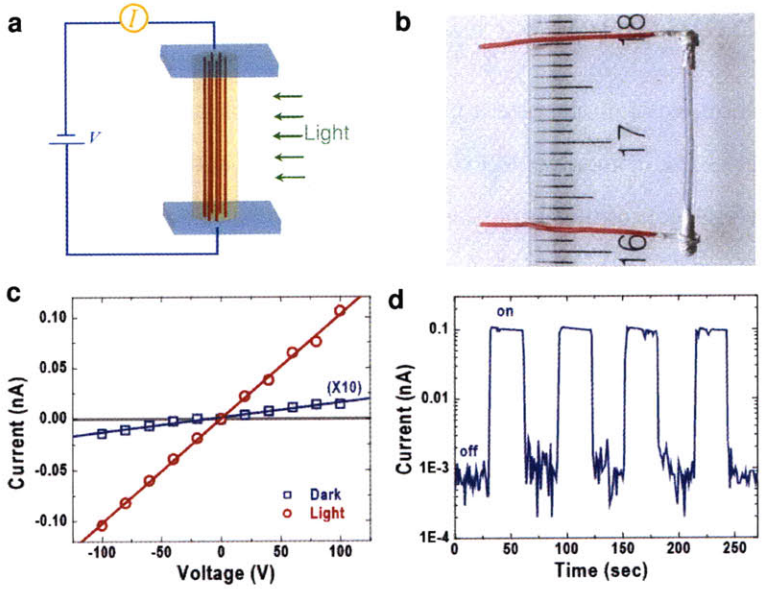

Figure 5-7: Electrical connection and optoelectronic properties of centimeter-long c-Se nanowires. **a, b,** Sketch and photograph of electrical contact to an external circuit by connecting the fiber ends. **c,** Current-voltage characteristics of an array of $2-\mathrm{cm}-\mathrm{longc}-\mathrm{Se}$ nanowires in the dark (blue line) and under illumination (red line). No detectable current was observed in the a-Se nanowires (gray line), owing to their large resistivity. **d,** Reversible switching between high and low current states as illumination is modulated.

The simplicity of electrical contact to the nanowire arrays is a direct result of the fabrication method. The nanowires themselves are generated in a unidirectional process, imparting a completely uniform global orientation. The drawing process does not impose any intrinsic limitation on the length of the nanowires that can be fabricated. Indeed, in the absence of fabrication defects there is no reason to believe that the nanowires do not extend the entire length of drawn fiber, typically upwards of twenty meters. Finally, the polymer matrix surrounding the semiconductor forms a protective and mechanically tough sheath that enables simple and

macroscopic manipulation to be done in a straightforward fashion without expensive nano-manipulation techniques, circumventing a major challenge to the large-scale integration of nanowire devices. Electrical contact to the nanowire arrays is made trivial by directly connecting fiber ends.

5.6 Summary

In conclusion,we demonstrate a new technique to fabricate, manipulate and electronically address one-dimensional crystalline semiconductor nanowire arrays. The optical fiber drawing technique enables very long lengths of continuous and aligned nanowires to be generated in a straightforward fashion. The capacity to build amorphous-crystalline heterostructure nanowires by local crystallization may provide a powerful tool to create new electronic junctions as well as optical modulation by refractive index contrast. Moreover, the process of laser-induced local crystallization is similar to the read/write process in phase-change materials [60], and the nanowires themselves may become a novel data storage platform.

Chapter 6

Stability of continuous filaments

6.1 Introduction

In chapter 3, we have presented that cylindrical shell thickness down to submicrometers is attainable in microstructured fibers by the conventional thermal drawing. If thickness is further reduced, cylindrical shell undergoing a thermal drawing process evolves into an ordered array of filaments, as discussed in Chapter 4. The breakup only occurs un the azimuth direction, while axial direction remains intact. A nature theoretical question is how to understand these stability or instability of these nanostructures. This understanding will guide us to select material and control fabrication, in order to achieve the designed structures. We will mainly focus on these theoretical questions in this chapter and next chapter 7.

More specifically, we are interested in three questions as follows. First is the stability of cylindrical shell thickness. Uniform-thickness cylindrical shells (made of glass materials such as As_2Se_3 and As_2S_3), down to sub-micrometer or even nanometer thicknesses, have been successfully fabricated in glass materials, by a drawing process whereby a large-scale "preform" is heated and pulled into a long thread, as depicted in figure 6-1. Second is the azimuth instability if the shell thickness is further reduced towards the nanoscale. A thin cylindrical shell (made of the glass material selenium, Se), is observed to break up into an ordered array of filaments; that is, the breakup of the cylindrical shell occurs along the azimuthal direction [42, 49]. Third, the stability

of continuous filaments. When the thin film breaks into filaments arrays, the axial continuity of filament arrays remains intact. In general, one would like to understand the fundamental mechanism for the observed azimuthal break-up process, and more generally what instability mechanisms limit the attainable feature size in drawn fibers.

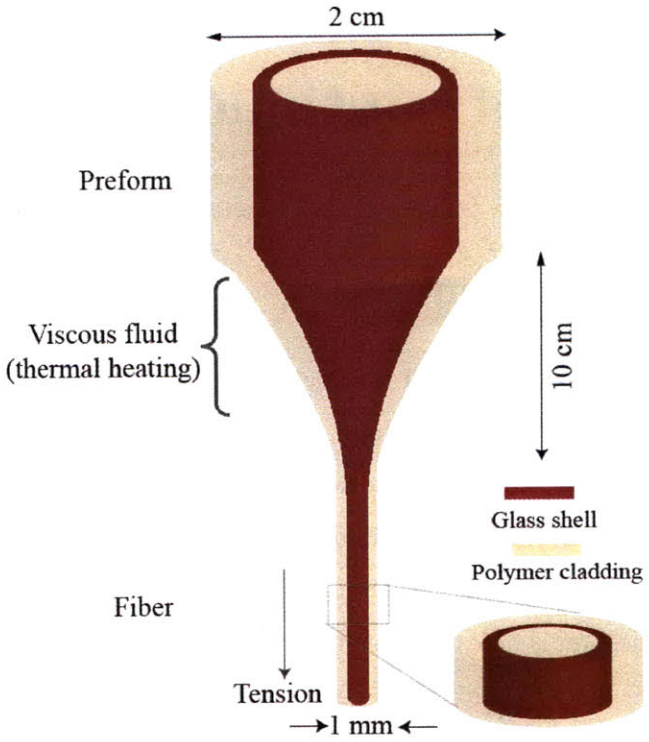

Figure 6-1: Optical-fiber thermal drawing. Preform is heated at elevated temperature into viscous fluid, and stretched into extended fibers by applied tension. This preform is specially designed with a thin cylindrical shell in polymer matrix.

In this chapter, we first present the feature size in microstructured fibers, and then provide a general physical picture of thermal drawings by dimensionless number analysis. Next, we focus on one perspective of fluid instabilities, *i.e.*, capillary instability and its application to continuous filaments. In following chapter, we will explore the capillary instability of concentric cylindrical shell by numerical simulations and its application of stability of shell in our microstructured fibers.

6.2 Feature size in composite microstructured fibers

Most optical fibers are mainly made of a single material, silica glass. Recent work, however, has generalized optical fiber manufacturing to include microstructured fibers that combine multiple distinct materials including metals, semiconductors, and insulators, which expand fiber-device functionalities while retaining the simplicity of the thermal-drawing fabrication approach [77]. For example, a periodic cylindrical-shell multilayer structure has been incorporated into a fiber to guide light in a hollow core with significantly reduced loss for laser surgery [82].

Uniform layer thicknesses, down to micrometers or even to nanometers, have been successfully achieved in fibers by this method. Mechanically flexible fibers with a uniform diameter have been produced, as shown in figure 6-2(a). Figure 6-2(b) shows a typical Scanning Electron Microscope (SEM) micrograph of a cross-section with 1 mm fiber diameter. Magnified SEM micrographs in figure 6-2(c) and (d), for two different fibers, reveal high-quality multiple-layer structures with thicknesses on the order of micrometers and tens of nanometers, respectively.

Ideally, the cross-section of the resulting fibers retains the same structure and relative sizes of the components as in the preform. If the layer thickness becomes too small, however, we observed the layers to break up azimuthally, as shown in the cross-section of figure 6-2(e), while continuity along the axial direction remains intact. In this fashion, a thin cylindrical shell breaks into filament arrays embedded in a fiber [42]. After dissolving the polymer cladding, the resulting separated glass filaments are shown in figure 6-2(f) [42].

6.3 Dimensionless groups during thermal drawing process

Thermal drawing is a complicated physical system, involving the coupled thermal, mechanical and fluid mechanical problems. To identify the operating regime of the fiber drawing process, we consider the relevant dimensionless numbers. The Reynolds

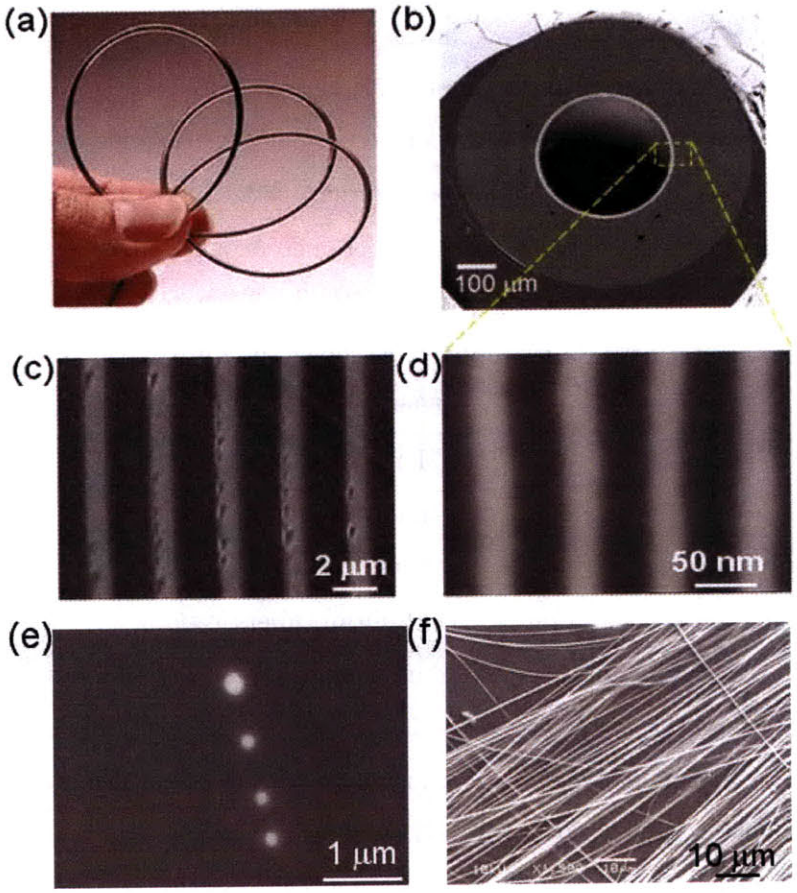

Figure 6-2: SEM micrographs of cylindrical shells in fiber. **(a)** Photograph of fiber. **(b)** SEM of fiber cross-section. Magnified view of multilayer structures reveals the thickness of micrometer **(c)** and tens of nanometers **(d)**, respectively. Bright and dark color for glass and polymer in SEM, respectively. **(e)** showing layer breakup into circles in the fiber cross-section, while **(f)** presenting the continuous filaments obtained from fiber after dissolving polymer matrix.

number (Re), Froude number (Fr), and capillary number (Ca) are:

$$\text{Re}=\frac{\rho U h}{\eta},\ \text{Fr}=\frac{U^2}{gh},\ \text{Ca}=\frac{\eta U}{\gamma}, \tag{6.1}$$

where $\rho \approx 10^3$ kg/m^3 is the density of the materials, $g \approx 10$ m/s^2 is gravity, $U \approx 5$ mm/s is drawing speed, $\eta \approx 10^5$ Pa $\cdot$ s is viscosity, $h \approx 100$ nm is the layer thickness, and $\gamma = 0.1$ N/m is surface tension between polymer and glass [84, 85]. Therefore, these dimensionless numbers in a typical fiber draw are Re $\approx 10^{-10}$, Fr $\approx 10^2$ and Ca $\approx 10^4$. Small Re number, large Fr number, and large Ca number imply a weak inertia term, negligible gravity, and dominant viscosity effects, respectively. In addition, since the fiber diameter is $D \approx 1$ mm and the length of the neck-down region is $L \approx 10$ cm, the ratio $D/L \approx 1/100$ is much less than 1, and thus the complicated profile of neck-down cone is simplified into a cylindrical shape for the purpose of easier analysis.

6.4 Capillary instability

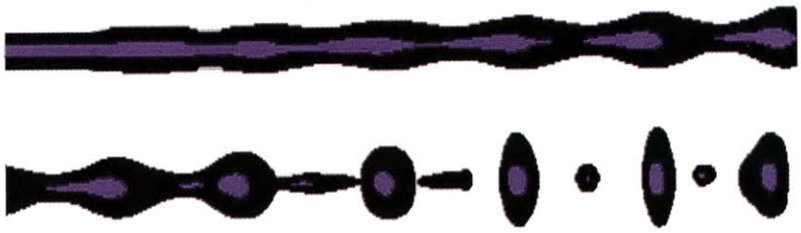

Figure 6-3: Sketch of capillary instability. Small amplitudes of perturbation in the cylindrical fluid are amplified, resulting in breakup into a serials of droplets.

The classical capillary instability, the break-up of a cylindrical liquid thread into a series of droplets, is perhaps one of the most ubiquitous fluid instabilities, as depicted in figure 6-3. It appears in a host of daily phenomena [61, 62] from glass-wine tearing [63], and faucet dripping to ink-jet printing. The study of capillary instability has a long history. In 1849, Plateau attributed the mechanism to surface tension:

the breakup process reduces the surface energy [64]. Lord Rayleigh pioneered the application of linear stability analysis to quantitatively characterize the growth rate at the onset of instability, and found that a small disturbance is magnified exponentially with time [65]. Subsequently, Tomotika investigated the effect of viscosity of the surrounding fluid, showing that it acts as a deterrent to slow down the instability growth rate [66]. Stone and Brenner investigated instabilities in a two-fluid cylindrical shell geometry with equal viscosities [67]. Many additional phenomena have been investigated, such as the cascade structure in a drop falling from a faucet [68], steady capillary jets of sub-micrometer diameters [69], and double-cone neck shapes in nanojets [70]. Capillary instability also offers a means of controlling and synthesizing diverse morphological configurations. Examples include: a long chain of nanospheres generated from tens-of-nanometer diameter wires at the melt state [71, 72]; polymer nanorods formed by annealing polymer nanotubes above the glass transition point [73]; and nanoparticle chains encapsulated in nanotubes generated by reduction of nanowires at a sufficiently high temperature [74]. Moreover, instabilities of fluid jets have numerous chemical and biological applications [75, 76].

6.4.1 Rayleigh linear theory

Original work of cylinder instability dated back to Rayleigh's work in 1878 [65]. Using perturbation analysis,he derived the a critical wavelength scale (λ_{crit}), above which instability develops resulting in the amplification of initial small amplitude.

Considering a radically symmetric perturbation on a uniform cylinder of radius R_0

$$R(z,t) = R_{cyl} + \epsilon(t)cos(\frac{2\pi z}{\lambda}), \tag{6.2}$$

where $\epsilon(t)$ is time-dependent perturbation amplitude. Volume conservation gives

$$\pi R_0^2 \lambda = \int_0^\lambda \pi R^2(z,t)dz = \pi R_{cyl}^2 \lambda + \frac{\pi\lambda\epsilon^2(t)}{2}, \tag{6.3}$$

The average cylinder radius will shrink with times as following

$$R_{cyl} = R_0 - \frac{\epsilon^2(t)}{4R_0} + ..., \tag{6.4}$$

Total surface energy is:

$$E^{surf} = \int_0^\lambda \gamma dA = \gamma \int_0^\lambda 2\pi R ds = 2\pi\gamma \int_0^\lambda R\sqrt{1+(\frac{dR}{dz})^2}dz = E_0^{surf} + \frac{\pi\gamma}{2\lambda R_0}[(2\pi R_0)^2 - \lambda^2]\epsilon^2(t). \tag{6.5}$$

Thus, the energy decreases with time if the *Rayleigh instability condition* is satisfied,

$$\lambda > \lambda_{crit} = 2\pi R_0, \tag{6.6}$$

Perturbation with a wavelength above the critical wavelength scale is amplified with time to reduce surface energy.

6.4.2 Tomotika linear theory

Consider a cylinder of viscous fluid surrounded by a second fluid that is assumed infinite in extent. The fluid inside the cylinder has viscosity η_{in}, while the outside fluid has viscosity η_{out}. The fluids are assumed incompressible, Newtonian, and isotropic. There is an interfacial energy between the two fluids γ. The cylinder has a local radius r, and initially the radius has everywhere a nominally uniform value, a. However, instabilities of a defined initial size exist in the cylinder radius; these instabilities are described spatially by the expression $e^{i\kappa z}$ and they grow in time according to the expression e^{qt}. The system is assumed axi-symmetric, so theta-dependent terms may be ignored. This framework is depicted schematically in figure 6-4.

Cylinder geometry and current function For incompressible viscous fluid of viscosity η and of density ρ for the case in which the motion is symmetrical about the axis z, the equations for velocity (u, v, w) in (r, θ, z) are:

$$\frac{\partial u}{\partial t} + u\frac{\partial u}{\partial r} + w\frac{\partial u}{\partial z} = -\frac{1}{\rho}\frac{\partial p}{\partial r} + \frac{\eta}{\rho}(\frac{\partial^2 u}{\partial r^2} + \frac{1}{r}\frac{\partial u}{\partial r} - \frac{u}{r^2} + \frac{\partial^2 u}{\partial z^2}), \tag{6.7}$$

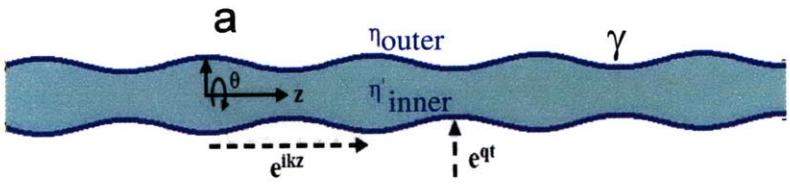

Figure 6-4: Coordinate system and basic model geometry used to describe capillary breakup in a system comprised of two viscous fluids.

$$\frac{\partial w}{\partial t} + u\frac{\partial w}{\partial r} + w\frac{\partial w}{\partial z} = -\frac{1}{\rho}\frac{\partial p}{\partial z} + \frac{\eta}{\rho}(\frac{\partial^2 w}{\partial r^2} + \frac{1}{r}\frac{\partial w}{\partial r} + \frac{\partial^2 w}{\partial z^2}), \tag{6.8}$$

And the continuity equation, stemming from mass conservation, is:

$$\frac{\partial u}{\partial r} + \frac{u}{r} + \frac{\partial w}{\partial z} = 0, \tag{6.9}$$

Now induce the Stokes current function Ψ, by which the above continuity equation is satisfied,

$$u = \frac{1}{r}\frac{\partial \Psi}{\partial z}, w = -\frac{1}{r}\frac{\partial \Psi}{\partial r}, \tag{6.10}$$

This is analogous to the magnetic potential A, and magnetic field B is the curl of A. Eliminating pressure p in the motion equation, we obtain the following:

$$(\frac{\partial}{\partial t} + \frac{1}{r}\frac{\partial \Psi}{\partial z}\frac{\partial}{\partial r} - \frac{1}{r}\frac{\partial \Psi}{\partial r}\frac{\partial}{\partial z} - \frac{2}{r^2}\frac{\partial \Psi}{\partial z})D\Psi = \frac{\eta}{\rho}DD\Psi,$$

where D denotes a differential operator:

$$D = \frac{\partial^2}{\partial r^2} - \frac{1}{r}\frac{\partial}{\partial r} + \frac{\partial^2}{\partial z^2},$$

Low-velocity approximation With an assumption of slow motions, the squares and products of velocity components may be neglected, nonlinear effect has been ignored by linear approximation theory, and equation is reduced to a simpler form,

$$(D - \frac{\rho}{\eta}\frac{\partial}{\partial t})D\Psi = 0,$$

Since above operators are commutative, function Ψ is separated into two parts, Ψ_1 and Ψ_2,

$$D\Psi_1 = 0, D\Psi_2 - \frac{\rho}{\eta}\frac{\partial \Psi_2}{\partial t} = 0,$$

Separation of time and space Now assume the motions are proportional to exp(iωt) and exp(ikz),

$$\Psi_1(r,z,t) = \Phi_1(r)exp(i(\omega t + kz)), \Psi_2(r,z,t) = \Phi_2(r)exp(i(\omega t + kz)),$$

Then equations for Φ_1 and Φ_1 become,

$$\frac{d^2\Phi_1}{dr^2} - \frac{1}{r}\frac{d\Phi_1}{dr} - k^2\Phi_1 = 0, \frac{d^2\Phi_2}{dr^2} - \frac{1}{r}\frac{d\Phi_2}{dr} - k_1^2\Phi_1 = 0,$$

where $k_1^2 = k^2 + i\omega\rho/\eta$, k_1 is complex value generally.

General solution The general solution of radius function is:

$$\Phi_1 = A_1 r I_1(kr) + B_1 r K_1(kr), \Phi_2 = A_2 r I_1(k_1 r) + B_2 r k_1(k_1 r),$$

So the general solutions of NS equations become

$$\Psi = \Psi_1 + \Psi_2 = ([A_1 r I_1(kr) + B_1 r K_1(kr)] + [A_2 r I_1(k_1 r) + B_2 r I_1(k_1 r)])exp(i(\omega t + kz)), \tag{6.11}$$

Solution of inner fluid is:

$$\Psi_{inner} = \Psi_{i1} + \Psi_{i2} = (A_1 r I_1(kr) + A_2 r I_1(k_1 r))exp(i(\omega t + kz)), \tag{6.12}$$

Solution of outer fluid is:

$$\Psi_{outer} = \Psi_{o1} + \Psi_{o2} = (B_1 r K_1(kr) + B_2 r K_1(k_1 r))exp(i(\omega t + kz)), \tag{6.13}$$

Here K_n and I_n are the n^{th}-order modified Bessel functions of the first and second kind, respectively. The general solutions for both regions contain both the $I_1(kr)$

and $K_1(kr)$ Bessel functions, but $K_1(kr)$ is eliminated from the interior solution and $I_1(kr)$ is eliminated from the exterior solution by the boundary conditions because these functions grow infinitely towards $r = 0$ or $r = \infty$, respectively. A1, B1, A2, and B2 are constant coefficients.

Boundary conditions The following boundary conditions at interface remain to be applied:

1. No slipping for velocity at the interface(velocity along r and z direction). The velocity components should be continuous at the surface.

$$(u^{inner})_{r=a} = (u^{outer})_{r=a}, (w^{inner})_{r=a} = (w^{outer})_{r=a},$$

2. Continuous tangential stress. Tangential stress parallel to the surface is continuous at the surface of the column.

$$\eta_{inner}(\frac{\partial u_{inner}}{\partial z} + \frac{\partial w_{inner}}{\partial r}) = \eta_{outer}(\frac{\partial u_{outer}}{\partial z} + \frac{\partial w_{outer}}{\partial r}),$$

3. Normal stress from surface tension. The difference in the normal stress between inner and outer fluid is due to the interfacial surface tension.

$$(P_{rr}^{outer})_{r=a} - (P_{rr}^{inner})_{r=a} = F_{surface},$$

The displacement in the r-direction of a fluid element on the interface is

$$\xi = \int (u^{inner})_{r=a} dt = \int (\frac{1}{a}\frac{\partial \Psi^{inner}}{\partial z})_{r=a} dt = \frac{k}{\omega a}(\Psi^{inner})_{r=a},$$

The pressure difference due to the interfacial surface tension γ, which is assumed to be constant, is given by

$$F_{surface} = \frac{\gamma \xi (k^2 a^2 - 1)}{a^2}. \tag{6.14}$$

Growth rate The two stream function solutions and these three remaining boundary conditions result in four equations that can be expressed in the following deter-

minantal form (where K_n' and I_n' denote derivatives):

$$\begin{vmatrix} I_1(ka) & kaI_1'(ka) & K_1(ka) & kaK_1'(ka) \\ I_0(ka) & I_0(ka)+kaI_1(ka) & -K_0(ka) & -K_0(ka)+kaK_1(ka) \\ (\eta_{inner}/\eta_{outer})I_1(ka) & (\eta_{inner}/\eta_{outer})kaI_0(ka) & K_1(ka) & -kaK_0(ka) \\ G_1 & G_2 & K_1'(ka) & G_4 \end{vmatrix} = 0,$$

where

$$G_1 = \frac{\eta_{inner}}{\eta_{outer}} I'(ka) + \frac{\gamma(k^2a^2-1)}{2qa^2\eta} I_1(ka),$$

and

$$G_2 = \frac{\eta_{inner}}{\eta_{outer}} [I'(ka) + kaI_1''(ka) - K_0(ka)] + \frac{\gamma(k^2a^2-1)}{2qa\eta} I_1'(ka),$$

and

$$G_4 = K_1'(ka) + kaK_1''(ka) + K_0(ka),$$

Another critical assumption has been employed, which is that the effects of inertia can be neglected compared to the effects of viscosity (viscosity dominates the system), so the solution is found in the limit of vanishingly small densities, and the term k_1 is removed.

Finally, by expanding the determinant in the fourth row and rearranging the result, we can obtain our sought-after solution for the value of *growth rate* q as a function of η_{outer}, η_{inner}, γ, and ka:

$$q = i\omega = \frac{\gamma}{2a\eta_{outer}} \Phi(ka, \eta_{inner}/\eta_{outer}), \tag{6.15}$$

Here Φ, a complicated growth factor, is defined as follows,

$$\Phi(ka, \eta_{inner}/\eta_{outer}) = (1-(ka)^2) \frac{N(ka)}{M(ka, \eta_{inner}/\eta_{outer})}, \tag{6.16}$$

where

$$N(ka) = I_1(ka)\Delta_1 - [kaI_0(ka) - I_1(ka)]\Delta_2, \tag{6.17}$$

and

$$M(ka, \eta_{inner}/\eta_{outer}) = (\frac{\eta_{inner}}{\eta_{outer}})[kaI_0(ka) - I_1(ka)]\Delta_1 - (\frac{\eta_{inner}}{\eta_{outer}})[(k^2a^2+1)I_1(ka) - kaI_0(ka)]\Delta_2$$
$$-(kaK_0(ka) + K_1(ka))\Delta_3 - [(k^2a^2+1)K_1(ka) + kaK_0(ka)]\Delta_4.$$

Here $\Delta_1, \Delta_2, \Delta_3$, and Δ_4 are each a 3×3 determinant derived from expansion of the previous 4×4 determinant as follows:

$$\Delta_1 = \begin{vmatrix} xI_0(x) - I_1(x) & K_1(x) & -xK_0(x) - K_1(x) \\ I_0(x) + xI_1(x) & -K_0(x) & -K_0(x) + xk_1(x) \\ (\eta_{inner}/\eta_{outer})xI_0(x) & K_1(x) & -xk_0(x) \end{vmatrix},$$

$$\Delta_2 = \begin{vmatrix} I_1(x) & K_1(x) & -xK_0(x) - K_1(x) \\ I_0(x) & -K_0(x) & -K_0(x) + xk_1(x) \\ (\eta_{inner}/\eta_{outer})I_1(x) & K_1(x) & -xk_0(x) \end{vmatrix},$$

$$\Delta_3 = \begin{vmatrix} I_1(x) & xI_0(x) - I_1(x) & -xK_0(x) - K_1(x) \\ I_0(x) & I_0(x) + xI_1(x) & -K_0(x) + xK_1(x) \\ (\eta_{inner}/\eta_{outer})I_1(x) & (\eta_{inner}/\eta_{outer})xI_0(x) & -xK_0(x) \end{vmatrix},$$

$$\Delta_4 = \begin{vmatrix} I_1(x) & xI_0(x) - I_1(x) & K_1(x) \\ I_0(x) & I_0(x) + xI_1(x) & -K_0(x) \\ (\eta_{inner}/\eta_{outer})I_1(x) & (\eta_{inner}/\eta_{outer})xI_0(x) & K_1(x) \end{vmatrix}.$$

6.5 Calculated instability growth factor

Linear theory has shown that the growth rate in Eq. 6.15 is a complicated function of instability wavelength and inner and outer viscosities. To better understand this growth rate, we performed numerical calculations in Matlab to quantitatively investi-

gate both wavelength and viscosities. This will provide us insight of viscous materials that are identified in our microstructured fibers.

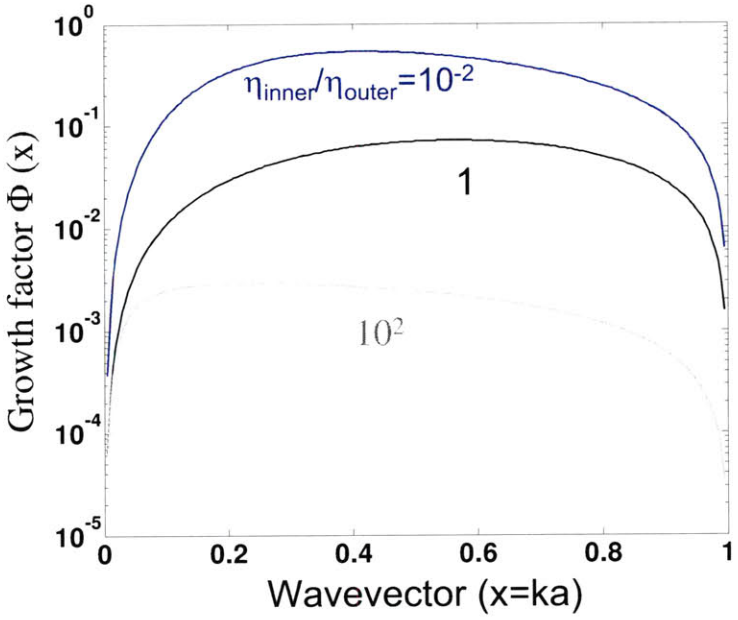

Figure 6-5: Growth rate factor as a function of wavelength for various viscosity contrast $\eta_{inner}/\eta_{outer}$.

Figure 6-5 shows the growth factor $\Phi(x)$ as a function of wavevector ($x = ka$) for different viscosity contrasts of $\eta_{inner}/\eta_{outer}$. As wavelength is shorter than critical wavelength ($x > 1$), instability can not develop and small perturbations are damped away by viscosity. However, as wavelength becomes longer ($x < 1$), growth factor is greater than $phi > 0$, which means that small perturbations are amplified. At certain wavelength, the growth rate reaches to a maximum value. If wavelength is too long ($x \rightarrow 0$), the growth factor decreases.

Furthermore, the maximum value of Φ_{max} at a certain wavelength (x^*) dependents on the viscosity contrast $\eta_{inner}/\eta_{outer}$. Figure 6-6 shows that Φ_{max} decreases with viscosity contrast $\eta_{inner}/\eta_{outer}$, and wavelength ($x^*$) gradually deceases as $\eta_{inner}/\eta_{outer}$ is away from 1.

During fiber drawing with a scale factor $s = 20$, the radius of filament is reduced by a factor of s ($\Delta r = s$) , while wavelength along the axial direction is extended

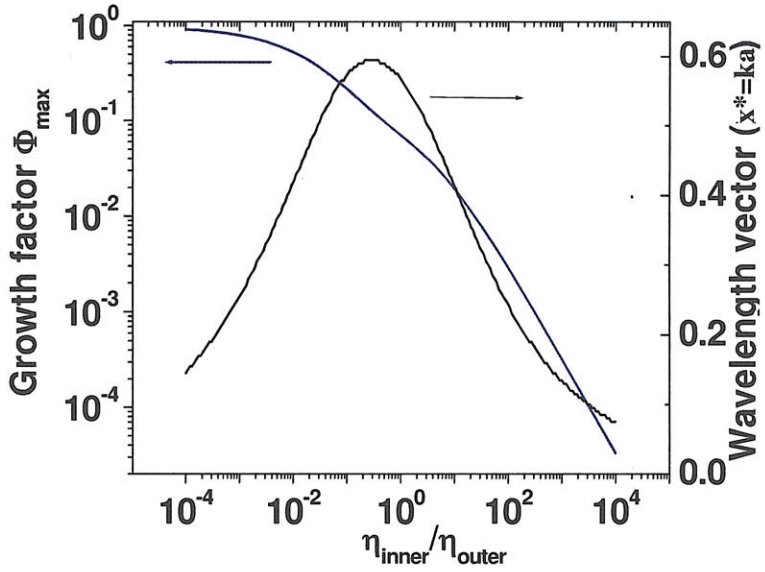

Figure 6-6: Maximum growth factor and the corresponding wavelength as a function of viscosity contrast.

by a factor of s^2 ($\Delta\lambda = s^2$). So the dimensionless wavelength changes by s^3 ($\Delta x = \Delta(r/\lambda) = s^3 = 10^4$), which corresponds to the change of growth factor ($\Psi = (1 - x^2)\Phi(x)$) with six orders of magnitude, as seen from figure 6-7 in a log-log scale.

6.6 Discussion of continuous filaments down to submicrometer scale

As shown in Fig. 6-2(e–f), in some cases the initial shell breaks up (azimuthally) into long cylindrical filaments. These filaments themselves should be subject to the classic capillary instability and in principle should eventually break up into droplets. In our fiber-drawing experiments, however, no further instability is observed: the filaments are observed to remain continuous and unbroken over at least cm length scales with diameters reaching submicrometer scales [42, 49]. Since a cylindrical filament of one fluid surrounded by another should be described exactly by the Tomotika model, it is important to know whether the observed stability is consistent with this model,

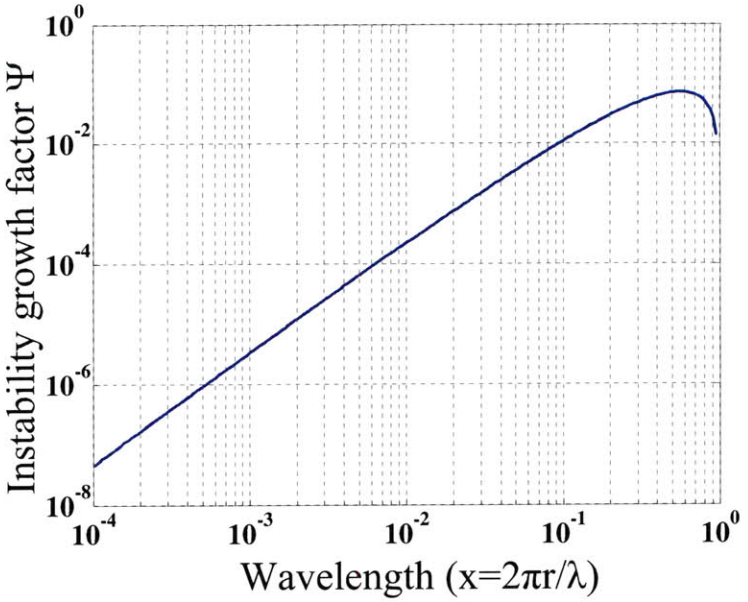

Figure 6-7: Instability growth factor as a function of wavelength on a log log scale.

or otherwise requires some additional physical mechanism (such as visco-elasticity) to explain. In this section, we find that the timescale of instability predicted by the Tomotika model exceeds the dwelling time of fiber drawing, making it unsurprising that filament instability is not observed. In fact, we show that the instability time scale exceeds the fiber drawing time even under unrealistically conservative assumptions: that the filaments appear immediately in the fiber drawing, that the maximum instability growth rate is cumulative even though the lengths scale achieving maximum growth changes with the filament radius during drawing, and that the polymer is always at its minimum value (corresponding to the highest temperature point).

An instability with time scale τ corresponds to exponential growth of a fluctuation amplitude ϵ according to $\frac{d\epsilon}{dt} = \epsilon/\tau$. If τ is time varying, then the total amplitude growth is $exp[\int dt/\tau(t)]$. Converting to $dz = v(z)dt$ for a position-dependent axial flow velocity $v(z)$ during thermal drawing, we therefore obtain a total exponential growth factor:

$$\Gamma = \int_0^L \frac{dz}{v(z)\tau(z)}, \tag{6.18}$$

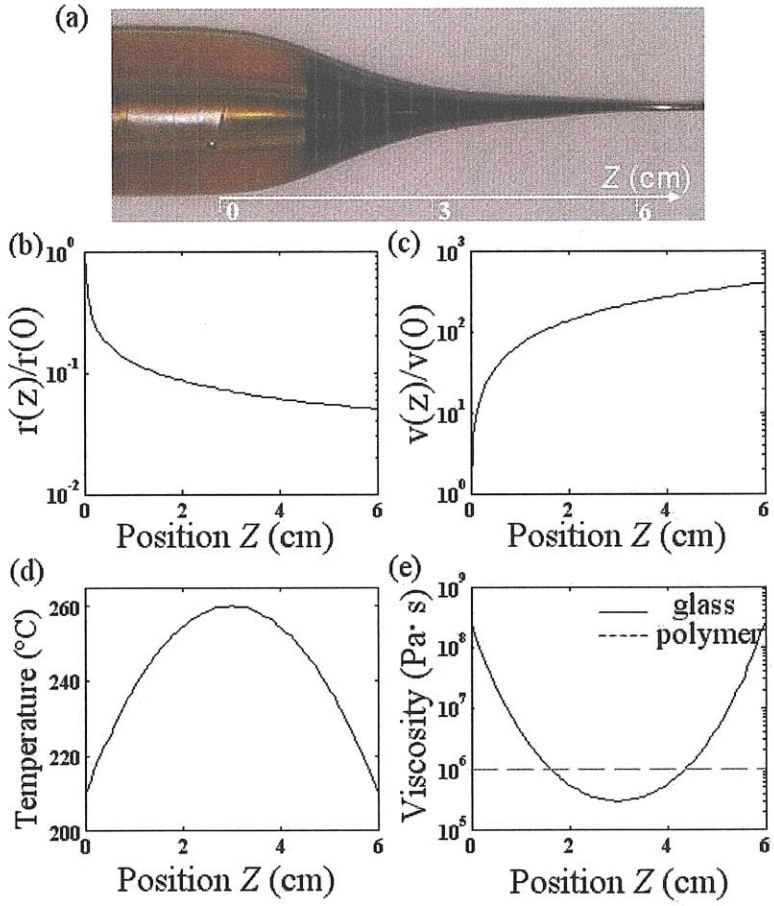

Figure 6-8: Relevant parameters in the neck-down region during thermal drawing. **(a)** Photograph of neck-down region from preform to fiber, **(b)-(e)** for the calculated dimensionless quantities of radius, velocity, temperature and viscosity, respectively.

where $z \in [0, L]$ is axial position in the neck-down region with length (L = 6 cm). $\Gamma \gg 1$ corresponds to breakup, while $\Gamma \ll 1$ corresponds to stability.

In order to provide a conservative estimation of filament stability, the capillary instability time is calculated from the fastest growth factor at each axial location, and the polymer viscosity is set to be the minimum value (at the highest temperature) during thermal drawing. The capillary instability time scale is calculated based on the Tomotika model as follows [66],

$$\tau(z) = \frac{2r\eta_{\text{polymer}}(z,T)}{\gamma[\max_{\lambda}(1-x^2)\Phi(x,\eta_{\text{polymer}}(z,t)/\eta_{\text{clad}}(z,t))]}. \tag{6.19}$$

The complex shape of neck-down profile is fitted from experiment can be approximately described by following formula,

$$\frac{R(z)}{R(0)} = (1+kz)^{-1/p}, \qquad k = (\frac{R(L)}{R(0)})^p - 1, \qquad p = 2. \tag{6.20}$$

Due to the incompressibility of the viscous fluid, the velocity of flow scales inversely with area:

$$\frac{v(z)}{v(0)} = \frac{R^2(0)}{R^2(z)}, \tag{6.21}$$

where v(0) = 4×10^{-3}mm/sec is the preform velocity. Again by incompressibility, the filament radius (r) should scale as the fiber radius (R):

$$\frac{r(z)}{r(0)} = \frac{R(z)}{R(0)}. \tag{6.22}$$

The temperature distribution during thermal drawing, fit from experiment, is found to be approximately parabolic,

$$T = T_{max} - (T_{max} - T_{min})(2\frac{z}{L} - 1)^2, \tag{6.23}$$

In calculations, parameters for the typical As_2Se_3 $--$PES fiber drawing are R(0) = 1 cm, s = 20, L = 6 cm, p = 2, $T_{max} = 260°C$, $T_{min} = 210\,°C$, r(L) = 200 nm, $\eta_{polymer} = 10^6$ Pa·s. Fig. 6-8 (b)–(d) presents the corresponding position–dependent variables including radius, velocity, temperature and viscosity. Finally, we obtain

$$\Gamma = 0.90. \tag{6.24}$$

This is $\Gamma < 1$, but only barely–if this were an accurate estimate of the growth factor, instability might still be observed. However, the assumptions we made above were so conservative that the true growth factor must be much less than this, indicating the instability should not be observable during the dwelling time of fiber drawing. So the observed filaments are consistent with the Tomotika model, although of course we cannot yet exclude the possibility that there are also additional effects (*e.g.*, elas-

ticity) that further enhance stability.

6.7 Summary

In this chapter, we have discussed the general physical picture of thermal drawing to understand the attainable structures (such as thin cylindrical shells and filaments) and the relevant feature sizes. In particular, a classic fluid instability, capillary instability, is focused. Numerical calculation is carried out to study instability growth rate, which depends on wavelength and viscosity. Finally, we model the complex fiber drawing with position-dependent velocity, radius, temperature, and viscosity. We find the capillary instability time under the conservative estimation is still slower than the experimental drawing time scale, which means the instability has insufficient time to develop. This analysis is consistent with the observed continuous filaments.

Chapter 7

Numerical simulation of capillary instability in cylindrical shell

7.1 Introduction

In the previous Chapter 6, we outline three theoretical questions of stability of attained cylindrical shell, stability of continuous filaments, and instability of azimuth breakup at further reduced thickness. We have discussed that the continuous filaments are consistent with the capillary instability which has insufficient time to develop during thermal drawing. By calculating the capillary instability time from linear theory of Tomotika model, we find the instability time under conservative estimate is slower than drawing time. In this Chapter, we will investigate the impact of capillary instability leading to radial fluctuations in cylindrical fluids in the previously unstudied case of concentric shells with different viscosity, a first step towards understanding instabilities in drawn cylindrical shells.

To isolate this mechanism from other forms of instability, we consider only cylindrically symmetrical geometries, which also greatly simplifies the problem into two dimensions (r, z). We model this situation by direct numerical simulation via a finite-element method for the Navier–Stokes (NS) equations. After first reproducing the known results from the linear theory for equal viscosity, we are able to explore the regime beyond the limits of the linear theory, which we show is accurate up to fluctu-

ations of about 10% in radius. For the case of unequal-viscosity shells, we show that the instability timescale interpolates smoothly between two limits that can be understood by dimensionless analysis. Finally, we apply our results to the experimental fiber-drawing situation, where we obtain a necessary (but not sufficient) condition for stability that can be used to guide the materials selection and the design of the fabrication process by excluding certain materials combinations from consideration. Our stability criterion is shown to be consistent with the experimental observations.

Motivated by the desire to understand the range of attainable structures and improve their performance, previous theoretical study of microstructured fiber drawing has considered a variety of situations different from the one considered here. Air-hole deformation and collapse was explored by numerical analysis of the continuous drawing process of microstructured optical fibers [78, 79]. Surface-tension effects have been studied for their role in determining the surface smoothness and the resulting optical loss of the final fibers [80]. The modeling of non-circular fibers has also been investigated in order to design fiber-draw process for unusual fiber shapes with a square or rectangular cross-section [81].

As a first step towards understanding these observations, we will consider simplified geometries consisting of a thin cylindrical shell in the cladding matrix. The question, here, is whether the classical capillary instability from radial fluctuations is relevant to the attained thin uniform shells. Moreover, we want to know whether classical capillary instability can provide guidance for materials selections and fabrication processing in our microstructured fibers. The observed azimuthal breakup at further reduced thicknesses need more future work by 3D numerical simulation.

7.2 Linear theory of concentric cylindrical shell with equal viscosities

A linear theory of capillary instability for the co-axial cylinder with equal viscosities is provided in the literature by Stone and Brenner [67]. The growth rate (σ) for a

wave vector $k = 2\pi/\lambda$ is a solution of the following quadratic equations,

$$(\sigma - \frac{k^2\gamma_1}{r\eta}(1-(rk)^2)\Lambda(r,r))(\sigma - \frac{k^2\gamma_2}{R\eta}(1-(Rk)^2)\Lambda(R,R)) = \frac{k^4\gamma_1\gamma_2}{rR\eta^2}(1-(rk)^2)(1-(Rk)^2)\Lambda(r,R)^2, \tag{7.1}$$

where r and R is radius of unperturbed interface I and II, γ_1 and γ_2 are interfacial tensions at interface I and II, η is viscosity. $\Lambda(a,b)$ is associated with Bessel function,

$$\Lambda(a,b) = \int_0^\infty \frac{sJ_1(sa)J_1(sb)}{(s^2+k^2)^2}ds = -\frac{1}{2k}\frac{d}{dk}(I_1(ak)K_1(bk))(a \le b). \tag{7.2}$$

For the case of $\gamma_1 = \gamma_2 = \gamma$, the growth rate has the following formula,

$$\sigma(\lambda) = \frac{\gamma}{\eta r}\Psi(\lambda, R/r), \tag{7.3}$$

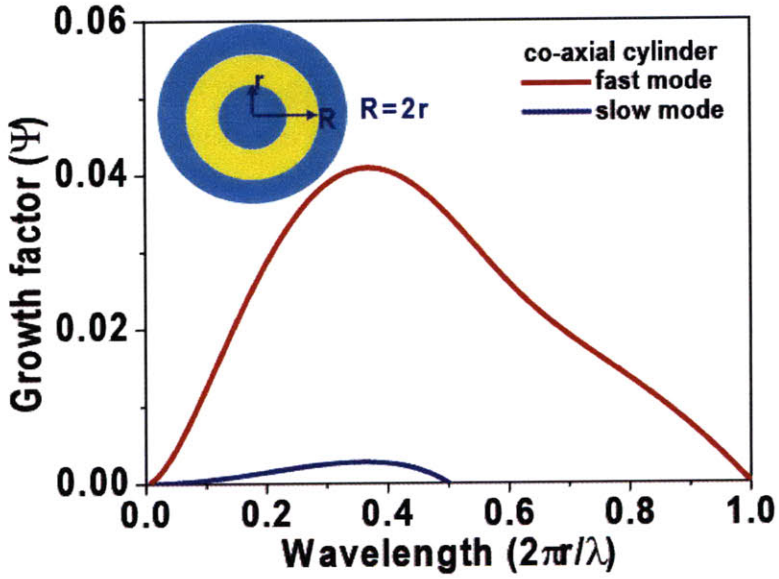

Figure 7-1: Growth factor of instability as a function of wavelength. Fast and slow modes occur at wavelengths above their respective critical wavelengths λ_f, λ_s. Inset is a sketch of coaxial cylinder with radius $R = 2r$ and equal viscosities.

The instability time scale $\tau \sim \sigma^{-1} \sim \eta r/\gamma$ is scaled with radius. The growth factor of $\Psi(\lambda, R/r)$ in Eq. 7.3 is a complicated function of instability wavelength. For the case of $R = 2r$, this growth factor is calculated in figure 7-1. A positive growth factor

indicates a positive growth rate ($\sigma > 0$), and perturbation is exponentially amplified with time. Instability occurs at long wavelength above a certain critical wavelength. Two critical wavelengths exist for the co-axial cylinder shell. One is a short critical wavelength $\lambda_f = 2\pi r$ for faster growth mode in red line. The other is a long critical wavelength $\lambda_s = 2\pi R$ for slower growth mode in blue line.

7.3 Govern equations

During thermal drawing, the temperature is set above the softening points of all the materials, which consequently are in the viscous fluid state to enable fiber co–drawing. To describe this fluid flow, we consider the incompressible NS equations:

$$\begin{cases} \rho(\partial_t \vec{u} + (\vec{u} \cdot \nabla)\vec{u}) = -\nabla p + \eta \nabla^2 \vec{u} - \gamma \kappa \vec{n} \delta, \\ \nabla \cdot \vec{u} = 0, \end{cases} \tag{7.4}$$

where $\vec{u}$ is velocity, p is pressure, η is viscosity, γ is interfacial tension, ρ is density, δ is the delta function on the interface, κ is curvature of interface, and $\vec{n}$ is a unit vector at interface [83].

7.4 Simulation algorithm

To develop a quantitative understanding of capillary instability in a cylindrical-shell geometry, direct numerical simulation is performed using the finite element method. In order to isolate the effect of radial fluctuations, we impose cylindrical symmetry, so the numerical simulation simplifies into a 2D problem in the (r, z) plane (where the ∇ operations are replaced by their cylindrical forms). Although the low Re number means that one could accurately neglect the $(\vec{u} \cdot \nabla)\vec{u}$ nonlinear inertia term and solve only the time-dependent Stokes problem, we solve the full NS equations because of the convenience of using available software supporting these equations and also to retain the flexibility to consider large Re regimes in the future.

Our simulation algorithm is briefly presented in figure 7-2(a). The geometry

of a cylindrical shell is defined by two interfaces I and II in figure 7-2(b). The flow field $(\vec{u}, p)$ is calculated from Navier–Stokes equations, as seen in figure 7-2(c). Consequently, this new flow field generates interface motion, resulting in an updated interface and an updated flow field. By these numerical iterations, the interface gradually evolves with time.

More specifically, the time-dependent interfaces I and II can be expressed as follows:

$$\begin{cases} r_1(z,t) = r_0 + \varepsilon_1(z,t), \\ r_2(z,t) = 2r_0 + \varepsilon_2(z,t), \end{cases} \tag{7.5}$$

where $r_0, 2r_0$ are the unperturbed radii of interface I and II, $\varepsilon_1(z,t), \varepsilon_2(z,t)$ denote the interfacial perturbations that grow with time.

The initial perturbations at interface I and II are given by cosine-wave shapes:

$$\begin{cases} \varepsilon_1(z,0) = \varepsilon_0 \cos(2\pi z/\lambda), \\ \varepsilon_2(z,0) = 2\varepsilon_0 \cos(2\pi z/\lambda), \end{cases} \tag{7.6}$$

where $\varepsilon_0, 2\varepsilon_0$ are the perturbation amplitudes, and λ is the initial perturbation wavelength.

Numerical challenges in the simulations arise from the nonlinearity, moving interfaces, interface singularities, and the complex curvature [61, 86]. A level-set function (ϕ) is coupled with the NS equations to track the interface (see Appendix 1) [87, 88, 89], where the interface is located at the $\phi = 0.5$ contour and the ϕ evolution is given by $\vec{u}$ via:

$$\phi_t + \vec{u} \cdot \vec{\nabla}\phi = 0. \tag{7.7}$$

The local curvature (κ) at an interface is given in terms of ϕ by:

$$\kappa = \nabla \cdot \vec{n} = \nabla \cdot \frac{\nabla\phi}{|\nabla\phi|} = \frac{(\phi_r^2\phi_{zz} + \phi_z^2\phi_{rr}) + (\phi_r^2 + \phi_z^2)\phi_r/r - \phi_r\phi_z(\phi_{rz} + \phi_{zr})}{(\phi_r^2 + \phi_z^2)^{3/2}}. \tag{7.8}$$

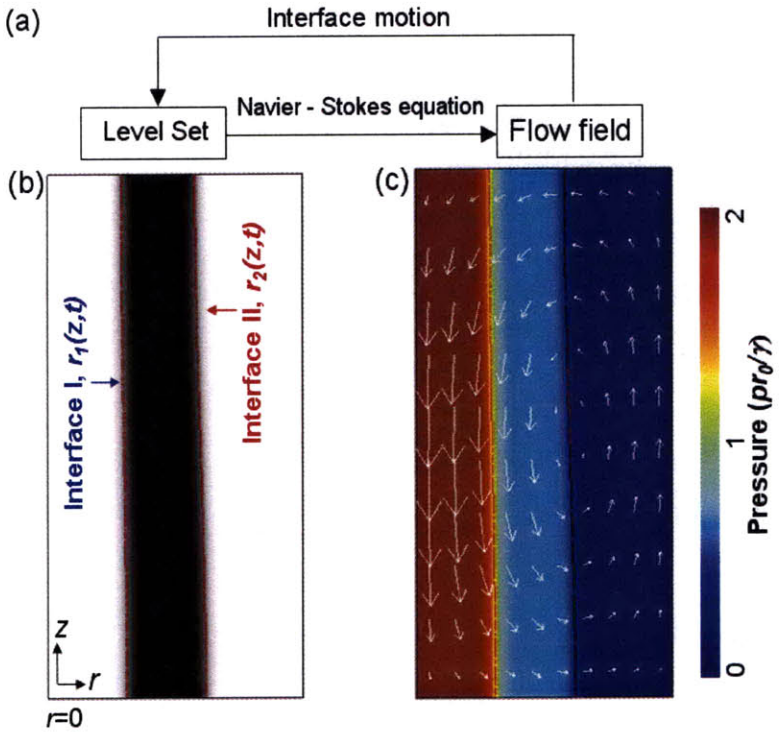

Figure 7-2: Simulation algorithm. (a) Chart of algorithm. (b) Interface I and II of cylindrical shell is defined by the level set function, which evolves with flow field. (c) Flow field is determined by the NS equations. Dark color in (b) for cylindrical shell region; color scale in (c) for pressure and arrows for fluid velocity.

In the simulation, level set function is defined by a Heavy-side function [90],

$$\phi(z,t) = \begin{cases} 0, r < (r_1(z,t) - \Lambda), r > (r_2(z,t) + \Lambda), \\ 0.5, (r_1(z,t) - \Lambda) < r < (r_1(z,t) + \Lambda), (r_2(z,t) - \Lambda) < r < (r_2(z,t) + \Lambda), \\ 1, (r_1(z,t) + \Lambda) < r < (r_2(z,t) - \Lambda), \end{cases} \tag{7.9}$$

where $r_1(z,t)$ and $r_2(z,t)$ are the radius of interface$I$ and II of coaxial cylinder, and Λ is the half thickness of interface. Level set $\phi = 1, 0$ corresponds to the region of concentric cylindrical shell and surrounding fluid, respectively. Contour $\Pi = \{X | \phi(X,t) = 0.5\}$ tracks the interface I and II.

A delta function is defined to project surface tension at interface,

$$\delta = 4\phi(1-\phi) = \begin{cases} 1, (r_1 - \Lambda) < r < (r_1 + \Lambda), (r_2 - \Lambda) < r < (r_2 + \Lambda), \\ 0, r < (r_1 - \Lambda), r > (r_2 + \Lambda), (r_1 + \Lambda) < r < (r_2 - \Lambda). \end{cases} \tag{7.10}$$

A step function is introduced for the smooth transition of level function ϕ from 0 to 1 across interface,

$$\phi = (1 + exp((r - r_1))/\Lambda))^{-1} - (1 + exp((r - r_2))/\Lambda))^{-1}. \tag{7.11}$$

The boundary condition for the level set equation is

$$\vec{n} \cdot (-c\nabla\phi + \phi\vec{u}) = 0, \tag{7.12}$$

where $\vec{n}, \vec{t}$ is the normal and tangential vector at the boundaries.

In addition, boundary conditions for the NS equations are

$$\begin{cases} \vec{n} \cdot \vec{u} = 0, \\ \vec{t} \cdot \eta(\nabla\vec{u} + (\nabla\vec{u})^T) = 0, \end{cases} \tag{7.13}$$

7.5 Simulation results

In the low Re regime, the NS equations are linear with the respect to flow velocity $\vec{u}$ because the inertia term $(\vec{u}\cdot\nabla)\vec{u}$ is negligible, but they are not linear with the respect to the geometry of the interface shape except in the limit of small perturbations. A linear theory for small geometric perturbations was solved for the cylinder by Tomotika [66] and for a cylindrical shell with a cladding of equal viscosity by Stone and Brenner [67]. Our full simulation should, of course, reproduce the results of the linear theory for small perturbations, but also allows us to investigate larger perturbations beyond the regime of the linear theory, and we can also consider the more general case of a cylindrical shell with a cladding of unequal viscosity.

7.5.1 Numerical convergence

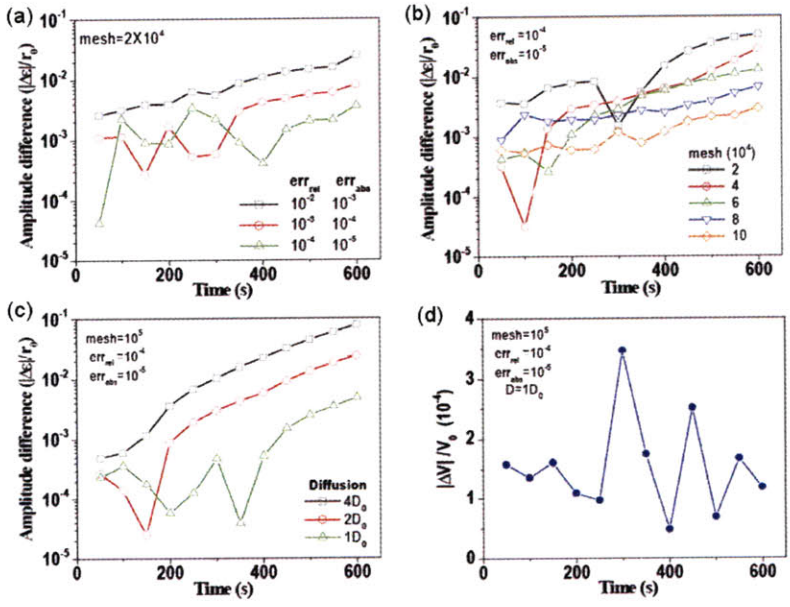

Figure 7-3: Numerical convergence of (a) the mesh size, (b) the relative and absolute error, and (c) the diffusion coefficient. (d) Numerical error of shell volume is less than 10^{-4}.

In order to establish the accuracy of the simulation, we first investigated the convergence with respect to the various approximations: the time integration tolerance

($\rightarrow 0$), the mesh resolution ($\rightarrow \infty$), and an artificial diffusion term D ($\rightarrow 0$). Finite element meshes are generated by the triangular method, and second order quadratic basis functions are used in the simulation. In the simulation, numerical error is controlled by the absolute and relative error (err_{abs} and err_{rel}) for each integration step. U is the solution vector at a given time step, E is the solver's estimated local error in U during this time step, and N is the number of degrees of freedom in the simulation. The step is accepted if the following condition is satisfied,

$$(\frac{1}{N}\sum_i(\frac{|E_i|}{err_{abs}+err_{rel}|U_i|})^2)^{1/2} < 1. \tag{7.14}$$

The time integration is performed by a fifth-order backward differentiation formula, characterized by specified relative and absolute error tolerances ($\mathrm{err_{rel}}$ and $\mathrm{err_{abs}}$). Figure 7-3(a) shows the convergence of the instability amplitude $\min_z \varepsilon_1(z,t)$ as a function of time, as these tolerances $\rightarrow 0$, compared by the difference $|\Delta\varepsilon|/r_0$ with the result at low tolerances $\mathrm{err_{rel}} = 10^{-5}$ and $\mathrm{err_{abs}} = 10^{-6}$. We find that tolerances of $\mathrm{err_{rel}} = 10^{-4}$ and $\mathrm{err_{abs}} = 10^{-5}$ yield acceptable accuracy ($\approx 10^{-3}$). Figure 7-3(b) shows the convergence of $|\Delta\varepsilon|/r_0$ with respect to the number of triangular mesh elements, compared with a very fine mesh of $12 \cdot 10^4$ mesh elements. We found $10 \cdot 10^4$ mesh elements, corresponding to a typical element diameter $\approx 0.01 r_0$, yield good accuracy ($\approx 10^{-3}$ error). To ensure numerical stability in the simulation, an artificial diffusion term, $\nabla \cdot (c\nabla\phi)$ is added to the right side of the level-set Eq. 7.7, where $c = D - \phi(1-\phi)D$ for some diffusion coefficient D [90]. The physical results are recovered in the limit $D \rightarrow 0$, and so we must establish the convergence of the results as D is reduced and identify a D small enough to yield accurate results while still maintaining stability. Figure 7-3(c) demonstrates this convergence in the simulation by calculating the amplitude difference $|\Delta\varepsilon|/r_0$ compared with $D = 0.5D_0$ ($D_0 = 10^{-14}\mathrm{m}^2/\mathrm{s}$ in Appendix 1), and 3 digits of accuracy are attained by $D = D_0$. Accordingly, the numerical parameters throughout the following simulations are $err_{rel} = 10^{-4}, err_{abs} = 10^{-5}, D = 1.0D_0$, and $10 \cdot 10^4$ mesh elements. As an additional check, the volume of the incompressible fluid shell between the two interfaces should

be conserved. As shown in figure 7-3(d), the numerical errors in the simulation leads to only a small volume deviation, ($|V(t) - V(0)|/V(0) = |\Delta V(t)|/V(0)$), of less than 0.4%. We conclude that the finite-element level-set approach is numerically reliable for the simulation of capillary instabilities.

7.5.2 Instability evolution

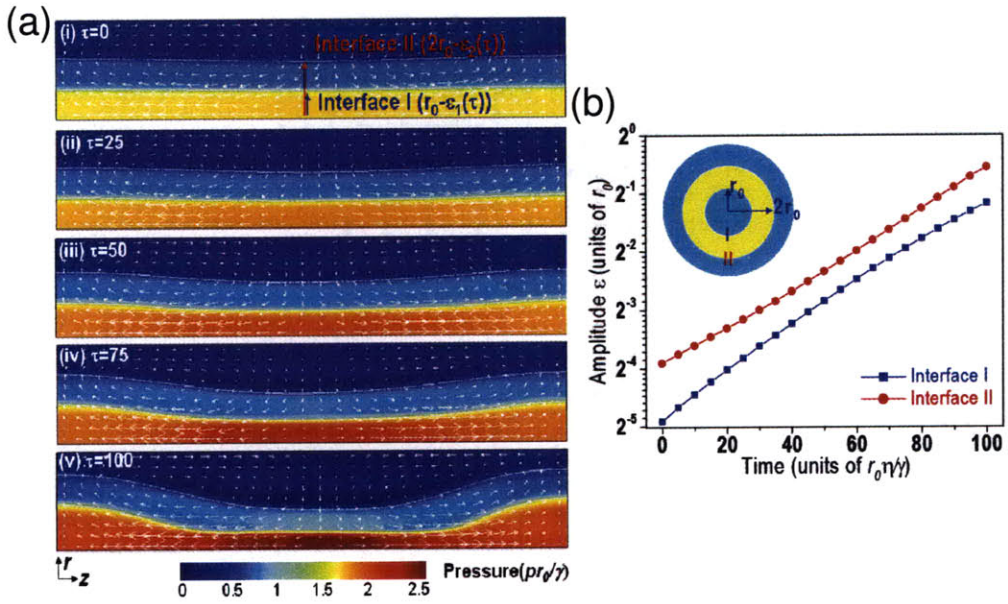

Figure 7-4: (a) Snapshot of instability evolution. The small-amplitude perturbation at interface is magnified by fluid flow moving from a smaller-radius to a larger-radius region. Color scale for pressure, arrows for fluid velocity. (b) The instability amplitude at interface I and II grows with time, respectively.

The evolution of a capillary instability can be obtained from direct numerical simulation. Figure 7-4(a) (i)–(v) presents snapshots of the flow field and interface. (i) Initially, the pressure of the inner fluid is higher than that of the outer fluid due to Laplace pressure ($p = \gamma\kappa$) originating from azimuthal curvature of the cylindrical geometry at interfaces I and II. (ii)–(iv) The interfacial perturbations generate an axial pressure gradient Δp, and hence a fluid flow occurs that moves from a smaller-radius to a larger-radius region for the inner fluid. Gradually the amplitude of the perturbation is amplified. (v) The *shrunk* smaller-radius and *expanded* larger-radius

regions of inner fluid further enhance the axial pressure gradient Δp, resulting in a larger amplitude of the perturbation. As a result, the small perturbation is exponentially amplified by the axial pressure gradient. Physical parameters for figure 7-4 in the simulation are $\rho = 10^3$ kg/m^3, $\eta = 10^5$ Pa $\cdot$ s, $\gamma = 1$ N/m, $R = 100$ μm, $err_{rel} = 10^{-4}, err_{abs} = 10^{-5}$, $D = D_0 = 10^{-14}$ m^2/s.

Figure 7-4(b) shows the instability amplitude $\min_z \varepsilon(z,t)$ at interfaces I and II growing with time exponentially on a semilog scale in the plot. The instability time scale in the simulation is about 372 ± 3 sec by fitting the curve to an exponential $\varepsilon \sim e^{t/\tau}$. In the numerical simulation, the wavelength is chosen between these two wavelengths ($\lambda_f < \lambda < \lambda_s$) , and only fast modes exist. From the simulation parameters $\eta \approx 10^5$ Pa $\cdot$ s and $\gamma/r \approx 10^4$ Pa $\cdot$ s together with wavelength $2\pi r/\lambda \approx 0.47$ corresponding to growth factor $\Psi(\lambda) \approx 0.03$, linear theory predicts instability time scale $\tau = \sigma^{-1} = (\frac{\gamma}{\eta r}\Psi(\lambda, R/r))^{-1} \approx 334$ sec. Thus, simulation is consistent with the linear theory, in terms of the instability time scale.

7.5.3 Beyond the linear theory

More quantitatively, for small perturbations or short times, exponential growth of the perturbation amplitude is expected from the linear theory. However, after a long time, when the perturbation has grown sufficiently, one expects the linear theory to break down. We observe significant deviations from the linear theory if the amplitude is above 10% of the cylinder radius r (corresponding to time $40r\eta/\gamma$), as shown in figure 7-5 (taking interface I as an example). For example, at perturbation amplitudes of around 25% of r (time $70r\eta/\gamma$), the deviations of the simulation data from the linear theory is almost 20%.

The length scaling of the instability is studied as well. After rescaling time and distance by the same factor (so that the initial radius is scaled by $0.25, 0.5, 1, 2$, and 4), all the data collapse onto one master curve, as shown in figure 7-5. This length scaling originates from the low Re regime, which implies that the NS equations are approximately linear with respect to $\vec{u}$; this gives rise to a well known scale invariance in the Stokes regime [83].

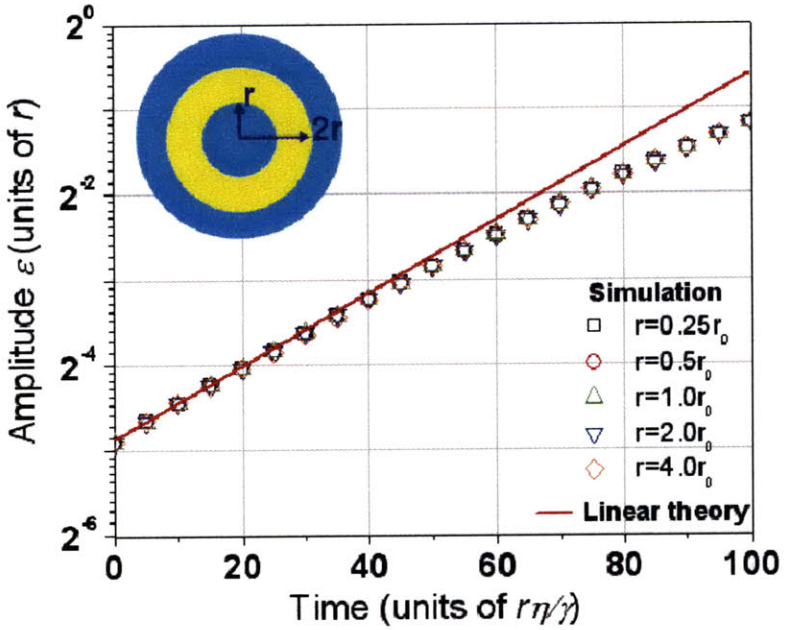

Figure 7-5: Time-dependent amplitude of perturbation and length scaling for the different radii. For an amplitude of instability below 10% r, data agree well with exponential growth from linear theory. However, as the amplitude of instability is above 10% r, a noticeable deviation from linear theory occurs. Rescaling time, amplitude by a same radius factor; all the data collapse onto one master curve in simulation.

7.5.4 Unequal viscosities

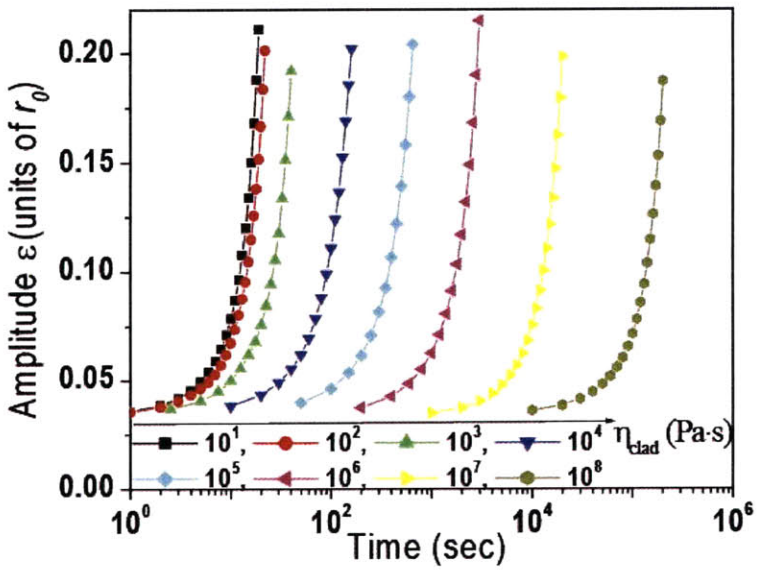

Figure 7-6: Time-dependent perturbation amplitude for various cladding viscosities with a fixed shell viscosity.

We now investigate the dependence of instability timescale on cladding viscosity (η_{clad}) with a fixed shell viscosity (η_{shell}), in order to help us to identify suitable cladding materials for fiber fabrication. As viscosity slows down fluid motion, the low-viscosity cladding has a faster instability growth rate and a shorter time scale, while the high-viscosity cladding has a slower instability growth rate and a longer instability time scale. Figure 7-6 shows the time-dependent perturbation amplitude curves for various viscosity contrast $\eta_{\text{clad}}/\eta_{\text{shell}}$ by changing the cladding viscosity ($\eta_{\text{shell}} = 10^5$ Pa $\cdot$ s). Instability time scale (τ) for the each given viscosity contrast is obtained by exponentially fitting the curves in figure 7-6. Instability time scale as a function of viscosity contrast is presented in figure 7-7, and instability time scale at interface I is comparable with that at interface II for all the cladding viscosity in the simulations.

The existing linear theory has only been solved in case of equal viscosity, and predicts that the instability time scale is proportional to the viscosity $\tau \sim \eta$ [67].

We obtain a more general picture of the instability time scale for unequal viscosity by considering two limits. In the limit of negligible cladding viscosity, $\eta_{\text{clad}} \to 0$, the instability time scale should be determined by η_{shell}, and from dimensional analysis should be proportional to $r\eta_{\text{shell}}/\gamma$, assuming that the inner and outer radius are comparable and so we take r to be the average radius. In the opposite limit of $\eta_{\text{clad}} \to \infty$, the time scale should be determined by η_{clad} and hence should be proportional to $r\eta_{\text{clad}}/\gamma$. In between these two limits, we expect the time scale to smoothly interpolate between the $r\eta_{\text{shell}}/\gamma$ and $r\eta_{\text{clad}}/\gamma$ scales. Precisely this behavior is observed as shown in figure 7-7.

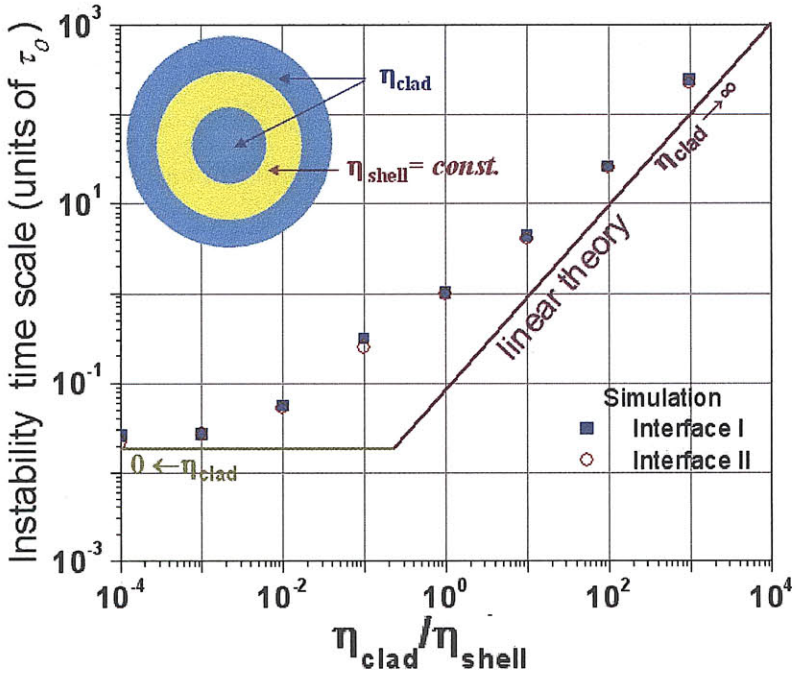

Figure 7-7: An instability time scale (τ) dependent on cladding viscosity with the fixed shell viscosity. At the limit of $\eta_{clad} \to 0$, the time scale is approaching a constant; at the other limit of $\eta_{clad} \to \infty$, the time scale is linearly proportional to η_{clad}.

7.6 Estimate of radial instability timescale

In the previous section, we surveyed the capillary instability of a concentric-cylindrical shell by numeral simulations. We proceed to apply these results to investigate the instability time scale dependent on various physical parameters including geometry (e.g., radius and shell thickness) and materials properties (viscosity) in a broad range, exploiting the accuracy of simple dimensional analysis demonstrated in the previous section and providing guidance of our fiber drawing.

Calculated instability time scale (τ) for different values of the radius (r) and the viscosity (η) is displayed in figure 7-8. The cross-sectional geometry in the calculation is shown in the inset: interface Iis located at radius r, the cylindrical-shell thickness is h, and interface II is at radius $R = r+h$. The interfacial tension in the calculations was set $\gamma = 0.1\text{N/m}$, which was the measured interfacial tension between thermoplastic polymer and chalcogenide glass used in our microstructured fibers [84].

Two cases are considered: one is equal viscosity ($\eta_{\text{shell}} = \eta_{\text{clad}}$), and the other is unequal viscosity ($\eta_{\text{shell}} \neq \eta_{\text{clad}}$). In the case of $\eta_{\text{shell}} = \eta_{\text{clad}}$, the instability time scale is calculated exactly from Stone and Brenner's linear theory [67],

$$\tau = \frac{\eta r}{\gamma \max_\lambda \Psi(\lambda, R/r)}, \tag{7.15}$$

where the fastest growth factor $\max_\lambda \Psi(\lambda, R/r)$ was found by searching numerically within a wide range of wavelengths λ for a certain value of R/r (Eq. 7.3 in Appendix 2). Figure 7-8 plots the time scale versus radius for $\eta = 10^5 \text{Pa} \cdot \text{s}$ corresponding to $As_2Se_3 - \text{PES}$, compared to the time scale $\tau_{\text{exp}} \approx 100$ sec of our fiber drawings[85].

In the other case of $\eta_{\text{shell}} \neq \eta_{\text{clad}}$ (at the limit of $\eta_{\text{clad}}/\eta_{\text{shell}} \gg 1$ as discussed in Section 7.5.4), the instability time scale can be roughly estimated from dimensional analysis. Although dimensionless analysis does not give the constant factor, for specificity, we choose the constant coefficient from the Tomotika model [66],

$$\tau \approx \frac{2r\eta_{clad}}{\gamma \max_\lambda (1-x^2)\Phi(x, \eta_{clad}/\eta_{shell})}, \tag{7.16}$$

where the fastest growth factor $\max_\lambda(1-x^2)\Phi(x, \eta_{clad}/\eta_{shell})$ was found numerically by searching a wide range of wavelengths ($x = 2\pi r/\lambda$) [$\Phi(x, \eta_{clad}/\eta_{shell})$ is a complicated implicit function of wavelength and viscosity contrast]. Figure 7-8 plots the time scale for $\eta_{\text{shell}} = 10$ Pa $\cdot$ s, $\eta_{clad} = 10^5$ Pa $\cdot$ s corresponding to Se $-$ PSU, showing that the observed stability of shells of radius $\sim 500\mu$m is consistent with radial stability ($\tau > \tau_{\text{exp}}$). On the other hand, if η_{clad} is reduced to 10^3Pa $\cdot$ s with the same shell materials, corresponding to Se $-$ PE, we predict that radial fluctuations alone will render the shell unstable for radius r $\leq$ 1mm.

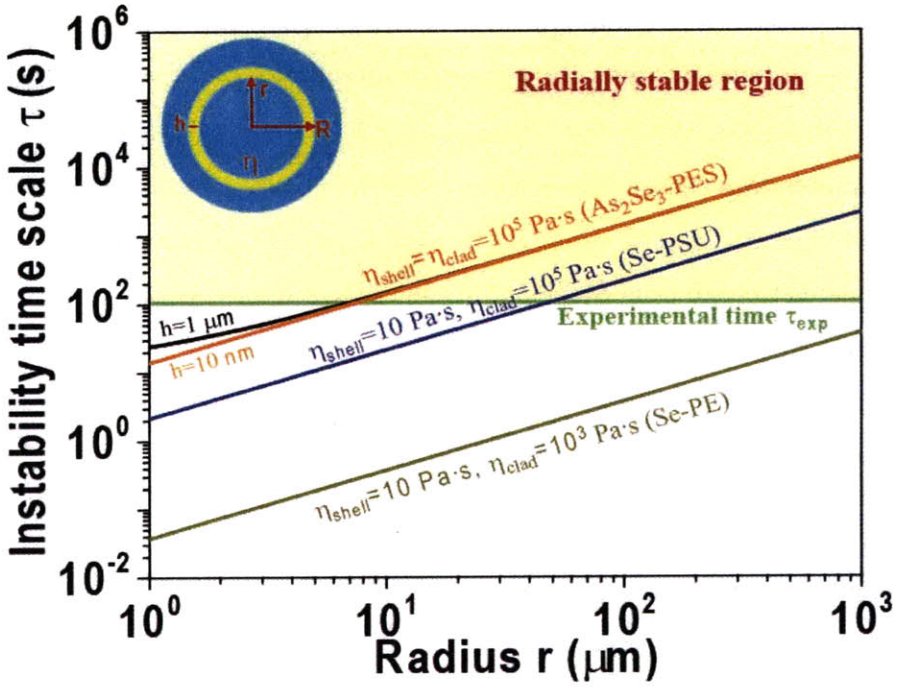

Figure 7-8: Radial stability map. Linear theory calculations of instability time scale dependent of the radius, thickness, and viscosity. Experimental time scale of thermal drawing around $\tau_{exp} \approx 100$ sec, and fiber radius $r \approx 500$ μm. Inset shows the cross-sectional geometry of cylindrical shell. Radially stable region for $\tau_{ins} > \tau_{exp}$, while unstable region for $\tau_{ins} < \tau_{exp}$.

7.7 Applications in microstructured fibers

In this section, we consider in more detail the application of these analyses to understanding observed experimental results, and in particular the observed stability (or instability) of thin shells and filaments. We examine whether our stability analysis can provide guidance in materials selection and in the the understanding of attainable feature sizes. Because we only considered radial fluctuations, our analysis provides a necessary but not sufficient criterion for stability. Therefore, the relevant questions are whether the criterion is *consistent* with observed stable structures, whether it is sufficient to explain the observed azimuthal breakup, and what materials combinations are *excluded*. Below, in Sec 7.7.1 we consider the application of radial stability analysis to the observed stability or instability of cylindrical shells. In Sec 7.7.2 we look at the impact on materials selections. Finally, in Sec **??**, we show that the observed stability of the resulting nanoscale filaments is consistent with the Tomotika model.

7.7.1 Comparison with observations for cylindrical shells

The radial stability map of figure 7-8 is consistent with the experimental observations (the default cylindrical shell radius ≈ 250 μm). First, the map predicts that feature size down to submicrometers and hundreds of nanometers are consistent with radial stability for the equal–viscosity materials combination of $\eta_{\text{clad}} = \eta_{\text{shell}} = 10^5$ Pa $\cdot$ s, which corresponds to As_2Se_3–PES or As_2S_3–PEI. For As_2Se_3–PES, Figure 6-2 (c) shows that a shell thickness of As_2S_3 of 1 μm is obtained; in other work, layers of As_2S_3 down to 15 nm have been achieved as well [42]. For As_2S_3–PEI, figure 6-2 (d) demonstrates a thickness of As_2S_3 down to 32 nm. Second, the map is consistent with thickness down to submicrometers for unequal–viscosity materials with $\eta_{\text{clad}} = 10^5$ Pa $\cdot$ s, $\eta_{\text{shell}} = 10$ Pa $\cdot$ s, which corresponds to Se–PSU. Se layers with thickness on the order of 1 μm have been demonstrated in Se–PSU fiber [42].

The radial stability map, nevertheless, is not sufficient to explain the azimuthal instability at further reduced thickness down to tens of nanometers. The stability

map of figure 7-8 predicts that a Se layer in a Se–PSU combination should be *radially* stable down to tens of nanometers. However, we found in experiments [figure 6-2(e, f)] that Se shell with thickness < 100 nm breaks up into continuous filament arrays [42], which means that the mechanism for this breakup is distinct from that of purely radial fluctuations. For another As_2Se_3–PES materials combination, this filamentation of As_2Se_3 film was also observed as the thickness is reduced down to 10 nm [42]. Future work will elucidate this filamentation mechanism by performing 3D numerical simulation to explore the azimuthal fluctuations.

7.7.2 Materials selection

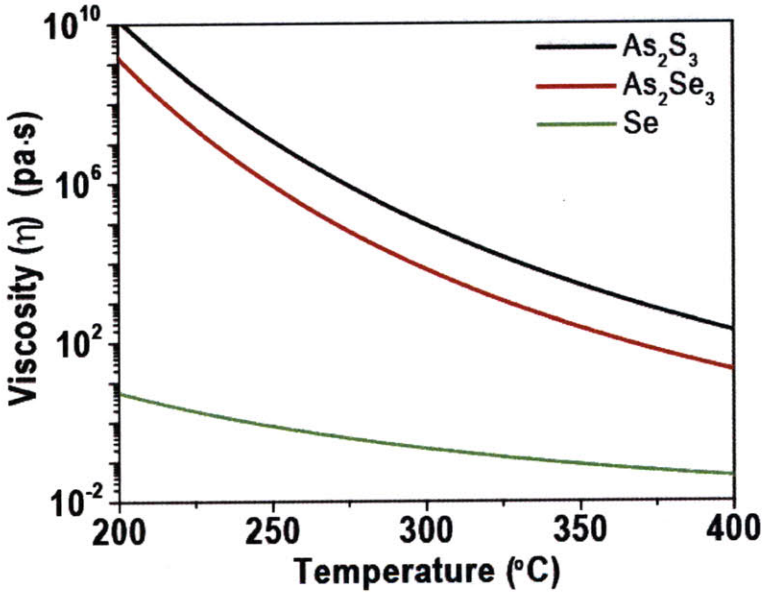

Figure 7-9: Temperature-dependent viscosity for various chalcogenide glasses. Typical temperature during fiber drawing for glass Se, As_2Se_3, As_2S_3 is around 220, 260, 300 °C with the corresponding viscosities of $10, 10^5, 10^5$ Pa · s, respectively

Given the viscosities and surface tension of a particular material pair, we can use figure 7-8 to help determine whether that pair is suitable for drawing: if it is radially unstable, then it is almost certainly unsuitable (unless the process is altered to

converse somehow), whereas if it is radially stable then the pair is at least potentially suitable (if there are no other instability).

As glassy materials have a continuous viscosity-temperature dependence for high-speed drawing, the materials choices in our fiber system are chalcogenide semiconductor (such as selenium, Se; arsenic triselenide As_2Se_3; and arsenic trisulfide, As_2S_3) and thermoplastic polymers (such as polyethersulfone, PES; polyetherimide, PEI; and polysulfone, PSU). Three sets of aforementioned shell-cladding materials combinations ($Se - PSU$, $As_2Se_3 - PES$, and $As_2S_3 - PEI$) are listed in figure 7-10. Cladding materials of thermoplastic polymer (PSU, PES, PEI) have similar viscosities $\eta_{\text{polymer}} \approx 10^5$ Pa $\cdot$ s during fiber drawing [85]. Viscosities of these of semiconductor glasses (Se, As_2Se_3, As_2S_3) are calculated from an empirical Arrhenius formula and obtained from the corresponding temperature during thermal drawing

$$log\eta = log\eta_0 + Cexp(D/T)/2.3RT - 1, \tag{7.17}$$

where R is an ideal gas constant, T is temperature in the unit of kelvin, and η is viscosity in the unit of $Pa \cdot s$. Parameters of $log\eta_0, C, D$, which are related with special materials, are listed below: $-2.0, 6651, 770.82$ for Se, $-3.09, 18877.8, 875.56$ for As_2Se_3, and $-3.62, 33744, 650.8$ for As_2S_3 in the literature [94]. These viscosities over a wide temperature range are plotted in figure 7-9. More specifically, the typical temperature during a fiber drawing for Se, As_2Se_3, As_2S_3 film is set around $220, 260, 300$ °C with the corresponding viscosities of $10, 10^5, 10^5$ Pa $\cdot$ s, respectively.

Viscosities of materials used in fiber drawing are obtained as follows: the viscosities of semiconductor glasses (Se, As_2Se_3, As_2S_3) are calculated from an empirical Arrhenius formula at the associated temperature during thermal drawing; several thermoplastic polymers (PSU, PES, and PEI) have similar viscosities $\eta_{\text{polymer}} \approx 10^5$ Pa $\cdot$ s during fiber drawing [85]; and the viscosity of the polymer PE is 10^3 Pa $\cdot$ s at temperature T = 250°C [91]. The polymer–glass surface tension is typically $\gamma = 0.1$ N/m [84] for all of these materials. For materials combinations, assuming a cylindrical shell of radius ≈ 250 μm and a dwelling time of thermal drawing ≈ 100 sec, we

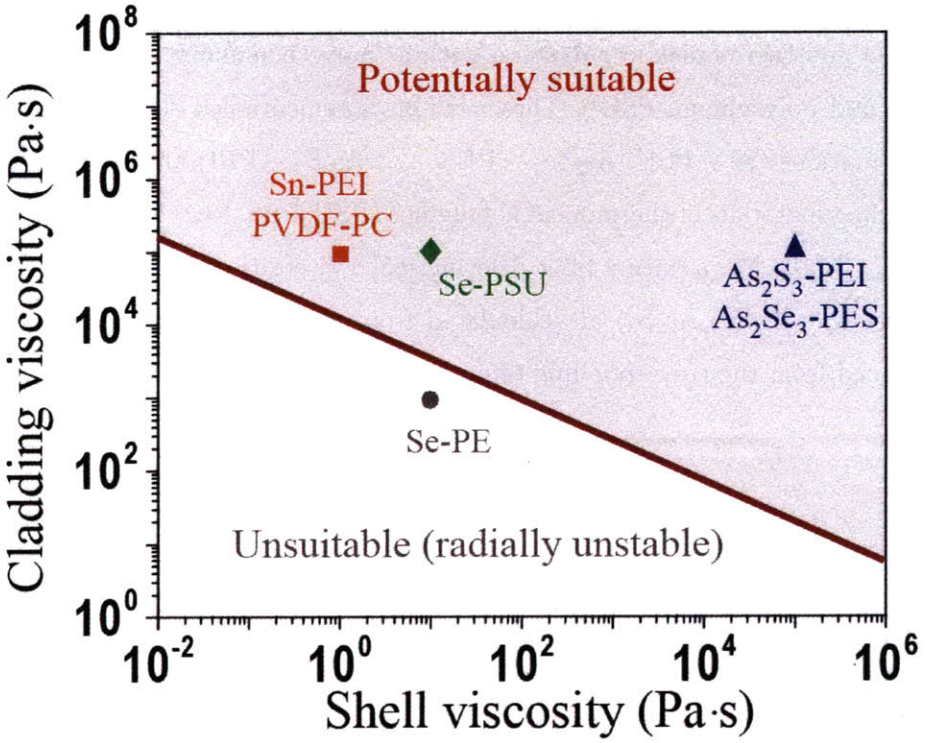

Figure 7-10: Calculated shell-cladding viscous materials selection map during thermal drawing ($\tau_{\text{dwelling}} = 100$ sec). A red line for instability time for dwelling time $\tau = \tau_{\text{dwelling}}$. The shaded region above red line for potentially suitable viscous materials combination ($\tau > \tau_{\text{dwelling}}$), which is consistent with identified shell-cladding materials combinations in our fiber drawings including semiconductor-polymer ($Se - PSU, As_2Se_3 - PES, As_2S_3 - PEI$), polymer-polymer($PVDF - PC$), and metal-polymer ($Sn - PEI$). The region below line for radially unstable materials combinations ($\tau < \tau_{\text{dwelling}}$), such as $Se - PE$ materials combination, is excluded in our thermal drawing.

can classify each materials combination by whether it falls in the $\tau > \tau_{\text{dwelling}}$ yellow region (radially stable) of figure 7-8 or in the $\tau < \tau_{\text{dwelling}}$ white region (radially unstable).

These materials combinations are presented in figure 7-10. The boundary line in red, which indicates the viscous combinations that satisfy $\tau = \tau_{\text{dwelling}}$, divides the map into two areas. The shaded area above the boundary line is the region of potentially suitable materials combinations for fiber drawing (As_2Se_3–PES, As_2S_3–PEI, Se–PSU); while the materials combinations below the boundary line are unsuitable with regarding to radial instability. Here, the only materials combination which seems to be definitely excluded in this regime due to radial instability is Se–PE. The polymer–polymer materials combination of PVDF–PC (polyvinylidene fluoride, PVDF, a piezoelectric polymer; polycarbonate, PC) is potentially suitable for thermal drawing, and this possibility has been confirmed by recent experiments [92]. Moreover, since a high viscosity cladding improves stability (increase τ), we predict that a wider variety of shell materials with low viscosity may possibly be employed in microstructured fibers, such as the metals Sn and In [77, 93]. These various available classes of metals, polymers and semiconductors expands the potential functionalities of devices in microstructured fibers.

7.8 Summary

In conclusion, capillary instability in a concentric cylindrical shell is explored by the direct numerical simulation of $2D$ NS equations. At smaller instability amplitude below $0.1r$, linear theory is applicable; at larger instability amplitude above $0.1r$, nonlinear effect due to geometry of deformed interface occurs. Instability time scale for the unequal viscosities, at two limits of cladding viscosity (zero and infinite), can be estimated from a known Tomotika model. Based on radial instability map calculated from linear theory calculation, the successful fabrication of uniform concentric cylinder shells with thickness down to nanometers in fibers is attributed to high viscosity ($\eta \approx 10^5$ Pa $\cdot$ s) and large radius ($r \approx 100$ μm). Nevertheless, more theoretical

work is required to understand the azimuthal instability of shell breakup. This work may provide an insightful theoretical guidance for us to rationally choose suitable material combinations and optimally control fabrication process, in order to maintain the desired nanostructures (such as nanotubes, nanoshells, and coaxial nanowires).

Chapter 8

Outlook and summary

8.1 Outlook

We have presented the observation of thin film breakup into filament arrays during thermal drawing and explored the relevant mechanism from a perspective of fluid instability. We will discuss the future directions which are based on the results in this thesis.

8.1.1 Nanowires with more complex structure

A single thin film breakup into nanowires was observed, and nanowires with more complicated cross-section geometry, such as coaxial nanowires, is suggested. First, a sandwiched structure of three-layer thin film, $\beta\alpha\beta$, is fabricated by thermal evaporation, where α and β stands for two different materials such as chalcogenide glass or metals. Second, after the sandwiched structure $\beta\alpha\beta$ is rolled into the polymer matrix, this preform is heated at high temperature and drawn into fiber. The three-thin films may break up into filament arrays with core made of materials α surrounded by materials β. Particularly, we need check the cross-section of these filaments to check this hypothesis. The challenge here is to identify two different chalcogenide glasses have compatibility to codrawing together.

8.1.2 3D numerical simulation of azimuth instability

We have explored that the axial stability of continuous filaments and maintained cylindrical shells, and found the axial stability is consistent with capillary instability since the instability has insufficient time to develop during thermal drawing. On the other hand, the physical mechanism of azimuth instability in a thin cylindrical shell is not fully understood at this point. The experimental observations indicate the relevant physical parameters associated with azimuth instability are thickness of film, viscosity, and surface tension, and perhaps stretching stress as well. These parameters imply the azimuth mechanism is possibly related with fluid instability such as capillary instability of thin film during scaling down in cross-section plane while stretching along axial direction. Thus, an initial perturbation at azimuth direction may be amplified due to the fluid incompressibility. A model of fluid mechanics can be applied to simplify the complicated thermal drawing process, and 3D numerical simulation can be performed to check the instability of thin shell.

8.2 Summary

In this thesis, we observed a new physical phenomenon in which a thin cylindrical shell undergoing a scaling process evolves into an ordered array of filaments upon reaching a characteristic thickness during optical-fiber thermal drawing. This structural evolution occurs exclusively in the cross-sectional plane while uniformity is maintained in the axial direction. By a post-drawing annealing procedure, we attained crystalline semiconductor nanofilaments, characterized their electrical and optoelectrical properties, and demonstrated their applications as photo detectors and optical switches. To further understand the maintained structures, we explore the stability (or instability) of these structures from a perspective of capillary instability from fluid mechanics during the complicated thermal drawing process. We perform numerical simulation of capillary instability in a cylindrical shell geometry, and these results provide theoretical guidance in materials selection and in the understanding of attainable feature sizes.

Bibliography

[1] http://www.its.caltech.edu/ feynman/plenty.html

[2] J.T. Hu, T.W. Odom, C.M. Lieber, *Acc. Chem. Res.* **32,** 435 (1999).

[3] Y. N. Xia, P. D. Yang, *et al. Adv. Mater.* **15,**(2003).

[4] Z. L. Wang, *Annu. Rev. Phys. Chem.* **55,** 159(2004).

[5] C. Thelander, P. Agarwal, S. Brongersma, *et al,*, *Materials Today***9**, 28 (2006).

[6] P. J. Pauzauskie and P. D. Yang, *Materials Today* **9,** 36 (2006).

[7] W. Lu and C. M. Lieber, *Nature Materials* **6,** 841 (2007).

[8] F. Patolsky, B. P. Timko, G. F. Zheng, and C. M. Lieber, *MRS Bulletin*, **32**, 142 (2007).

[9] G. Z. Cao, *Nanostructures and Nanomaterials: Synthesis, Properties and Applications, Imperial College Press, London, UK* (2004).

[10] R. S. Wagner, W.C. Ellis, *Appl. Phys. Lett.* **4,** 89, (1964).

[11] M. H. Huang, S. Mao, H. Feick, *et al., Science* **292,** 1897 (2001).

[12] M. S. Gudiksen, J. Wang, and C. M. Lieber, *J. Phys. Chem.* **B105**, 4062 (2001)

[13] Y. Shi, Q. Hu, H. Araki, H. Suzuki, *et al, Appl. Phys. A: Mater. Sci. Process.* **80,** 1733 (2005).

[14] W.I. Park, G. Zheng, X. Jiang, B. Tian and C.M. Lieber, *Nano Lett.* **8,** 3004,(2008).

[15] Y. Y. Wu and P. D. Yang, *J. Am. Chem. Soc.* **123,** 3165 (2001).

[16] X. F. Duan, Y. Huang, Y. Cui, *et al.*, *Nature***409,** 66 (2001).

[17] J. A. Rogers, *Nature photon* **2, 69,** (2008).

[18] G. H. Yu, A. Y. Cao, and C. M. Lieber, *Nature Nanotech.* **2,** 372 (2007).

[19] A. Tao, F. Kim, C. Hess, *et al.*, *Nano Letters* **3,** 1229 (2003).

[20] D. Whang, S. Jin, Y. Wu, *et al., Nano Letters* **3,** 1255 (2003).

[21] P. D. Yang, *Nature***425,** 243 (2003).

[22] Y. Cui, Z. H. Zhong, D. L. Wang, W. U. Wang, C. M. Lieber, *Nano Lett.* **3,** 149 (2003).

[23] Y. Cui, Q. Q. Wei, H. K. Park, C. M. Lieber, *Science* **293,** 1289 (2001).

[24] B. Z. Tian, X. L. Zheng, T. J. Kempa, Y. Fang, N. F. Yu, G. H.Yu, J. L. Huang, C. M. Lieber, *Nature* **449**, 885, (2007).

[25] C. K. Chan, H. L. peng, G. Liu, *et al, Nature Nanotech.*, **3**, 31 (2008).

[26] B. O'Regan and M. Grätzel, *Nature* **353,** 737 (1991).

[27] J. B. Baxter, and E.S. Aydil, *Appl. Phy. Lett.* **86,** 53114 (2005).

[28] M. Law, L. Greene, J. Johnson, R. Saykally, and P. D. Yang, *Nature Mater.* **4**, 455 (2005).

[29] R. D.Maurer, P. C. Schultz, US Patent No. 3,659,915, (Corning Glass Works, 1972).

[30] D. B. Keck, R. D. Maurer, P.C. Schultz, *Appl. Phys. Lett.* **22,** 307 (1973).

[31] G. P. Agrawal, Fiber-optic communication systems, *3rd edn, Wiley-Interscience, New York,* (2002).

[32] A. F. Abouraddy, *et al. Nature Mater.* **6,** 336-347 (2007).

[33] P. Yeh, A.Yariv, and E. Marom, *J. Opt. Soc. Am.* **68,** 1196 (1978).

[34] J. N. Winn, *et al., Opt. Lett.* **23**, 1573 (1998).

[35] Y. Fink, *et al., Science* **282,** 1679 (1998).

[36] B. Temelkuran, *et al., Nature* **420,** 650 (2002).

[37] J. C. Knight, and P. S. Russell, *Science* **296,** 276 (2002)

[38] M. Bayindir, *et al., Nature* **431,** 826 (2004).

[39] S. D. Hart, *et al., Science* **296,** 510 (2002).

[40] O. Shapira, K. Kuriki, *et al., Opt. Express* **14,** 3929 (2006).

[41] T. Sorin, *et al. Adv. Mater.* **19,** 3872 (2007).

[42] D. S. Deng, *et al. Nano Letters* **8,** 4265 (2008).

[43] L. M. Tong, *et al. Nature* **426,** 816-819 (2003).

[44] P. J. A. Sazio, A. Amezcua-Correa, C. E. Finlayson, *et al., Science* **311,** 1583, (2006).

[45] B. R. Jackson, P. J. Sazio, and J. V. Badding, *Adv. Mater*, **20**, 1135 (2008).

[46] H. K. Tyagi, M. A. Schmidt, L. P. Sempere, P. S. J. Russell, *Opt. Express* **16,** 17227, (2008).

[47] X. J. Zhang, Z. Y, Ma, Z. Y. Yuan, M. Su, *Adv. Mater.* **20,** 1310, (2008).

[48] J. Ballato, T. Hawkins, P. Foy, R. Stolen, *et al., Opt. Express* **16,** 18675, (2008).

[49] D. S. Deng, *et al., Appl. Phy. Lett.* **96**, 23102, (2009).

[50] R. A. Zingaro, W. C. Cooper, *Selenium,* Van Nostrand Reinhold, New York, (1974).

[51] B. Gates, B. Mayers, B. Cattle, Y. N. Xia, *Adv. Func. Mater.* **12,** 219, (2002).

[52] N. Ralston, *Nat. Nanotechnol.* **3,** 527, (2008).

[53] J. S. Im, H. J. Kim, M. O. Thompson, *Appl. Phys. Lett.* **63,** 1969 (1993).

[54] F. Boer, *Philips Res. Rep.* **2,** 352, (1947).

[55] E. J. Menke, M. A. Thompson, C. Xiang, L. C. Yang, R. M. Penner, *Nat. Mater.* **5,** 914, (2006).

[56] J. L. Hartke, *Phys. Rev.* **125,** 1177, (1962).

[57] S. R. Elliott, *Mater. Sci. Technol.* **9,** 375, (1991).

[58] H. Kind, H. Q. Yan, B. Messer, M. Law, P. D. Yang, *Adv. Mater.* **14,** 158, (2002).

[59] M. Law, H. Kind, B. Messer, F. Kim, P. D. Yang, *Angew. Chem. Int. Ed.* **41,** 2405, (2002).

[60] M. Wuttig, N. Yamada, *Nat. Mater.* **6,** 824, (2007).

[61] J. Eggers, *Rev. Mod. Phys.* **69,** 865 (1997).

[62] P. de Gennes, F. Brochard-Wyart, D. Quere, *Capillarity and Wetting Phenomena,* Springer (2002).

[63] A. M. Cabazat, and J. B. Fournier, *Bulletin SFP,* **84,** 22 (1992).

[64] J. Plateau, *Acad. Sci. Bruxelles Mem.* **23**, 5 (1849).

[65] L. Rayleigh, *Proc. London. Math. Soc.* **10,** 4 (1878); Rayleigh, *L, Proc. Roy. Soc. London,* **29,** 71 (1879); Rayleigh, L, *Philos. Mag.* **34,** 145 (1892).

[66] S. Tomotika. *Proc. Roy. Soc. London,* **150,** 322 (1935).

[67] H. A. Stone and M. P. Brenner, *J. Fluid. Mech.* **318,** 373 (1996).

[68] X. D. Shi, M.P. Brenner, and S. R. Nagel, *Science* **265,** 219 (1994).

[69] A. M. Ganan-Calvo, R. Gonzalez-Prieto, P. Riesco-Chueca, M. A. Herrada, and M. Flores-Mosquera, *Nature Phys* **3,** 737 (2007).

[70] M. Moseler and U. Landman, *Science* **289,** 1165 (2000).

[71] M. E. Toimil-Molares, A. G. Balogh, T. W. Cornelius, R. Neumann, and C. Trautmann, *Appl. Phys. Lett.* **85,** 5337 (2004).

[72] S. Karim, M. E. Toimil-Molares, A. G. Balogh, W. Ensinger, T. W. Cornelius, E. U. Khan, and R. Neumann, *Nanotechnology* **17,** 5954 (2006).

[73] J. T. Chen, M. F. Zhang, and T. P. Russell, *Nano. Letter.* **7,** 183 (2007).

[74] Y. Qin, S.M. Lee, A. Pan, U. Gosele, and M. Knez, *Nano. Letter.* **8,** 114 (2008).

[75] H. A. Stone, A.D. Stroock, and A. Ajdari, *Annu. Rev. Fluid. Mech.* **36,** 381 (2004).

[76] T. M. Squires and S. R. Quake, *Rev. Mod. Phys.* **77,** 977 (2005).

[77] A. F. Abouraddy, M. Bayindir, G. Benoit, S.D. Hart, K. Kuriki, N. Orf, O. Shapira, F. Sorin, B. Temelkuran, and Y. Fink, *Nature Materials* **6,** 336 (2007).

[78] A. D. Fitt, K. Furusawa, T. M. Monro, and C. P. Please, *J. Lightw. Technol.* **19,** 1924 (2001).

[79] S. C. Xue, M. C. J. Large, G. W. Barton, R. I. Tanner, L. Poladian, and R. Lwin, *J. Lightw. Technol.* **24,** 853 (2006).

[80] P. J. Roberts, F. Couny, H. Sabert, B. J. Mangan, D. P. Williams, L. Farr, M. W. Mason A. Tomlinson, T. A. Birks, J. C. Knight, and P. St.J. Russell, *Opt. Express* **13,** 236 (2005).

[81] I. M. Griffiths and P. D. Howell, *J. Fluid Mech.* **593,** 181 (2007); **605,** 181 (2008).

[82] B. Temelkuran, S. D. Hart, G. Benoit, J. D. Joannopoulos, and Y. Fink, *Nature* **420,** 650 (2002).

[83] G. K. Batchelor, *An Introduction to Fluid Dynamics,* Cambridge University Press (2000).

[84] S. D. Hart, Y. Fink, *Mat. Res. Soc. Symp. Proc.* **797,** W.7.5.1 (2004).

[85] S. D. Hart, *Multilayer composite photonic bandgap fibers,* PhD thesis, MIT (2004).

[86] R. Scardovelli and S. Zaleski, *Annu. Rev. Fluid Mech.* **31,** 567 (1999).

[87] S. Osher and J. A. Sethian, *J. Comput. Phys.* **79,**12 (1988).

[88] S. Osher and R. P. Fedkiw, *J. Comput. Phys.* **169,**463 (2001).

[89] J. A. Sethian and P. Smereka, *Annu. Rev. Fluid Mech.* **35,** 341 (2003).

[90] E. Olsson and G. A. Kreiss, *J. Comput. Phys.* **210,** 225 (2005).

[91] V. F. Dobrescu and C. Radovici, *Polym. Bull.* **10,** 134 (1983).

[92] S. Egusa,*et al.*, unpublished.

[93] M. F. Culpin, *Proc. Phys. Soc.* **B70,**1069 (1957).

[94] A.S. Tverjanovich, *Glass Phys. Chem.* **29,** 532 (2003).